Microstructure and Surface Characterization of Incrementally Formed AA 7075

by

Maya Nath

A dissertation submitted in partial fulfillment
of the requirements for the degree of
Doctor of Philosophy
(Materials Science and Engineering)
in the University of Michigan
2019

Doctoral Committee:

Professor Alan I. Taub, Chair
Professor John E. Allison
Professor Amit Misra
Professor Jun Ni

Maya Nath

nathm@umich.edu

ORCID iD: 0000-0002-0707-2301

Dedication

To Tata, who

Gave me strength,

Inspired me to dream, and

Taught me to never stop learning

Acknowledgements

I would first like to thank my advisor and committee chair, Professor Alan Taub, for giving me this opportunity and mentoring me every step of the way during my graduate studies. I am grateful for his unwavering support, guidance and sixth sense for knowing when I'm about to panic. I would also like to thank the rest of my committee members – Professor John Allison, Professor Amit Misra and Professor Jun Ni, for their support, direction and valuable critique of my dissertation work. Special thanks to Professor Allison for access to the SEM and sample preparation equipment that made the characterization work possible. Additionally, thank you to Professor Samantha Daly for a warm welcome to the University of Michigan.

I would also like to acknowledge the members of the University of Michigan Incremental Sheet Forming team. I am grateful for Professor Mihaela Banu's encouragement and helpful insights. Jaekwang Shin, Ankush Bansal, Randy Cheng and Erika Salem are some of the best people I've worked with and I am grateful for their advice, numerous helpful discussions and willingness to brave the band saw. Thank you also to Xianli Qiao, Pritam Das, Timothy Odykirk, Adrian Sanchez-Lohff, Elizabeth Gager and Benjamin Serratos for their assistance.

In addition, I wish to thank our collaborators: Brian Martinek from Boeing provided the material used in this research; Professor Jian Cao, Newell Moser, Dohyun Leem and Dr. Zixuan Zhang from Northwestern University provided helpful discussions and DSIF parts to be characterized; Professor Farhang Pourboghrat and Dr. Hyunki Kim from the Ohio State University and Professor Veera Sundararaghavan, Dr. Ali Ramazani and Aaditya Lakshmanan

from the University of Michigan provided helpful discussions and collaborations on texture prediction using ICME tools.

I'd also like to thank Professor Kathleen Sevener for access to the autopolisher to prepare my EBSD samples, John Lasecki for help with the electropolisher and Keith McIntyre for always being willing to brainstorm ideas and help troubleshoot in the lab. Thank you to Bobby Kerns and the Michigan Center for Materials Characterization for assistance with FIB analysis and insights on metallographic sample preparation for EBSD analysis. And an additional thanks to Ellen Kampf, who tirelessly works to make sure everything in the Taub group happens on time.

I wish to also thank my colleagues for their friendship, encouragement and just the right amount of comedic relief to make this time more enjoyable: Dr. Tracy Berman, Dr. Riddhiman Bhattacharya, Dr. Wesley Chapkin, Dr. Erin Deda, Dr. Iman Ghamarian, Dr. Joyce Gong, Dr. Michael Kimiecik, Dr. Will LePage, Dr. Aeriel Murphy-Leonard, Dr. Vir Nirankari, Dr. Qianying Shi, Avi Bregman, Aaron Gladstein, Yipeng He, Ashley Hilmas, Amy Langhorst, Anita Luong, Tasha Mangaldas, Caleb Reese, Elaina Reese, Anshul Singhal, and Daney Zhang.

This work would not have been possible without the love and support of my family and friends. Thank you to Dr. Shridhar, Shrilata and Kartik Nath for being my rocks and always picking up the phone when I call. Thank you also to Anjali and Umesh Singh, Kaajal Singh, Asha, Ela and Dr. Parag Aggarwal, Vijay and Natasha Singh and Professor Mahesh Aggarwal.

Finally, I would like to acknowledge the funding of this work by the DOD-ONR through the American Lightweight Materials Manufacturing Institute – LIFT. I would also like to thank the Horace H. Rackham Graduate School for the Rackham Merit Fellowship and financial awards that supported my travel to various conferences throughout my PhD to present my work.

Table of Contents

List of Tables

List of Figures

List of Equations

List of Acronyms and Symbols

AA = Aluminum Alloy

CP-FEM = Crystal Plasticity Finite Element Model

DSIF = Double Sided Incremental Forming

EBSD = Electron Backscatter Diffraction

EDS = Energy Dispersive Spectroscopy

FEM = Finite Element Model

FFL = Fracture Forming Line

FIB = Focused Ion Beam

FLC = Forming Limit Curve

ISF = Incremental Sheet Forming

ND = Normal Direction

RD = Rolling Direction

SEM = Scanning Electron Microscope

SPIF = Single Point Incremental Sheet Forming

TD = Transverse Direction

TPIF = Two Point Incremental Forming

α = Forming Angle

eSF = Effective Squeeze Factor

pSF = Programmed Squeeze Factor

t_0 = Initial Sheet Thickness

t_f = Formed Sheet Thickness

Δz = Step Size

List of Appendices

Abstract

Lightweighting in the automotive and aerospace industries is critical for improving fuel economy without sacrificing safety and performance. Replacing heavier steel components with lightweight materials, such as aluminum alloys, reduces the overall vehicle's weight; a 10% weight reduction can result in a 6-8% improvement in fuel economy. However, the decision to commercialize new lightweight metal components is dependent on the economics of production volume and manufacturing costs. Conventional forming processes such as stamping and deep drawing are economical for high volume production, while additive manufacturing processes are economical for low volume production.

Incremental Sheet Forming (ISF) is a die-less or low-cost die manufacturing process where components are formed from metal sheet through a series of localized plastic deformations. ISF uses much lower forming forces than conventional processes; it also allows for the forming of detailed, customizable parts and requires shorter forming times than additive processes. These advantages allow for it to be competitive for mass customization and low volume production. It is of high interest for prototyping, after-market service and creating complex products with high strength at low costs.

For ISF to be widely used, current challenges predicting the microstructure and mechanical properties of the as-formed parts must be addressed, as well as concerns about tribological and mechanically induced surface features that may impact fatigue life. An improved sample preparation technique for Electron Backscatter Diffraction (EBSD) analysis was

developed, which allowed a majority of the grain structure to be resolved at the highly deformed areas. Grains elongated proportionally to the stretch of the sheet and no evidence of recrystallization was found in the formed parts. This suggested that the starting grain structure can be used to predict the microstructure evolution due to a known strain path and Integrated Computational Materials Engineering (ICME) tools can be used to predict texture.

Additionally, inconsistencies in the amount of contact between the forming tool and sheet induced variations in surface finish on the as-formed components, even within a single tool striation. The majority of the deformation occurred under the tool with limited deflection at the microscale and material that was pushed forward by the forming tool formed a macroscopic bulge after the final tool pass, which is a defect part manufacturers want to avoid. These surface metrology studies enabled characterizing the surface features that developed on the formed parts, which may have an impact on the fatigue properties. Tribological grooves formed on the tool side surface and the native oxide layer cracked on the non-tool side surface. The density of the grooves was affected by process variant, wall angle and squeeze factor and their orientation depended on the rolling direction of the initial sheet material. While cracking in the oxide layer is unlikely to be sites of fatigue crack initiation, cracks in the second phase particles (Al-Mg-Zn) may serve as areas of high stress concentration, leading to potential fatigue crack growth.

Chapter 1. Introduction

1.1 Motivation

Lightweighting in the automotive and aerospace industries is critical for improving fuel economy without sacrificing safety and performance. Replacing heavier steel components with lightweight materials, such as aluminum alloys, reduces the overall vehicle's weight. Since it takes less energy to accelerate a lighter object than a heavier one, a 10% weight reduction can result in a 6-8% improvement in fuel economy [1]. According to the U.S. Department of Energy, "using lightweight components and high-efficiency [internal combustion] engines enabled by advanced materials in one quarter of the U.S. fleet could save more than 5 billion gallons of fuel annually by 2030" [2].

However, the decision to commercialize new lightweight metal components is dependent on the economics of production volume and manufacturing costs. Conventional forming processes such as stamping and deep drawing offer high volume production capability but require sizeable forming forces and high capital costs due to large, expensive matched die sets that necessitate long manufacturing lead times. In addition, the dies need to be stored for long periods of time after production has ended to be available for making spare parts. These processes are economical for high volume production as the die costs can be amortized. In contrast, additive manufacturing processes are economical for low volume production. Although they offer component customizability and the ability to create detailed parts, additive processes require much longer forming times. Additionally, the mechanical properties of additively formed parts are less desirable than those of conventionally formed parts [3-6].

Incremental Sheet Forming (ISF) is a die-less or low-cost die manufacturing process where components are formed from metal sheet through a series of localized plastic deformations. ISF uses much lower forming forces than conventional processes, offering significant cost savings for small volume production, since dies are not necessary for the manufacturing process (Figure 1.1a). Even if a die is needed, it can be rapidly produced from inexpensive materials, such as plastics. ISF also allows for the forming of detailed, customizable parts and requires shorter forming times than additive processes (Figure 1.1b). These advantages allow for ISF to be competitive for mass customization and low volume production, up to thousands of parts per year. It is of high interest for prototyping, after-market service, creating complex products with high strength at low costs, minimizing manufacturing lead-time and meeting application-specific material properties in the automotive and aerospace industries [3-7].

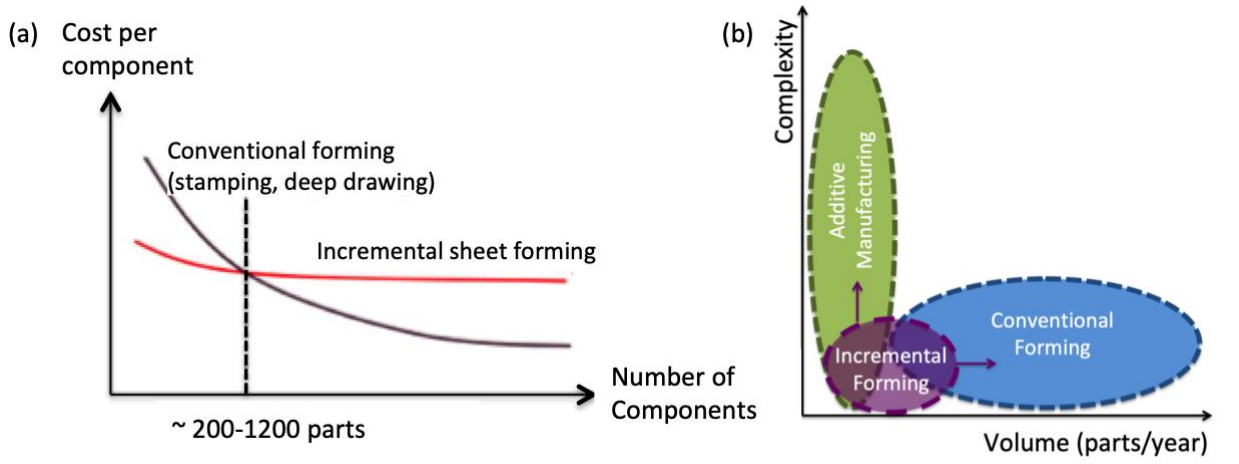

Figure 1.1 (a) Cost comparison between conventional forming processes and ISF [6]. ISF is cost-advantageous until ~200-1200 components produced. After that, conventional processes become cost-advantageous due to amortized die costs. (b) Part complexity versus production volume comparison for conventional forming, additive manufacturing and ISF. ISF is being studied to fill the niche in industry of 'low volume production-mass customization.'

For ISF to be commercialized, several concerns still need to be addressed. Like other forming processes, ISF generates residual stresses that affect the final part geometry. However, while conventional forming processes use a full die, ISF can have little to no mechanical support

for the sheet during forming, leading to deformations that induce large, non-uniform residual stresses [8-11]. This leads to springback in parts that is not yet predictable by modeling and affects the physical metallurgy and microstructure of the material [12-17]. In addition to modeling springback, challenges exist predicting and modeling the mechanical properties in the formed components, such as tensile, compressive and fatigue behavior [17]. Tribology and mechanical deformation affect the surface of the formed component, which influence mechanical properties and may initiate failure [18-20]. Microstructure determines mechanical properties, and with the addition of surface finish, influences the performance of the as-formed parts. Addressing this is fundamental for ISF components to be widely used in industry.

1.2 Thesis Overview

Developing Incremental Sheet Forming (ISF) as a robust manufacturing process is a flagship project in Novel/Agile Processing for Lightweight Innovations for Tomorrow (LIFT), an institute in the Manufacturing USA network. This particular project was focused on incrementally forming aluminum alloy (AA) 7075 for applications in the aerospace industry. Efforts were made to optimize geometric accuracy, processing parameters, part performance and finite element and cost modeling [21-24]. The overall objective of the LIFT project was to optimize the ISF process for it to be used to economically fabricate parts that can be flight certified. This research focused on the area of materials characterization: validating that the microstructure of the incrementally formed parts was consistent with that of conventionally formed parts; determining if the microstructure evolution could be predicted with Integrated Computational Materials Engineering (ICME) tools; and identifying any potential surface defects that could limit the fatigue life of the formed parts.

This dissertation work has two key research objectives for optimizing the performance of incrementally formed AA 7075:

1. Characterizing the microstructural evolution under various strain paths and locally applied force to determine if the microstructure of the formed part can be predicted
2. Studying the surface of as-formed components to understand its potential impact on fatigue properties

Chapter 2 introduces the ISF process and includes the relevant literature on the microstructure and surface finish of conventionally formed and incrementally formed aluminum alloys. Conventional forming processes, which are considered to be benchmark processes for ISF, include stamping, deep drawing, hydroforming and rolling. The microstructural evolution during ISF is detailed in Chapter 3 and an improved sample preparation technique for resolving the microstructure at the highest strains with Electron Backscatter Diffraction (EBSD) is described. Chapter 4 focuses on studies in surface metrology of incrementally formed parts: quantifying the amount of interaction between the tool and the sheet and understanding how material is moved during forming. Chapter 5 concentrates on the surface features that develop during ISF: classifying features on the forming and supporting sides and characterizing as-formed parts to determine the effects of various process parameters including process variant, wall angle and squeeze factor. Conclusions and future work are outlined in Chapter 6.

Chapter 2. Literature Review

2.1 Incremental Sheet Forming

In the Incremental Sheet Forming (ISF) process, a metal sheet is clamped between blankholders and locally deformed using a rigid forming tool that moves along a predefined path until the final three-dimensional geometry is formed (Figure 2.1). The as-formed part is then removed from the clamping system and ready for post-forming heat treatments and/or finishing operations. Several parameters can be controlled during forming, including sheet material and initial thickness (t_0), tool diameter, tool path, step size, forming angle (α), feed rate, spindle speed, tool path and lubrication [3-6,18].

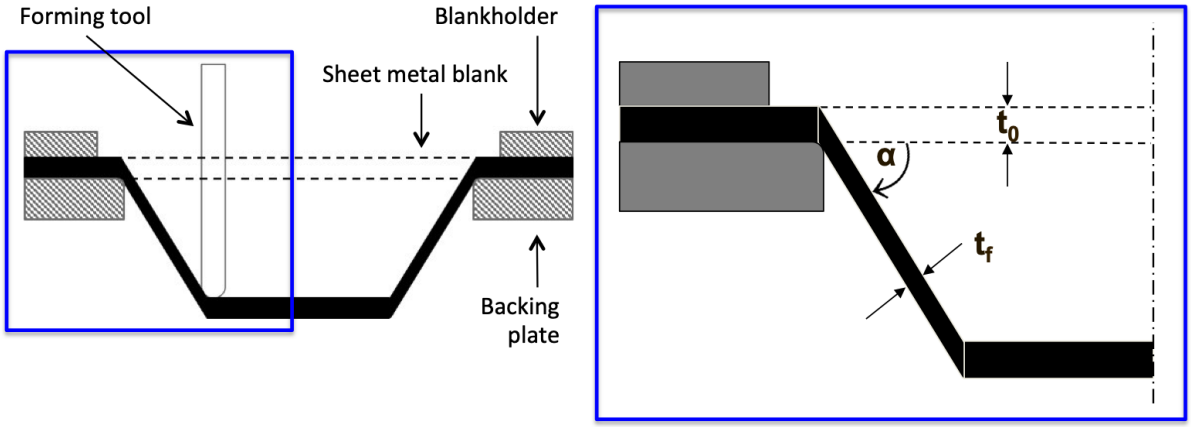

Figure 2.1 Schematic of the ISF process. The sheet metal blank is clamped between blankholders and deformed with the forming tool. t_0 is the initial sheet thickness, t_f is the formed sheet thickness and α is the forming angle.

Three variants of this process exist, defined by the number of contact points between the sheet, forming tool and potential die: single point incremental forming (SPIF); two point incremental forming (TPIF); and double sided incremental forming (DSIF) (Figure 2.2). In

SPIF, there is one point of contact between the sheet and forming tool. In TPIF, there are two points of contact; the first is between the sheet and the forming tool on the front side, and the second is between the sheet and either a full or partial die on the backside. In DSIF, there are also two points of contact; the sheet is deformed on either side by forming tools in a master-slave relationship [3]. The ISF research team at the University of Michigan is able to experimentally perform SPIF and TPIF on a CNC lathe, CNC milling machine and CNC industrial robots.

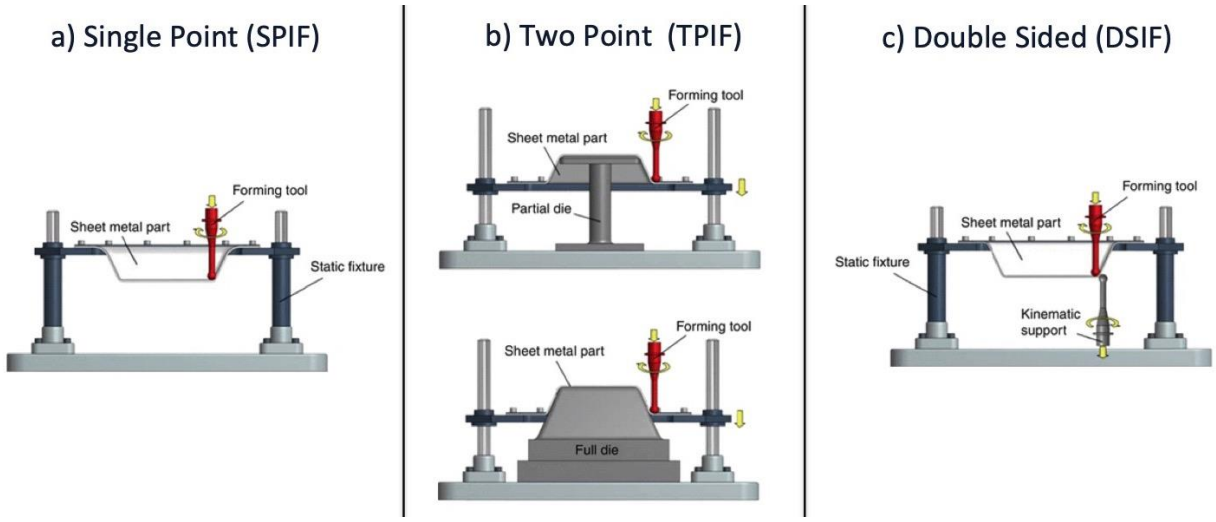

Figure 2.2 Variants of ISF: (a) Single Point Incremental Forming (SPIF); (b) Two Point Incremental Forming (TPIF); (c) Double Sided Incremental Forming (DSIF) [6]

The underlying mechanics of the ISF process allow for greater formability, making it advantageous compared to conventional forming processes such as stamping or deep drawing. Components made by conventional forming processes fail at the onset of necking, given by the forming limit curve (FLC) on Figure 2.3e [25]. However, the complexity of the stress states created during the ISF process allow for necking to be suppressed until higher strains are reached, pushing the point of failure to the fracture forming line (FFL) on Figure 2.3e. This is

due to the presence of bending, stretching and through-thickness shearing; the latter two deformation processes work to stabilize the material (Figure 2.3a-d) [26-30].

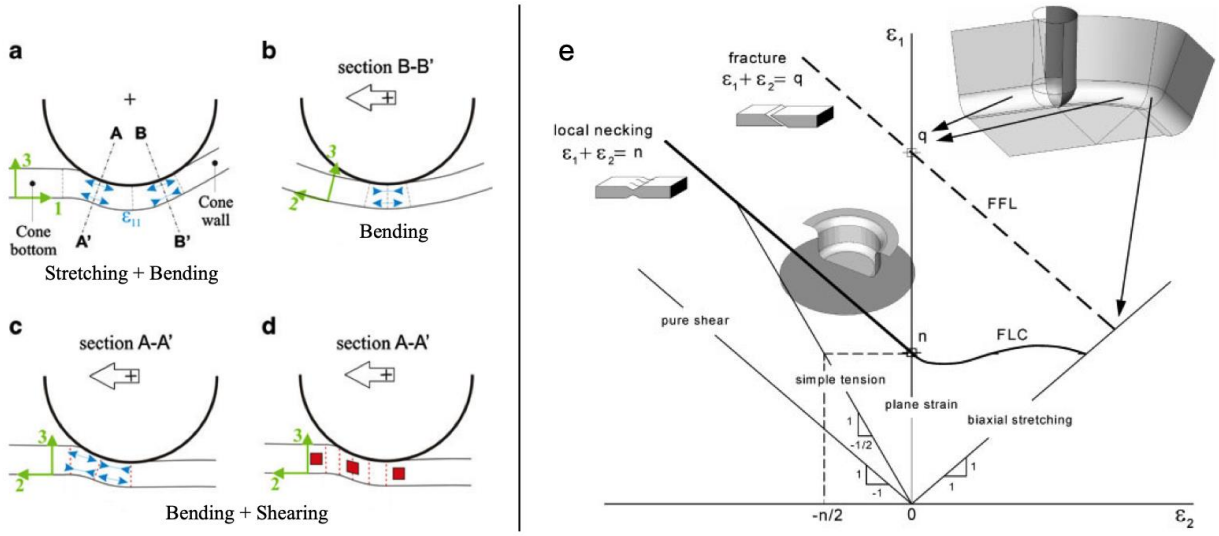

Figure 2.3 (a-d) Stretching, bending and through-thickness shearing deformation mechanisms in ISF [26] and (e) formability limits of ISF compared to conventional forming. FLC is the forming limit curve; FFL is the fracture forming line. [25]

ISF parts are thinner than conventionally formed parts. In conventional forming processes, material under the clamps can be drawn in, allowing for higher angle parts up to a full 90° to be formed. In ISF, material under the clamps is not allowed to flow, providing a limitation on the maximum angle at which a part can be formed, which is given by the sine law (Equation 2-1). t_0 is the initial thickness, t_f is the thickness after forming, and α is the wall angle (Figure 2.1).

$$t_f = t_0 \sin(90° - \alpha) \qquad (2\text{-}1)\ [31]$$

For the sine law to hold true, it assumes that the deformation is a straight projection onto the surface of the final part, the through-thickness deformation is pure shear and volume is constant and conserved [4, 31]. It is found to be most accurate at the midpoints of the as-formed part walls. Accuracy decreases as the sheet material bends into the defined wall thickness and at

large wall angles that have a region of thinning [31-33]. These two regions will be seen clearly on the thickness profiles of SPIF cones in Chapter 3. The profiles also show non-uniform behavior even for a constant wall angle, which can be attributed to overlapping of the tool passes during forming (Figure 2.4a) [34]. As the tool successively moves down each step (Δz), certain areas are repeatedly deformed. This leads to local strain hardening, increasing the equivalent strain of the formed material and affecting the fracture behavior. The contact area is given as a function of wall angle, tool radius and step size (Equation 2-2, Figure 2.4b) [35]. The amount of overlap increases with increasing contact area.

$$A = \frac{\pi R}{2}(R + \Delta z) + \frac{\pi R^2}{2(\delta - \alpha)}(\sin\alpha - \sin\delta) \qquad (2\text{-}2)\ [35]$$

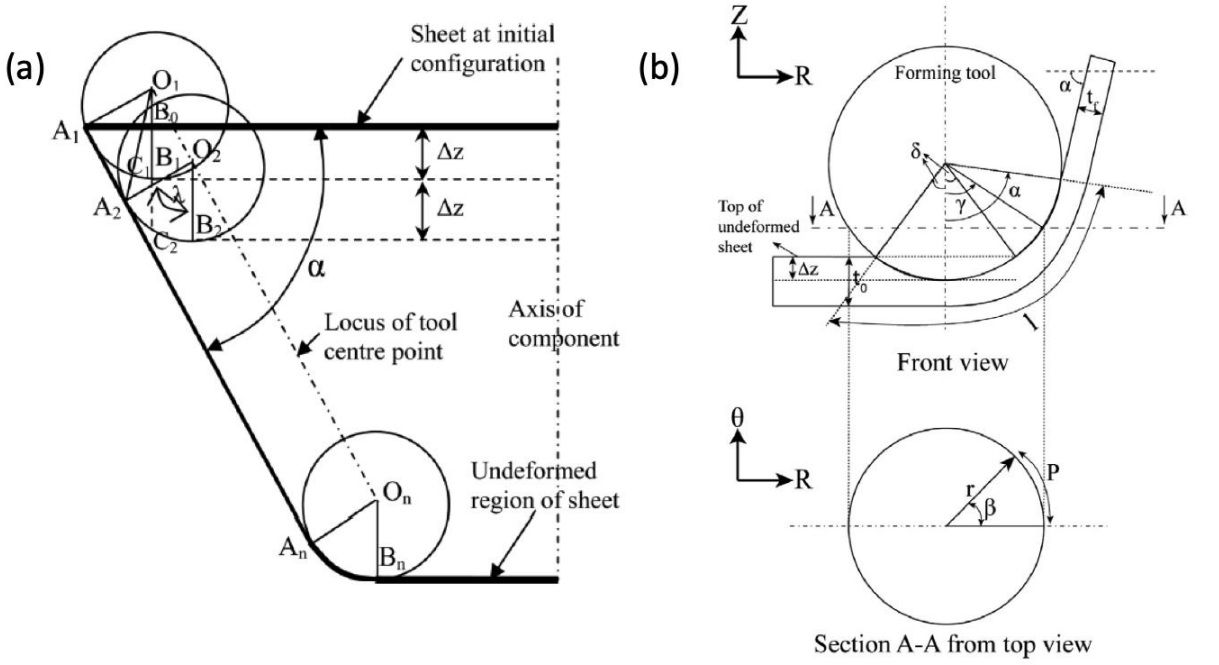

Figure 2.4 (a) Material and tool movement during ISF of a truncated cone [34] and (b) defining the contact area between the forming tool and sheet. [35] Δz = step size, α = forming angle, t_0 = initial sheet thickness, t_f = formed sheet thickness, R = forming tool radius.

In TPIF and DSIF, an additional parameter of squeeze factor exists, quantifying the amount of material squeezed between the forming tool and die surface (TPIF) or between the

two tools (DSIF). For TPIF, it is defined as the ratio of the distance between the tool contact point and die surface (d) to the local formed sheet thickness (t_f). Work in progress to be published by the University of Michigan ISF team indicates that the effective value of squeeze factor is different than what is programmed into the CNC machine due to the elastic deflection of the tool away from the die surface and intrinsic machine compliance [36,37]. Two values for squeeze factor were defined: programmed squeeze factor (pSF) and effective squeeze factor (eSF), where Δ accounts for the deflection and compliance (Equations 2-3, 2-4, 2-5).

$$pSF = \left(1 - \frac{d}{t_0 * \sin(90-\alpha)}\right) \times 100 \quad \text{(2-3) [37]}$$

$$eSF = \left(1 - \frac{d+\Delta}{t_0 * \sin(90-\alpha)}\right) \times 100 \quad \text{(2-4) [37]}$$

$$\text{where, } t_f = t_0 * \sin(90-\alpha) \quad \text{(2-5) [37]}$$

2.2 Aluminum Alloy 7075

The 7XXX series of aluminum alloys include the highest strength aluminum alloys and are commonly used in aerospace, structural and other high performance applications. These alloys are heat treatable, generally strengthened via precipitation hardening and can be further strengthened with cold working [38]. This dissertation work focuses on ISF of aluminum alloy AA 7075 (composition: Al – 1.4Cu – 2.4Mg – 0.19Cr – 5.7Zn) in the O temper.

The mechanical properties of AA 7075 are heavily dependent on the tempering, therefore forming was done on O temper, or annealed, sheet. The annealing heat treatment reduces the residual stress effects of plastic deformation from the rolling process, increasing ductility of the material for forming. However, since the O temper is the lowest strength temper, the final components will be heat treated into the T6 condition before use to meet application-specific performance requirements. Table 2.1 compares the mechanical properties of AA 7075-

O and AA 7075-T6 from literature as well as the sheet material used for these experiments [39]. It can be seen that the O temper material has lower yield, tensile and shear strengths and increased elongation compared to the T6 material. Thus, even though the sine law defines the maximum wall angle able to be fabricated, components formed in the O temper are more likely to reach higher wall angles than those formed in T6.

Table 2.1 Mechanical Properties for AA 7075-O and AA 7075-T6

Mechanical Property	O Temper [39]	T6 Temper [39]	O Temper (Experimental)	T6 Temper (Experimental)
Ultimate tensile strength	230 MPa	570 MPa	230-260 MPa	576-581 MPa
Yield strength	105 MPa	505 MPa	100-110 MPa	503-510 MPa
Elongation	17%	11%	13.1 – 14.2%	7.5-8.0 %
Hardness	60 HB	150 HB (~180 Vickers)	67.8-68.4 Vickers	174.8-179.9 Vickers
Shear strength	150 MPa	330 MPa	-	-

Zn is the primary alloying in AA 7075 and acts as a grain refiner; the η phase ($MgZn_2$) commonly forms along the grain boundaries [39]. Several other possible strengthening precipitates include the T-phase ($Al_2Mg_3Zn_3$), S-phase (Al_2CuMg), θ-phase (Al_2Cu) and Mg_2Si [40]. Additional dispersoids that are 0.01-0.5μm in size and larger constituent particles up to 50μm in size can also be found. These particles tend to be hard, brittle and can crack during bulk processing and machining. If they break at the surface, they can serve as potential crack nucleation sites, especially for fatigue crack growth [40-42].

Similar to other aluminum alloys, AA 7075 rapidly forms a thin aluminum oxide film on the surface. This film clings tightly to the metal sheet and blocks further oxidation of the material [39]. Studies have been done to characterize the behavior of the surface with the native oxide layer during processing. One study on micro-crack formation during cold rolling

theorized that the oxide films are fractured during rolling and as the cracks open, aluminum is extruded through. This leaves a final sheet surface of oxide fragments and metal surfaces [43]. This behavior is similar to what will be shown in the surface characterization work on incrementally formed parts in Chapter 5.

2.3 Microstructure and Surface Finish of Conventional Forming Processes

Conventional forming processes can be classified into two categories depending on the forming temperature. In cold working, all processing occurs at temperatures below the recrystallization temperature of the material. Hot working is defined when all processing occurs above the recrystallization temperature [44]. These lead to different resultant microstructures and surfaces. Conventional forming processes of interest as benchmark for this work include:

- Stamping: Components are formed from metal sheet by pressing the sheet between a set of matched dies into the desired geometry [45]
- Deep Drawing: Cylindrical or box-shaped components are formed from metal sheet by pressing the sheet metal blank into a die cavity [45]
- Rolling: Plate and sheet are formed by sending a metal piece through a set of rolls that reduce the thickness or change the cross-section by applying compressive forces [45]
- Hydroforming: Components are formed when metal sheet is pressed into a die using a high pressure hydraulic fluid [45]

2.3.1 Stamping

While stamping at ambient temperature has been a commonly used industrial process for many years, hot stamping is becoming increasingly popular. This is because aluminum alloys are known to have greater formability at higher temperatures than at room temperature, increasing the application space. In certain types of hot stamping, forming and quenching can occur together; metal sheet is solutionized, formed immediately and then quenched while the

formed component is still in the die. This decreases the amount of springback because the part is constrained in the die. It also allows for the microstructure of the formed part to be set in the supersaturated solid solution state, which increases strength when combined with a post-forming aging treatment [46,47]. Fan et al. studied the formability and strengthening mechanism of an Al-Mg-Si alloy [48]. Parts were stamped at temperatures ranging from room temperature to 500°C. It was found that the grain structure of the as-received rolled sheet could not be resolved via electron backscatter diffraction (EBSD) because there was too much distortion in the crystal structure from rolling. However, the grain structure was able to be resolved after stamping (Figure 2.5). For sheet stamped at room temperature, the grains formed an equiaxed structure that seemed to undergo recovery but not recrystallization. As the temperature increased, the grain structure did not significantly change. Some recrystallized grains appeared around the originally larger grains, and the number of high angle grain boundaries decreased, indicating the sample became textured.

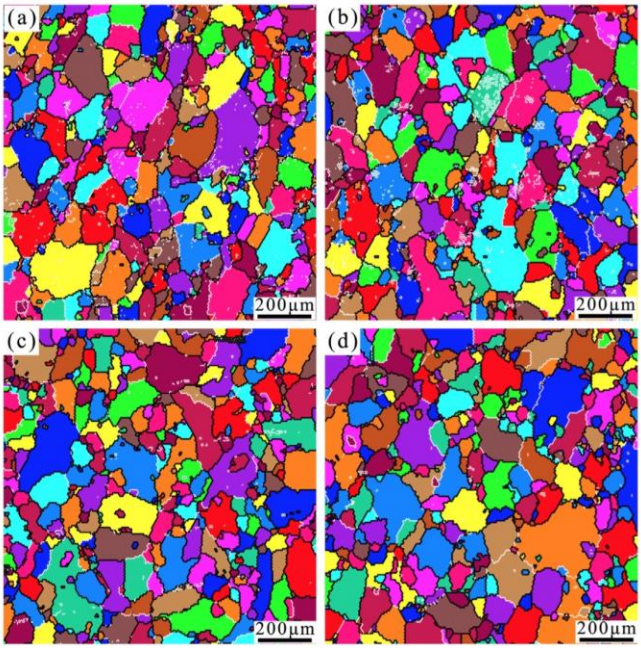

Figure 2.5 Microstructure of an Al-Mg-Si alloy stamped at (a) 25°C (b) 200°C (c) 400°C and (d) 500°C [48]

In addition to microstructure, several studies have been done characterizing frictional behavior and the surfaces of stamped components. Azushima et al. studied the friction behavior of hot-stamped aluminum coated high strength steel with and without added lubrication [49]. The lubricated conditions consistently had smaller coefficients of friction than the dry conditions, and the coefficient of friction was found to be dependent on the roughness of the die surface for lubricated stamping, but independent for dry stamping. Ghiotti et al. studied the tribological performance of several solid lubricants used for warm stamping of AA 6016 [50]. The activated lubrication mechanism was found to be highly dependent on the thickness of the applied layer. Additionally, the coefficient of friction was dependent on the pressure at the die/specimen interface while not significantly affected by the sliding speed. Boron-nitride was not a reliable lubricant, while graphite and molybdenum disulphide (MoS_2) were more promising. Incidentally, MoS_2 was found to be optimal for ISF of AA 7075-O and is used in grease form for all the experiments in this dissertation work.

2.3.2 Deep Drawing and Rolling

Another conventional forming process, commonly used for the production of beverage cans, is deep drawing. During the drawing process, the development of planar anisotropy induces earring, a forming defect that looks like uneven rims on the drawn product. Earrings lead to an inhomogeneous distribution of mechanical properties, wall thickness and microstructure [51]. Wang et al. studied the effects of blankholders on the drawability of AA 5182-O sheet [52]. It was found that a flat blankholder created a more severe earring than a curved blankholder but did not affect the microstructure. The microstructures of the formed cups were examined (Figure 2.6) at three locations on the cup. The bottom of the cups had the least amount of strain and the grain structure reflected that of the original rolled sheet (Figure

2.6a,d). In contrast, the shoulders of the cups had the maximum amount of deformation due to the bending, stretching and sliding mechanisms. This was reflected in the grain structure (Figure 2.6b,e); the grains were elongated in the bending orientation. Finally, the third region was at the top of the sidewall, near the blankholders (Figure 2.6c,f). The grains were slightly more elongated than the original material, but not to the extent of the shoulder region.

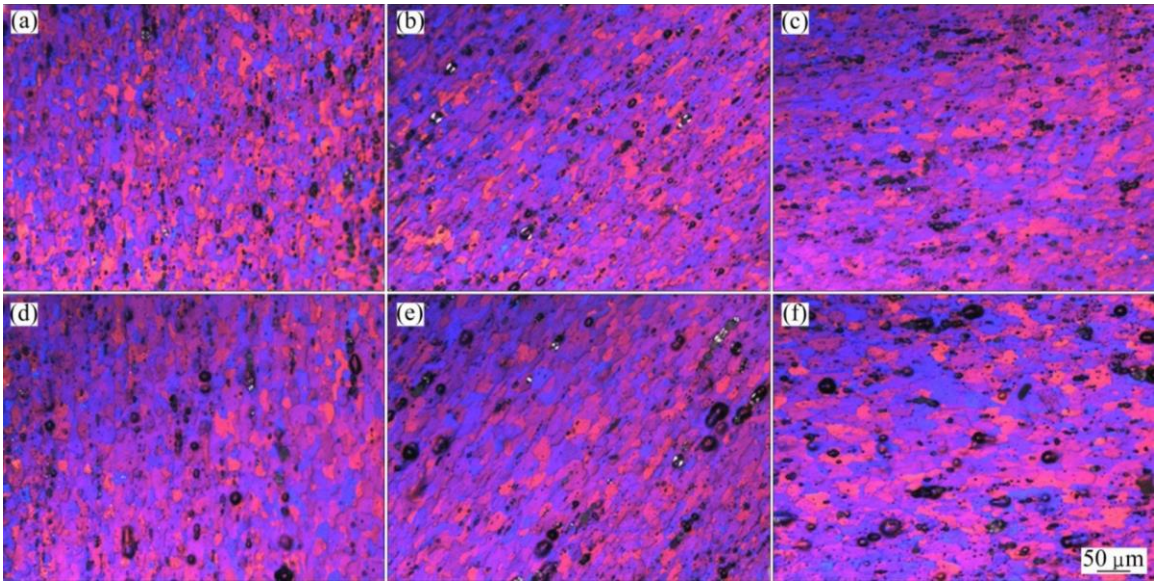

Figure 2.6 Microstructure of AA 5182-O drawn cup specimens at the bottom (a,d), shoulder (b,e) and sidewall (c,f) using a flat blank holder (a-c) and a curved blank holder (d-f) [52]

Deep drawing and plane strain rolling are related through a 90° rotation and their textures are also geometrically related (Figure 2.7) [53]. This relationship was used in work by Savoie et al. to study texture development in AA 1XXX and AA 5XXX alloys during uniaxial tension and deep drawing [53]. Texture analysis on tensile samples along the rolling and transverse direction showed the development of <111> and <100> type fiber textures. Fiber textures exhibit rotational symmetry and are represented by specifying the crystallographic direction with respect to the axis of deformation. This is in contrast to peak-type textures, which have one or more components centered on an ideal orientation and are denoted by specifying the crystallographic plane and direction [54]. At the beginning of the deep drawing process, the

samples exhibited textures similar to the uniaxial tensile samples. Deformation up to ~25% radial strain followed plane strain behavior, and once the coordinate system was rotated, the deep drawn textures matched those of plane strain rolling. The texture components changed from fiber to peak type, with the presence of Goss {011}<100>, Cu {112}<111>, P {011}<111>, Y {111}<112> and cube {001}<110> texture components. As the edge of the blank was approached, the strain path differed from the plane strain conditions, and the texture changed again [53].

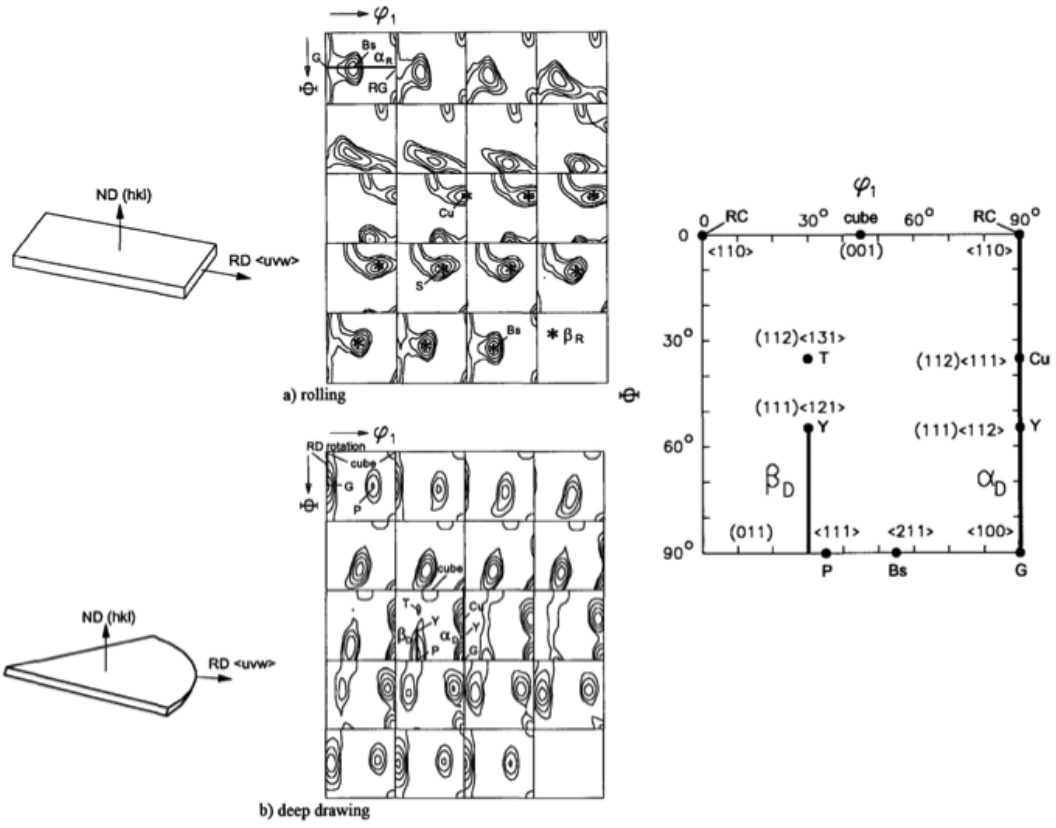

Figure 2.7 Textures that develop in AA 1145 during rolling and deep drawing (left) with a key to read the ODFs (right). The coordinate system has not been rotated, so textures do not visually match. [53]

Martins et al. studied deep drawn AA 3104 from metal sheet that went through different rolling conditions [55]. The texture of the formed components was balanced; the recrystallization cube texture {001}<100> appeared similar in intensity to the deformation brass

{110}<112> and copper {112}<111> textures. Roughness in the transverse direction was consistently higher than in the rolling direction. Additionally, the cup that was drawn from the sheet cold rolled in a single stage mill had the highest surface roughness, likely due to the wear of the work roll.

Similar to what is seen in the shoulder regions of deep drawn cups, the grain structure of rolled material is elongated [56-59]. Tajally et al. studied the mechanical and anisotropic behavior of AA 7075 rolled sheet [60]. The microstructure of the starting material and that cold rolled to 71% was compared (Figure 2.8). It was found that while both materials had elongated grains, the starting material had an aspect ratio (grain length/grain width) of 5, and the 71% cold rolled material had an aspect ratio of 35, increased by a factor of 7.

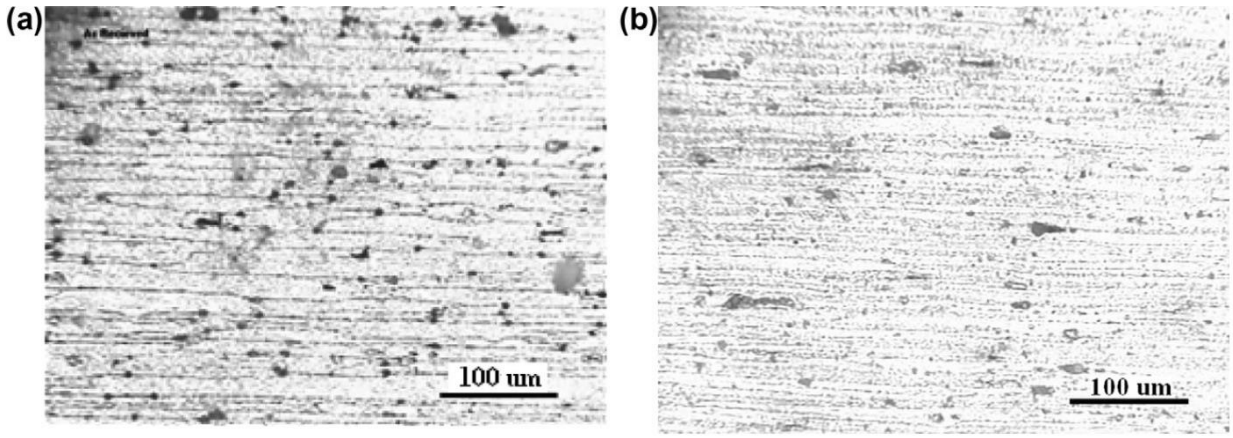

Figure 2.8 Microstructure of the (a) starting material and (b) 71% cold rolled material, AA 7075 [60]

Zhang et al. studied microcrack formation in cold rolled AA 5052 [43]. Microcracks were observed near the entry at the roll bite, perpendicular to the rolling direction. The study found that the cracks opened up at the roll bite and aluminum was extruded through the cracks during rolling, forming a surface comprised of oxide and metal fragments. Cracking was also seen in the rolling studies done by Mo et al. on aluminum brass [61]. For samples with an

equiaxed grain structure, cracking was observed at ~80% thickness reduction, while samples with columnar grain structures were able to achieve a good surface finish at ~ 95% reductions.

2.3.3 Hydroforming

In contrast to the microstructures formed by rolling and deep drawing, the microstructure formed by hydroforming is closer to that of stamping. Chu et al. studied the deformation characteristics of a hydroformed Y-shaped tube made of AA 6061 [62]. After forming, macroscopic defects including bursts and wrinkles were examined in addition to microstructures at various regions on the formed part (Figure 2.9). Point A was located on the protrusion, which experienced larger elongation and had a corresponding grain structure. The other points had versions of an equiaxed grain structure. Points B and D had similar shapes and sizes while point C had the most refined grain structure. Point C was located at a zone that experienced both compression and elongation.

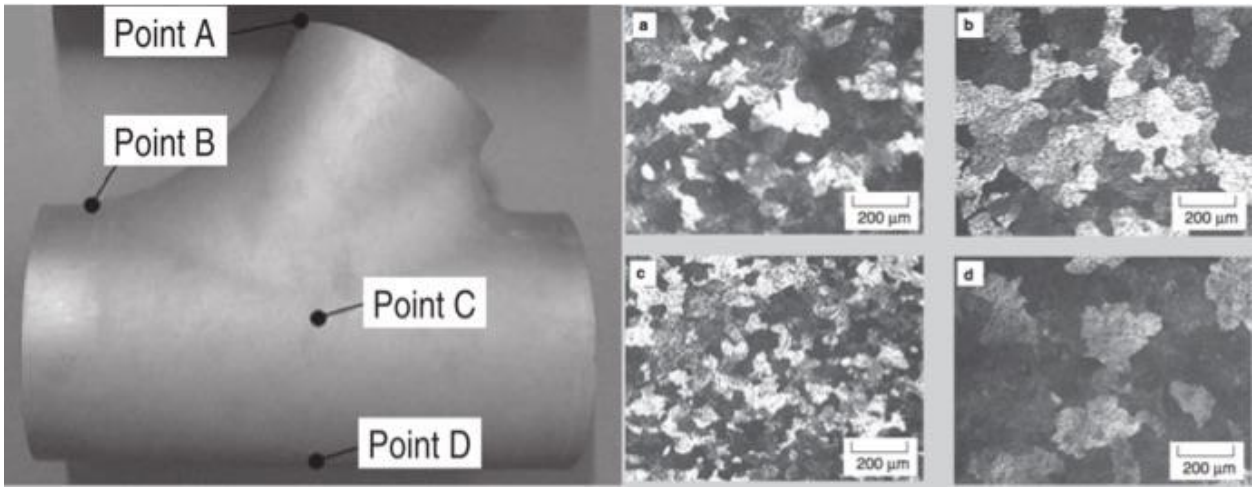

Figure 2.9 Y-shaped AA 6061 hydroformed tube and corresponding microstructures at points a, b, c and d [62]

Similar to the other forming processes, the frictional behavior in hydroforming is dependent on lubrication and the surfaces of the starting material and the die surface. Hwang et al. tested several lubricants for tube hydroforming and found MoS_2 to be the best option [63].

2.4 Microstructure and Surface Finish of Incremental Sheet Forming

Most of the published work on ISF has been on the manufacturing process, mechanical properties and finite element modeling. There are a limited number of publications on the microstructure and texture of ISF parts [20,64-69]. Hamilton et al. studied the effects of high feed rates and spindle speeds on the microstructure and surface of AA 3003-H14 SPIF parts [66]. The microstructure and surface finish of the undeformed material was compared to five formed parts with different feed rates, spindle speeds and step sizes (Figure 2.10). While all samples had an elongated grain structure, the undeformed material had much coarser grains than the formed parts. Additionally, it was found that step size had a greater effect on the microstructure and orange peel roughness than the other two process parameters. Figure 2.10(4) and 2.10(5) had more refined grains than Figure 2.10(2) and 2.10(3) because they were formed at a smaller step size. Samples produced with higher feed rates and spindle speeds had smaller grains, although the effects of these parameters were harder to isolate than the effect of step size.

Chezian Babu et al. also studied the effects of various process parameters on the microstructure of ISF of AISI 304 steel, testing several step sizes and spindle speeds with a hemispherical tool [65]. The study confirmed a highly strained microstructure with visible stress bands. Radu et al. also found that step size has a more significant effect on surface finish than tool diameter and tool speed [20]. To improve the surface finish, a smaller step size and greater tool speed is an optimal combination. While changes in the microstructure were difficult to see on incrementally formed 99.58% Al, slight deviations in morphology was observed. Grain elongation and refinement was associated with a larger tool diameter, feed rate, spindle rotational speed and smaller vertical step size (Figure 2.11).

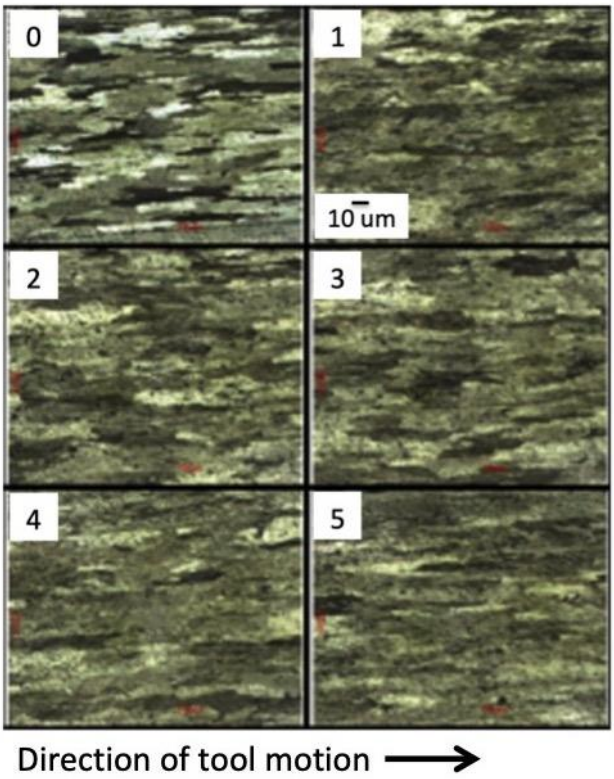

Figure 2.10 Microstructure of the incrementally formed AA 3003-H14 at various feed rates (mm/min), spindle speeds (rpm) and step sizes (mm). (0) Undeformed material, (1) 6985mm/min, 1200rpm, 0.01mm (2) 5080 mm/min, 400rpm, 0.016mm, (3) 8890 mm/min, 2000rpm, 0.016mm (4) 5080mm/min, 2000rpm, 0.004mm, (5) 8890 mm/min, 400rpm, 0.004mm. AA 3003-H14 [66]

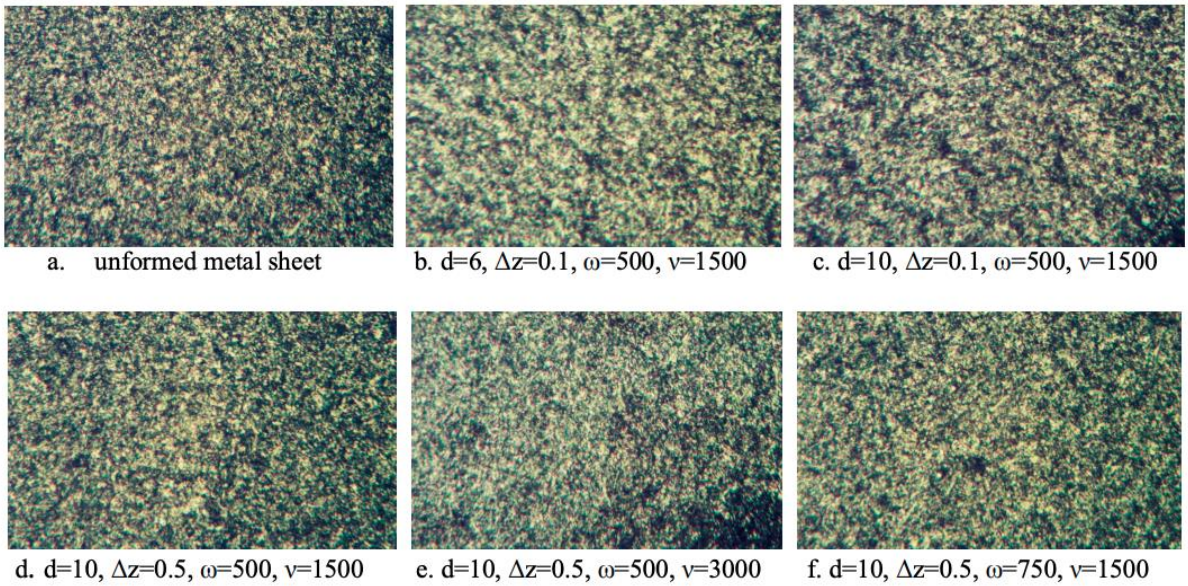

Figure 2.11 Microstructure of incrementally formed 99.58% Al. t=0.8mm [20]

Surface finish studies on incrementally formed parts have evaluated various lubricants and determined the effects of process parameters on surface roughness [34,71-81]. Bhattacharya et al. found that surface roughness decreased with increasing tool diameter, due to the overlap between passes [34]. Roughness also increased with step size up to a certain wall angle threshold, than it decreased. To understand the effects of friction on surface finish, Kim and Park tested a rolling ball tool and static hemispherical head tool, with and without lubrication on AA 1050 [71]. Lubrication with the ball tool gave the best-formed surface without any scratch formation. No lubrication with the hemispherical head tool was the worst combination, leaving the most scratches on the surface. Azevedo et al. studied the influence of lubricants on the final surface finish of parts made of different materials [72]. Using lower viscosity lubricants when forming harder materials such as DP 780 steel led to a better surface finish, whereas using higher viscosity lubricants provided better surface finish when forming softer materials, such as aluminum. Successful lubricants for ISF of AA1050 included SAE 30 oil and AL-M grease. There is still limited work on surface metrology studies other than reporting average surface roughness and evaluating microscale surface features that develop during forming, which are areas this dissertation will address in Chapters 4 and 5.

Chapter 3. Characterizing The Microstructural Evolution During Incremental Sheet Forming

3.1 Introduction

To fully understand how an incrementally formed part will perform under fatigue loading conditions, the microstructure must be well characterized. This is extensively studied for conventional forming processes such as stamping, drawing and hydroforming, as described in the previous chapter. Most of the published work on ISF has been on the manufacturing process, mechanical properties and finite element modeling. There are a limited number of publications on the microstructure and texture of ISF parts. Previous studies demonstrate that the grain structure elongates during forming. Comparing process parameters such as feed rate, spindle speed and step size, it was found that step size had the greatest effect on the microstructure [64-66].

This study focuses on characterizing the microstructural evolution during single point incremental forming of AA 7075-O at room temperature. The grain structure is expected to elongate along the wall of the formed components and localized heating under the tool may lead to incipient recrystallization. To test this hypothesis, characterization techniques including optical and electron microscopy and electron backscatter diffraction (EBSD) were used. Considerable work was done to optimize the sample preparation process for EBSD analysis of the highly deformed specimens. Microstructural results were compared with strain history outputs from a finite element model and preliminary ICME (Integrated Computational Materials Engineering, [75]) collaborations indicate a need for texture prediction models.

3.2 Experimental Methods

3.2.1 Single Point Incremental Forming (SPIF)

A set of SPIF truncated cones was formed by Erika Salem at the University of Michigan on a Standard Modern 1700 Series CNC lathe and a summary of the process parameters used is given in Table 3.1.

Table 3.1 Process parameters used for forming the SPIF truncated cones

Material	AA 7075 - O
Sheet Thickness	1.58 mm
Outer clamping diameter	200 mm x 200 mm
Inner clamping diameter	160 mm
Part opening diameter	140 mm
Tool diameter	12.7 mm
Forming angle	45°, 67°
Forming depth	55 mm
Feed rate	10 RPM (~3700 mm/min)
Step size	0.5 mm
Tool path	Spiral
Lubricant	MoS_2 grease

3.2.2 Characterization Trials – Optical Microscopy

The first samples characterized were from the as-received, undeformed AA 7075-O sheet. Metallographic samples were cut, mounted in Bakelite, mechanically ground and polished to a 1 μm diamond finish on the autopolisher and vibratory polished with 0.03 μm colloidal silica for a finishing step. The silica particles appeared to embed themselves in the aluminum matrix and could not be removed, even with an extensive cleaning process. Eventually, the colloidal silica step was removed from the polishing routine and 1 μm diamond suspension became the final step. The polished samples were then etched to delineate the grain boundaries (Figure 3.1).

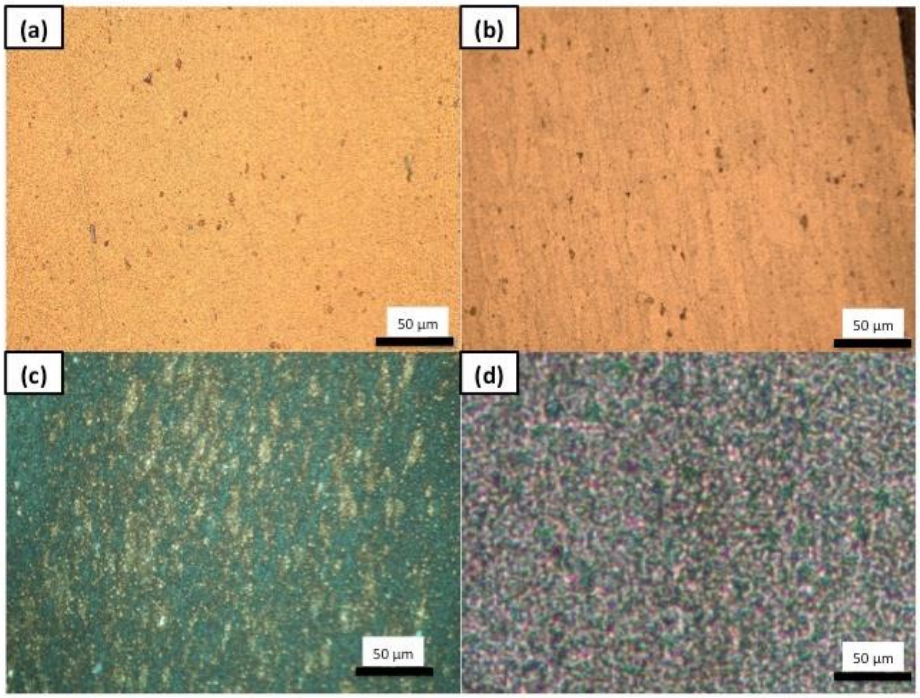

Figure 3.1 Etching trials to delineate the grain boundaries of undeformed AA 7075-O. (a) Caustic NaF etch, (b) Barker's Reagent, (c) Weck's Color Etch, (d) Keller's Reagent

The first etchant tested was the "Caustic NaF" Etch (Figure 3.1a). Samples were immersed in 30-second increments up to 3 minutes, however no grain boundary delineation was observed [83]. The second etchant tested was Barker's Reagent (Figure 3.1b). Samples were electrolytically etched at 20V at room temperature in 30-second increments up to 2 minutes [84]. Some grain boundaries began to delineate but sufficient contrast could not be reached. Additional etching voltage and time led to overetching. The third etchant was Weck's Color Etch (Figure 3.1c). Samples were immersed up to 30 seconds in 5-second increments and the surface was examined under polarized light [83-86]. Some directionality was observed but no grain boundary delineation occurred. A pre-etch of 2g sodium hydroxide in 100 mL distilled water was attempted but did not improve the results. The fourth etchant was Keller's Reagent (Figure 3.1d). Samples were immersed up to 10 seconds in 2-second increments and then up to 2 minutes in 10-second increments [83]. No grain boundary delineation was observed; however,

at 40 seconds, an overetched layer formed on the surface. These optical microscopy non-results were confirmed through correspondence with Robert Kubic, a metallography technician at General Motors who also tried preparing the samples for optical microscopy. His efforts included Barker's reagent, Keller's reagent and the Graff-Sargent etch none of which delineated grain boundaries [87].

It was later found that the sample overetched by Keller's reagent could be used for electron backscatter diffraction (EBSD) analysis, so efforts to visualize the grain structure using optical microscopy ceased and work began on EBSD.

3.2.3 Characterization Trials – EBSD – Preliminary Sample Preparation Techniques

After the first successful EBSD result on the undeformed material, additional studies were done to visualize the grain structure of the incrementally formed material. Vertical cross-sections (Figure 3.2) were sectioned from the cone, mounted in Bakelite, mechanically ground and polished using an autopolisher to a 1 μm diamond finish and overetched with Keller's Reagent. EBSD was performed on a Tescan Mira 3 FEG SEM at an accelerating voltage of 30 kV, a working distance of 16-25 mm, beam intensity of 20 and step size of 0.25-0.5 μm.

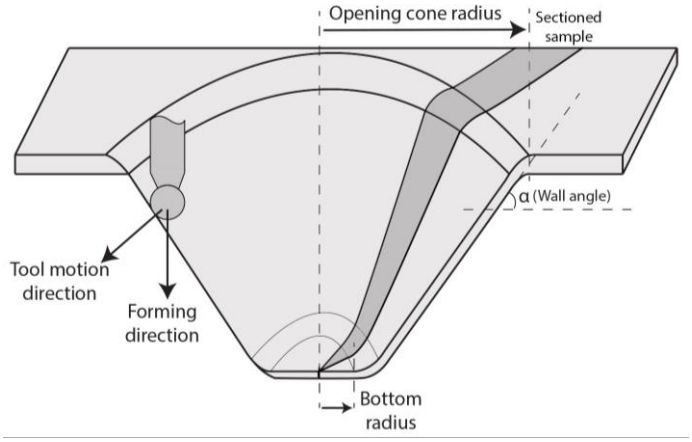

Figure 3.2 Schematic of the truncated cone, highlighting the vertical cross sections that were used for characterization

Samples with more plastic deformation from the forming process did not respond as well to Keller's Reagent. EBSD pattern quality depends on several factors including interaction volume (controlled by the electron beam), sample surface (dependent on particular sample preparation) and crystal orientation (affected by the presence of dislocations) [88]. To improve the surface quality, an electropolishing step on a Streurs Lectro-Pol 5 was added after mechanically grinding and polishing to a 1 μm diamond finish. Electropolishing removes deformation from cutting and grinding; thus, it is commonly used in metallographic preparation of severely deformed materials [89]. The sample surface is smoothened and brightened when the correct combination of electrolyte, voltage, time and temperature is used, generally determined through trial and error, starting with combinations reported in literature. The electrolyte chosen was composed of 80% ethanol, 14% distilled water and 6% perchloric acid, and at room temperature the optimum voltage and time was determined to be 30V and 60 seconds [90-94].

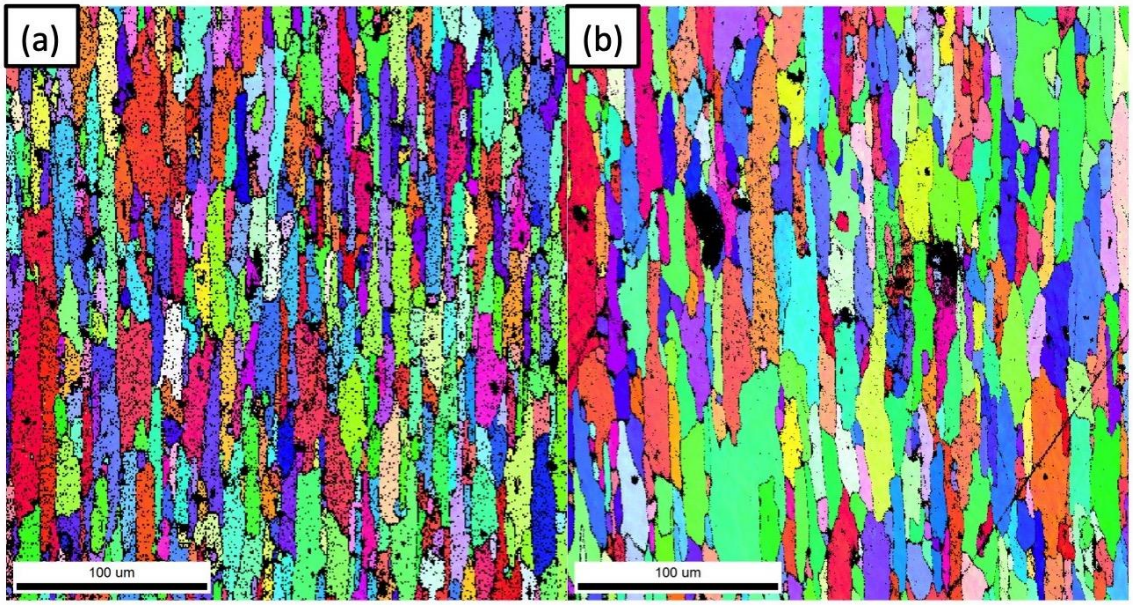

Figure 3.3 EBSD results of the undeformed material when mechanically polished and (a) overetched with Keller's Reagent and (b) electropolished. More grain structure is resolved from the electropolished sample than the overetched sample.

Figure 3.3 shows the differences in amount of resolvable grain structure in the as-received, undeformed material obtained from overetching with Keller's Reagent (Figure 3.3a) and electropolishing (Figure 3.3b). EBSD orientation maps of the electropolished surface resolved more of the grain structure and had fewer regions of low confidence index (CI), which is a measure of how certain the software deems a point to be at a given orientation. The average CI of the EBSD data from the mechanically polished sample, given by the software, is 51% and from the electropolished sample is 63%. The only data post-processing was a CI partition, where points below 10% certainty (CI < 0.1) were eliminated from the data set and appear as black regions in the EBSD orientation maps [95,96].

Even though electropolishing significantly improved the quality of the EBSD orientation map of the as-received material, it did not fully resolve the grain structure of the deformed material. Increased plastic strain generates more dislocations that locally perturb the diffracting lattice planes. Bragg's diffracting condition is hardly satisfied and incoherent scattering occurs, degrading the diffraction pattern [88,97]. This effect is one of the largest challenges for examining severely deformed materials. For example, Jorge-Badiola et al. encountered this in their study of hot worked steel [98]. Samples were deformed to 50% strain by torsion tests and examined by EBSD. As the amount of strain increased, the definition and the ability to determine several microstructural parameters including grain size and misorientation angles broke down. Yong-jun et al. studied materials processed by severe plastic deformation and encountered several non-indexed (or low CI) points in the heavily deformed areas [89]. To avoid black regions in their EBSD maps, the field of view was reduced to ~20 μm x 20 μm and diffraction patterns were taken more frequently (smaller step size).

3.2.4 Characterization Trials – EBSD – Improved Sample Preparation Technique

Being able to resolve the grain structure of the highly deformed material was still of high interest, especially to determine what was occurring in the black regions, which was believed to be severe grain refinement or incipient recrystallization. Additionally, it was unclear whether overetching with Keller's Reagent or electropolishing was preferentially etching the samples, so the sample preparation technique needed further refinement.

To eliminate the possibility of preferential etching, final polishing with colloidal silica was attempted again. In order to make sure the silica particles were not embedding themselves into the matrix, a colloid with a larger particle size (0.06 μm) was chosen, polishing was done on the autopolisher where it could be tightly controlled and an extensive cleaning routine was put in place. It was found that controlling the force and speeds of the autopolisher mimicked the effect of the vibratory polisher and allowed for shorter times to be used at each step. A technique was developed where the polish became gentler over time – at each step, the colloidal silica chemically removed a layer of the damaged surface and the mechanical polish swept away that layer. After several iterations, the surface and sub-surface became damage free, which allowed for better EBSD pattern quality. Figure 3.4 shows the improvement in EBSD quality with this sample technique, which is outlined in Table 3.2.

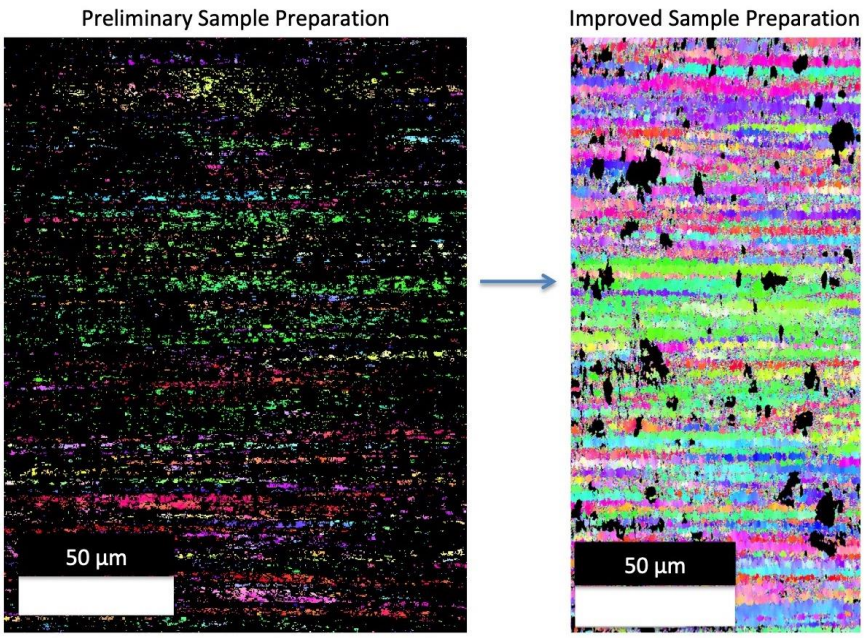

Figure 3.4 Improvement in EBSD quality of the highest strained region (~72% thickness) with the refined sample preparation technique outlined in Table 3.2

Table 3.2 Improved EBSD sample preparation technique for resolving more of the grain structure of the highly deformed material

Grit / Particle	Time (min)	Head Speed (RPM)	Base Speed (RPM)	Force (N)	Rotation ***
400*	0:40	60	150	25	Co-
600*	1:30	60	150	25	Co-
1200*	1:30	60	150	25	Co-
9 µm**	5:00	40	120	15	Counter-
3 µm**	7:00	40	120	15	Counter-
1 µm**	7:00	40	120	15	Counter-
0.06 µm Colloidal Silica^	5:00	40	120	15	Counter-
0.06 µm Colloidal Silica^	5:00	40	80	15	Counter-
0.06 µm Colloidal Silica^	15:00	40	50	15	Counter-
0.06 µm Colloidal Silica^	15:00	40	50	10	Counter-

* After each step, rinse samples and holder with water and dry with compressed air.

** After each step, rinse samples with water, clean them in water in the ultrasonic cleaner for 5:00 and dry with compressed air. Rinse holder with water.

^ Colloidal silica should be done with one sample in the holder at a time. All steps should be done consecutively. Repeat the final step as needed. After each step, immediately rinse the sample with water for 0:20. After the final step, immediately rinse with water for 0:20, place sample back in the autopolisher and run with water for 1:00. Remove the sample and immediately soak in water. Clean the sample in ethanol in the ultrasonic cleaner for 5:00 and dry with compressed air.

*** Relative rotational direction between the autopolisher head and base.

3.3 Microstructure Evolution with Strain

The microstructure and texture of the undeformed sheet material is given in Figure 3.5. The grain structure is slightly elongated, residual from the original sheet rolling process and the texture is fairly weak.

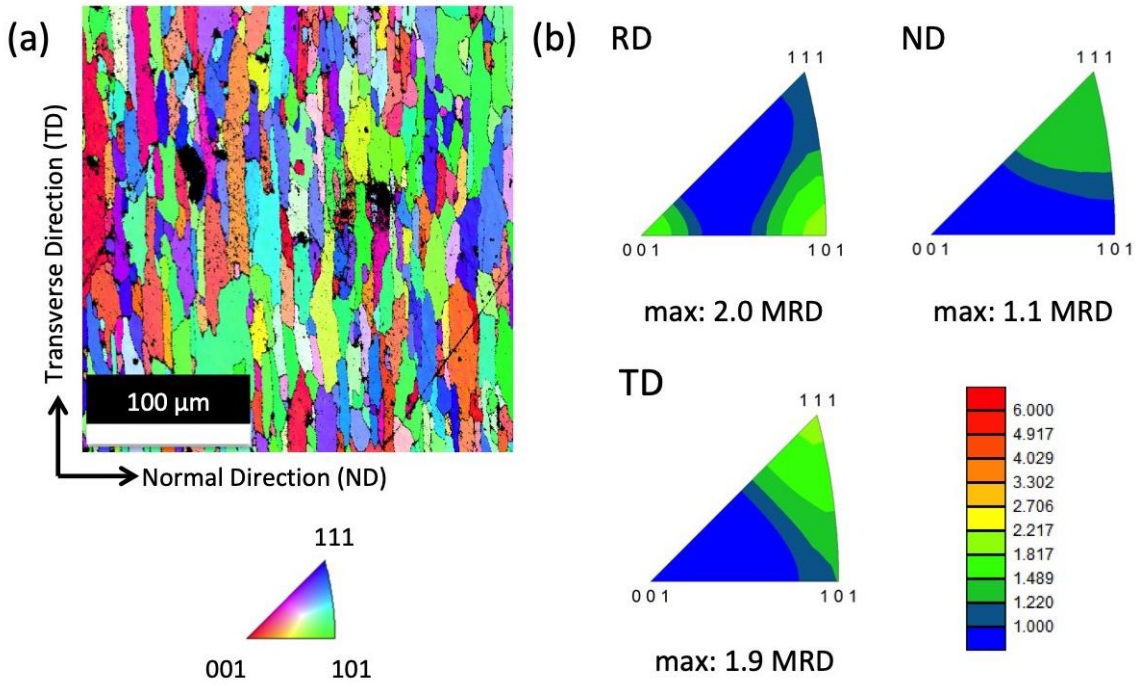

Figure 3.5 (a) Microstructure and (b) texture of the undeformed AA 7075-O sheet material. RD = rolling direction, ND = normal direction, TD = transverse direction. EBSD step size = 0.4 µm

To examine the microstructure of the 45° and 67° SPIF cones, samples were cut (Figure 3.2 for schematic, Figure 3.6 for images) and their cross-sections were measured to create thickness profiles [21], which were compared to the thickness predicted by the sine law. Strain profiles were generated using the measured thickness reduction (Figure 3.6 [22]).

For the 45° cone, point A corresponds to the location of initial tool contact at a thickness of 1.58 mm. A region of monotonically reducing thickness follows as the material bends until a steady state thickness of ~1.1 mm is reached, shown by point B. The steady state thickness agrees with that predicted by the sine law [31].

For the 67° cone, point A corresponds to the location of initial tool contact at a thickness of 1.58 mm. A region of bending follows, labeled as point B. The material decreases in thickness further into a region of thinning beginning at point C, reaches a minimum thickness of ~0.45 mm at point D, and then increases in thickness until a steady state is reached around point E, ~0.61 mm. Similarly to the 45° cone, the steady state thickness agrees with the sine law prediction.

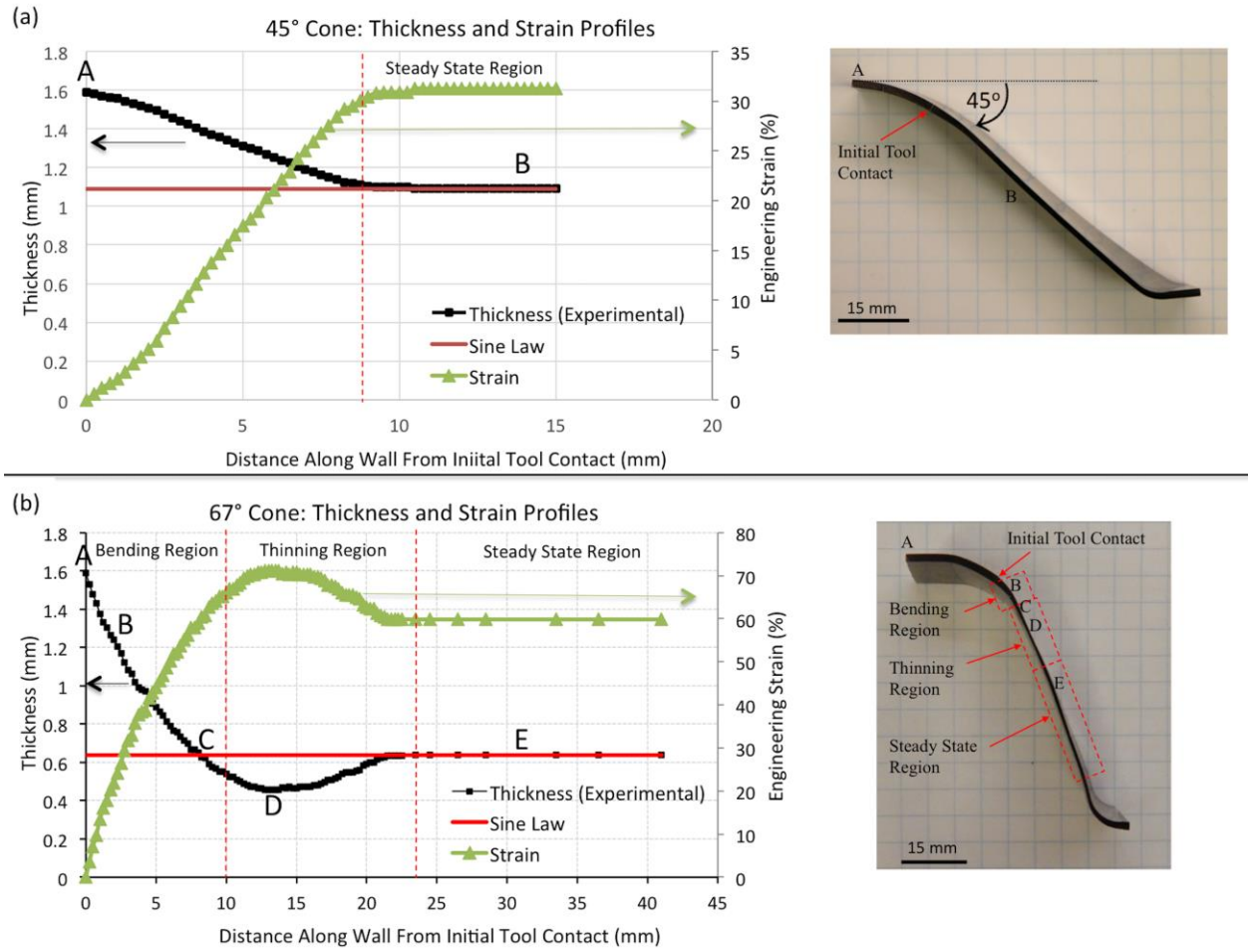

Figure 3.6 Thickness (experimental and sine law-predicted) and strain profiles for the (a) 45° and (b) 67° SPIF cones. Profiles are on the left and images of the samples are on the right [22].

EBSD results for the undeformed and steady state regions along the cross section of the 45° cone are shown in Figure 3.7. The transverse direction is parallel to the direction of elongation and the direction of tool motion is in/out of the page. The undeformed region shows slightly

elongated grains most likely residual from the rolling process, with an average grain width of 13.8 μm and an average grain length of 62.3 μm. The steady state region occurs at ~31% strain, which is calculated from thickness reduction. Most of the grain structure can be resolved, exhibiting enhanced grain elongation. The average grain width is 10.4 μm and the average grain length of 89.2 μm.

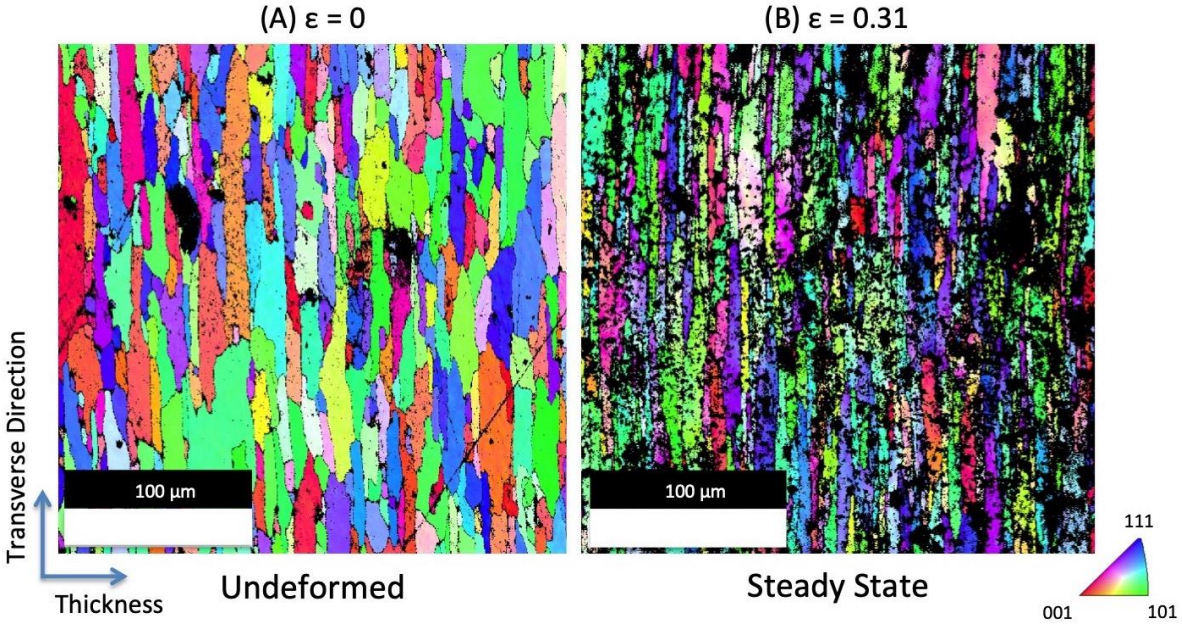

Figure 3.7 Microstructure results for the 45° SPIF cone at the (A) undeformed region and (B) steady state region. The transverse direction is parallel to the direction of elongation and the direction of tool motion is in/out of the page. EBSD step size = 0.4 μm

EBSD results for the undeformed, bending, maximum thinning and steady state regions along the cross section of the 67° cone are shown in Figure 3.8. The evolution is shown in terms of increasing strain, calculated again from thickness reduction. The transverse direction is parallel to the direction of elongation and the direction of tool motion is in/out of the page. The undeformed region is consistent with the previous cone. The bending region follows at ~12% strain, and while the grains have re-oriented, they have not significantly elongated. The average grain width is 12.4 μm and the average grain length of 62.7 μm. The steady state region occurs

at ~61% strain, with an average grain width of 8.8 μm and the average grain length of 172 μm. The thinning region has the largest amount of deformation at ~72% strain. The average grain width is 6.7 μm and the average grain length of 223 μm. Examining the through-thickness gradient at the steady state and bending regions, it is clear that the grains are being refined with increasing strain. Additionally, the morphology of the grains suggests no evidence of recrystallization, especially close to the surface, is observed.

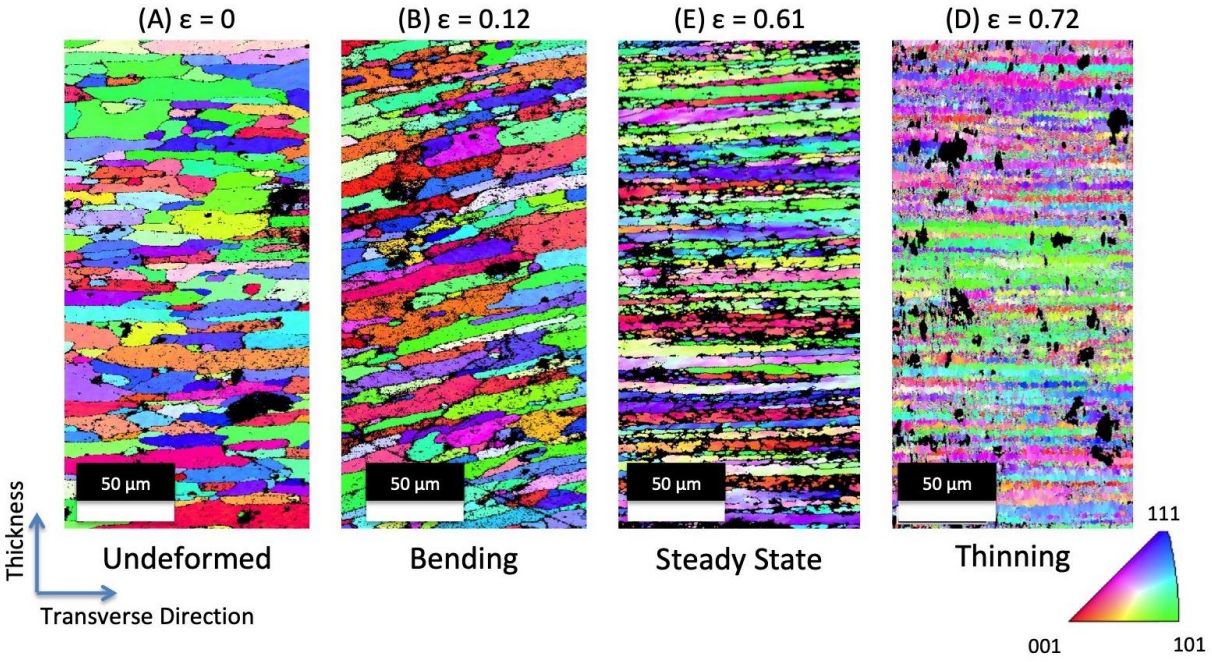

Figure 3.8 EBSD results for the 67° SPIF cone at the (A) undeformed, (B) bending, (C) steady state and (D) thinning regions. The transverse direction is parallel to the direction of elongation and the direction of tool motion is in/out of the page. EBSD step size = 0.25-0.4 μm

Comparing the microstructural features with strain (thickness reduction), it is apparent that grain width decreases linearly and grain length increases linearly with increasing strain (Figure 3.9 and Figure 3.10). This behavior corresponds to the grain elongation observed in the EBSD maps and suggests that the grains are elongating proportionally to the stretch of the sheet. Additional data points were added from components also formed from AA 7075-O at room temperature, including deep drawn cups drawn to ~30% strain, TPIF "heart shape" specimens

with a 38° flat wall at ~20% strain (Appendix A) and a SPIF variable angle funnel from 30-55% strain. Error bars are made with standard deviation.

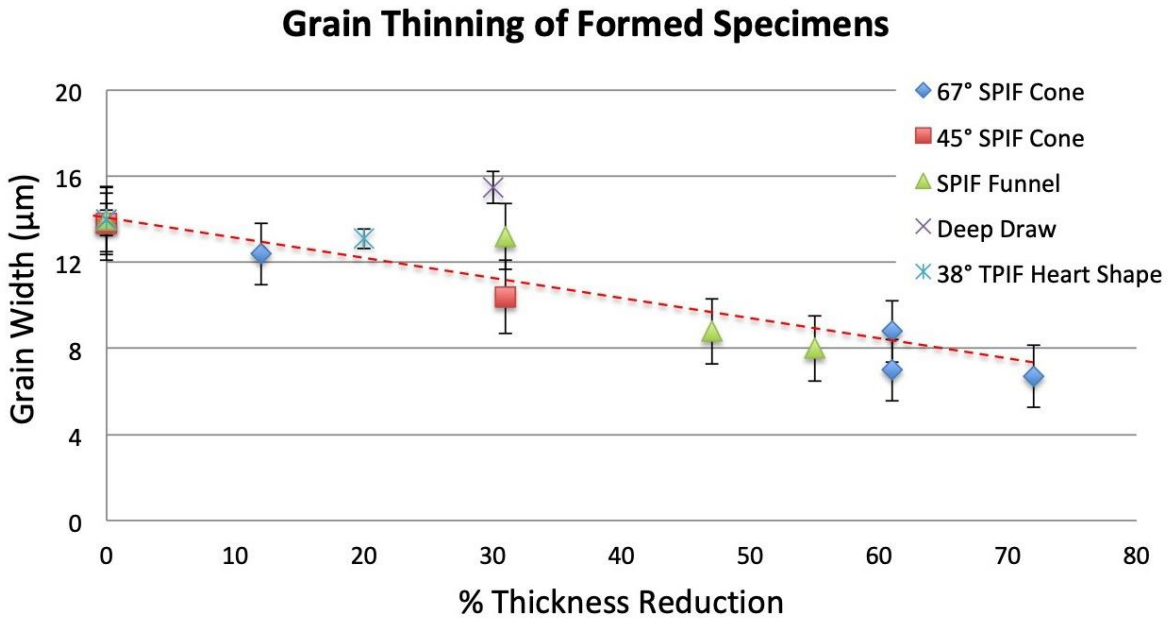

Figure 3.9 Grain thinning (refinement of grain width) with increased thickness reduction. AA 7075-O, Room temperature

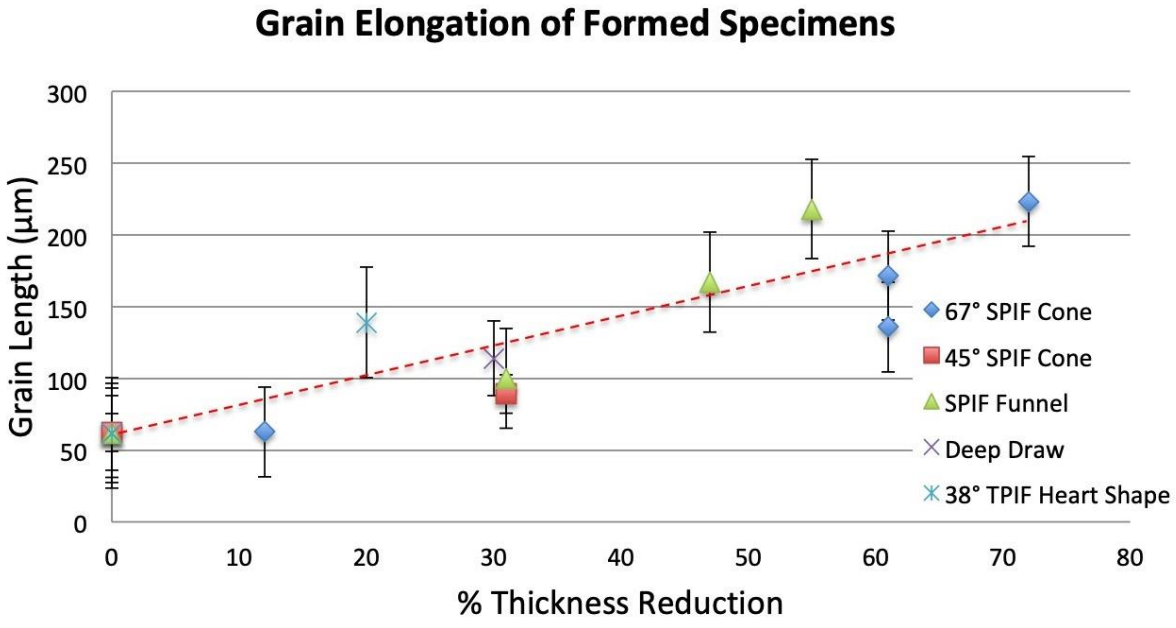

Figure 3.10 Grain elongation with increased thickness reduction. AA 7075-O, Room temperature

Aspect ratio, calculated from grain length and width, increases monotonically with increasing strain (Figure 3.11). An additional data point from Tajally *et a*l. of AA 7075-O that was cold rolled to 71% strain is included and agrees with the observed trend [60].

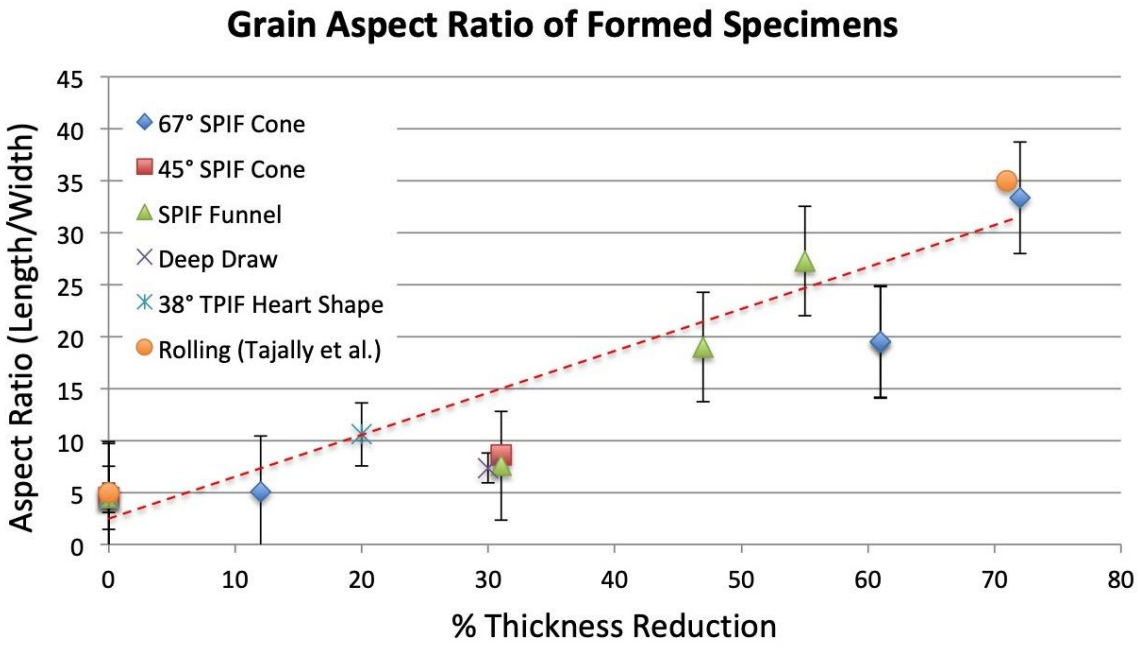

Figure 3.11 Grain aspect ratio (calculated from measured lengths and widths) with increased thickness reduction. AA 7075-O, Room temperature

3.4 Effects of Strain History

The thickness profiles from Figure 3.6 were also used as validation criteria for the ISF finite element model (FEM), which allowed for the microstructure results to be compared to its strain outputs. In particular, the strain histories for points C and E on the thickness profile in Figure 3.5b were compared. The two points are at equivalent strains, before and after the thinning band in the 67° SPIF cone. The aspect ratios are almost the same and the grain structures are very similar (Figure 3.12). The slight change in grain directionality between the EBSD maps and the variation in black regions are believed to be due to small sample mounting and preparation inaccuracies and not due to material or process conditions.

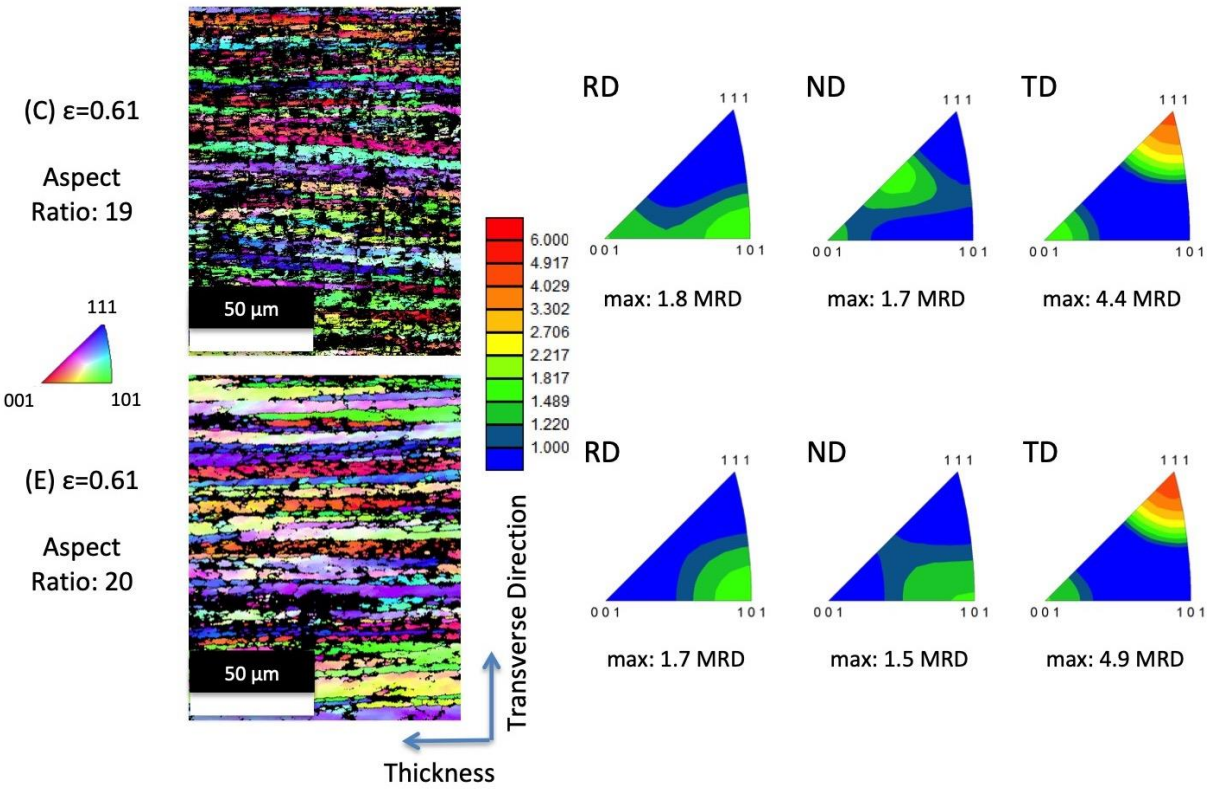

Figure 3.12 Aspect ratio (left), EBSD orientation maps (middle) and texture plots (right) of points C and E, two regions at the same strains (calculated from thickness reduction) of the 67° SPIF cone, AA 7075-O. RD = rolling direction, ND = normal direction, TD = transverse direction. EBSD step size = 0.35 µm

The textures are also very similar at both locations; the <111> and <001> textures are dominant with respect to TD and there are some variations between the weaker textures. These textures are similar to those that develop during uniaxial tension. Savoie et al. studied texture development during uniaxial tension of AA 1XXX and AA 5XXX alloys and the <111> and <100> type fiber textures appeared with respect to the deformation axis [53]. Given that aluminum has a face-centered cubic crystal structure and deforms by slip along {111}<110>, these results make sense. Additionally, Figure 3.12 depicts other texture variants appearing in the incrementally formed samples. This is because ISF has a more complex strain path than uniaxial tension, as seen in the FLC in Figure 2.3b; the strain path is not solely uniaxial tension, pure shear or plane strain. To further understand the texture development, EBSD analysis

should be performed on sheet material undergoing biaxial deformation, which would be more representative of ISF. Bulge testing is a possible test method and preliminary work was done to compare surface finish at equivalent strains to ISF [23]; further work on texture analysis should be completed.

It can be hypothesized from the microstructure results in Figure 3.12 that the strain histories at points C and E are similar. To test this, strain histories from the ISF FEM, generated and run by Jaekwang Shin at the University of Michigan, at points A-E from Figure 3.6b were plotted (Figure 3.13, [22]). An element located at the middle of the sheet in the regions of interest was chosen and tracked from the point of initial tool contact through when the tool leaves the region. The three normal strain components were plotted: circumferential; along the formed wall; and thickness reduction. The circumferential strain does not vary significantly and is considered negligible for this study. In contrast, the strains along the formed wall and due to thickness reduction vary greatly, which corresponds to the displacement of the tool.

The minimum principal strain in the steady state region (Figure 3.13c, curve E), exhibits increasing compressive strain after initial tool contact. After the tool leaves the region, the strain plateaus. The maximum principal strain (Figure 3.13a) is along the wall. That direction is under tension as the material stretches and results in the grains elongating. Comparing points C and E shows that the strain histories are similar in shape. The magnitude of the strain when the tool comes into contact with the sheet is very similar for both points and the slopes when the tool is entering and leaving the regions are very similar. The different final strain values reflect different phases of the forming process.

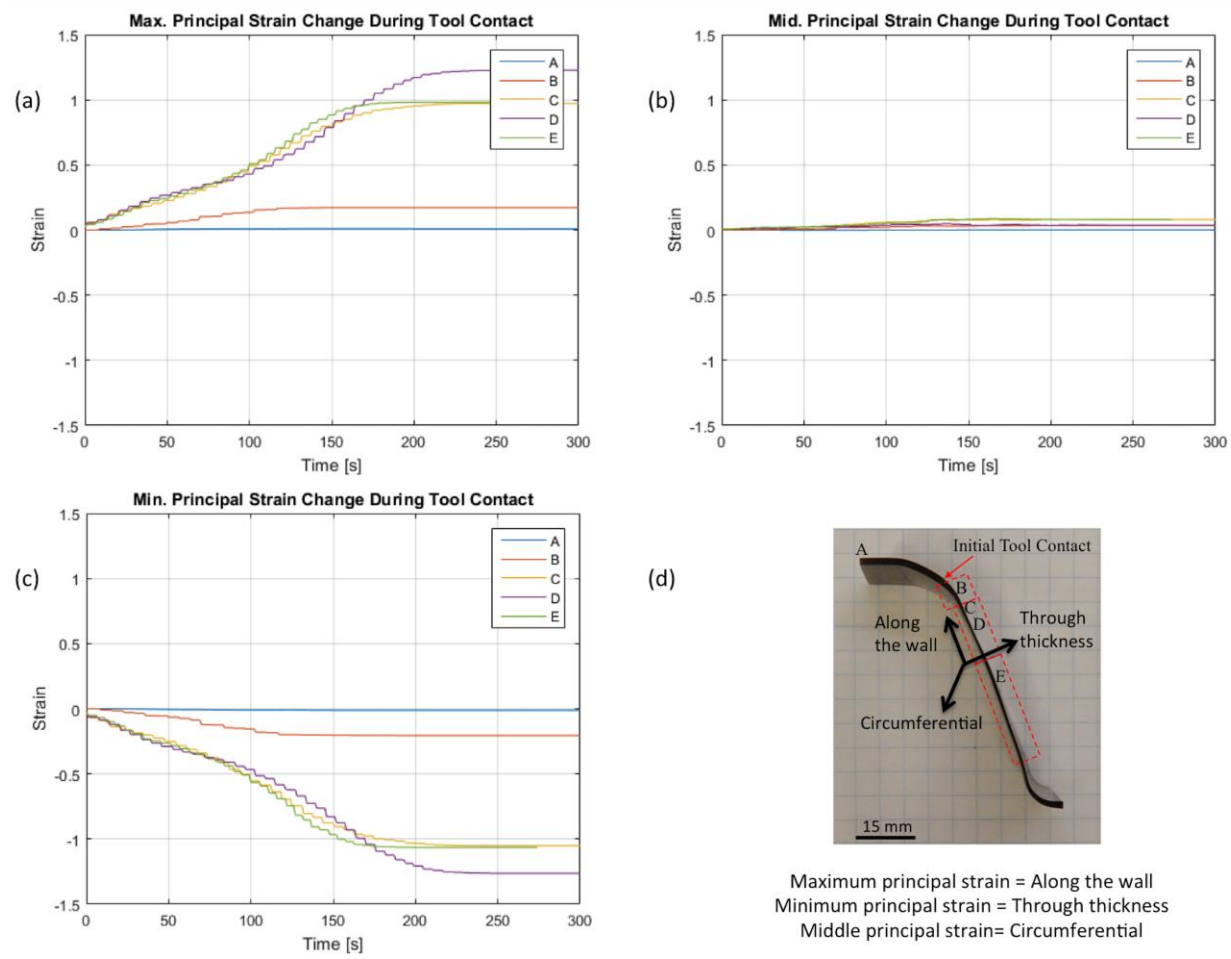

Figure 3.13 Strain history of the 67° SPIF cone during tool contact from the FEM. The elements chosen correspond to the locations of EBSD analysis. (a) Along the wall strain, (b) Circumferential strain, (c) Through thickness strain, (d) Sample with orientation marked [22]

These results indicate similar strain histories induce similar microstructure and texture. To test the effects of varying strain history, AA 7075-O samples were deep drawn to a similar equivalent strain by Jeremy Lipshaw and Dr. Tracy Berman at the University of Michigan at room temperature on an Erichsen Universal Sheet Testing Machine. EBSD analysis was done and the grain morphology and textures were compared (Figure 3.14). The grains appear larger along the deep drawn cup and there is a difference in the observed textures. It is known that deep drawing leads to more complicated textures; further work beyond the scope of this thesis

should be done to understand this phenomenon. It also indicates a need for texture prediction modeling and the following section will show preliminary results.

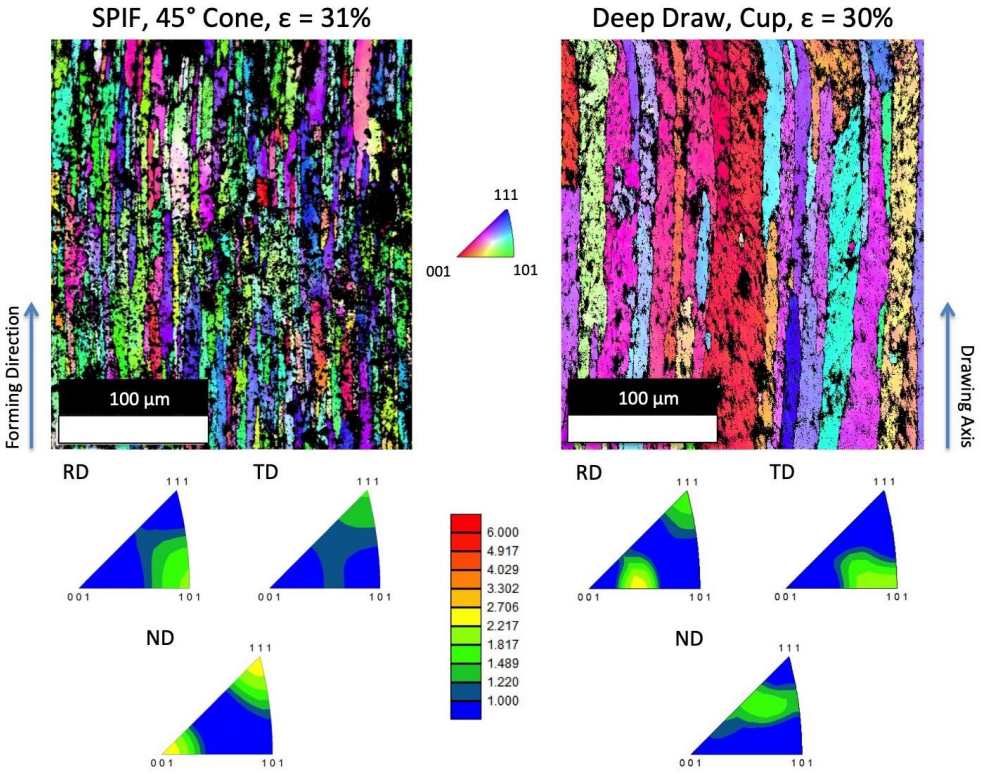

Figure 3.14 Microstructure and texture results for a 45° SPIF cone at 31% strain (left) and deep drawn cup at 30% strain (right), AA 7075-O. RD = rolling direction, ND = normal direction, TD = transverse direction. EBSD step size = 0.4 µm

This dissertation work concentrated on using EBSD to study the microstructural evolution during forming, specifically through-thickness showing grain elongation as well as any potential grain size gradient. It is worth mentioning that two-dimensional EBSD is not the only way to study this phenomenon. A three-dimensional reconstruction of the microstructure could be done with serial sectioning of the sample and performing EBSD on each slice. A highly controlled method to consistently polish away the same amount of material is needed to build the 3D microstructure. Higher resolution characterization techniques, including Transmission Kikuchi Diffraction and Transmission Electron Microscopy would allow characterizing the grain structure at a much smaller scale, investigating second phases that pin

grain boundaries during deformation and resolving and quantifying dislocation density. Using the sample preparation technique detailed in this dissertation work, any of these methods would be highly useful to further understand the microstructural behavior. Additionally, non-destructive techniques, such as 3D X-Ray Microscopy and Computed Tomography could resolve the microstructure at the surface, something that isn't possible with EBSD or other microscopy techniques that require polishing away material for an optimal sample surface. These techniques could also identify pores or other sub-surface defects that could be failure initiating.

3.5 ICME Collaborations for Texture Modeling

Preliminary work developing ICME tools for texture prediction using experimental EBSD results from this thesis were performed in collaboration with Professor Farhang Pourboghrat's group at The Ohio State University and Professor Veera Sundararaghavan's group at the University of Michigan. Professor Pourboghrat's group used experimental EBSD results from this dissertation work (Appendix B) to develop a representative volume element for their crystal plasticity finite element model (CP-FEM) and simulated the textures at the undeformed and steady state regions of the 67° SPIF cone. Professor Sundararaghavan's group used the EBSD results and predicted the same textures from a first principles approach. The three sets of textures are compared in Figure 3.15. Further work beyond the scope of this thesis should be done to strengthen these models.

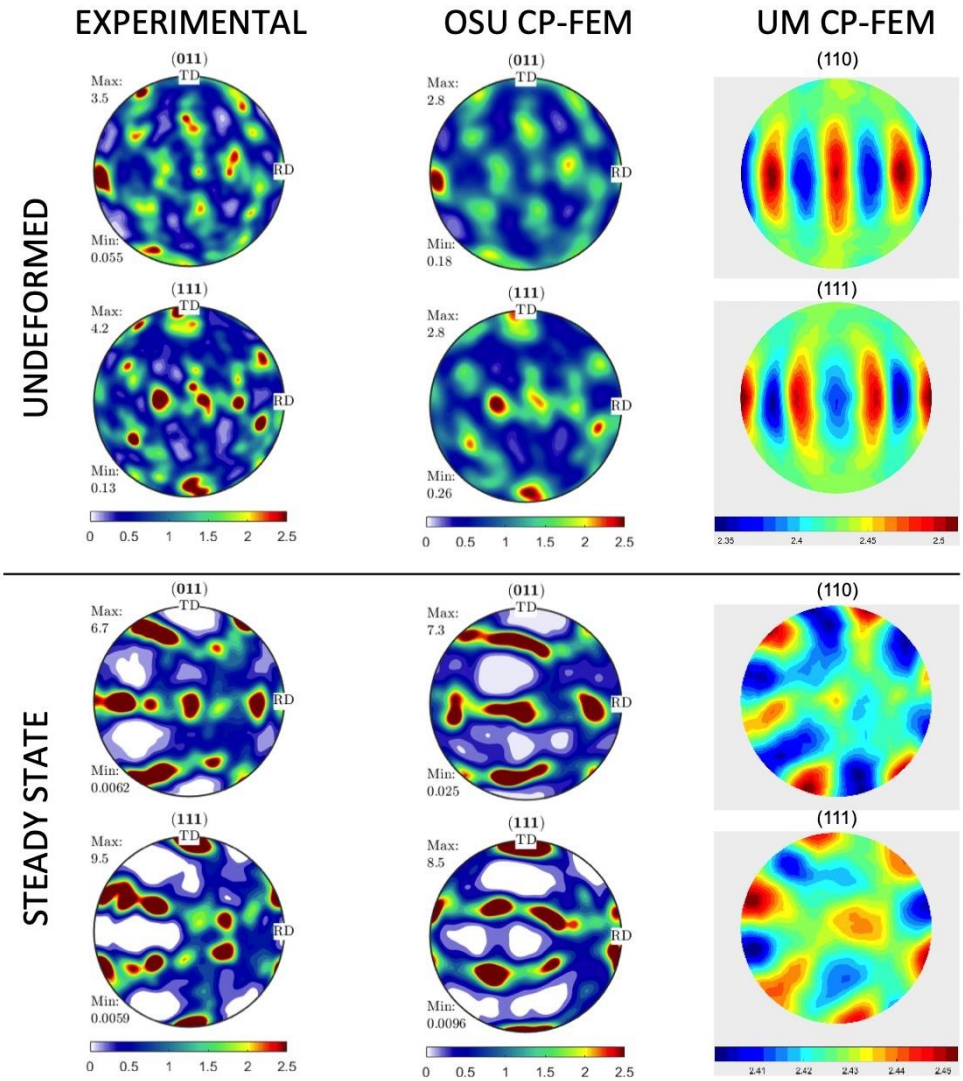

Figure 3.15 Experimental (left), CP-FEM from OSU (middle) and CP-FEM from UM (right) texture results for the undeformed (top) and steady state (bottom) regions of a 67° SPIF cone, AA 7075-O, Room temperature

Chapter 4. Studies In Surface Metrology Of Incrementally Formed Parts

4.1 Introduction

Characterizing the surface of incrementally formed parts is important for understanding how a part will perform under cyclic fatigue loading; any surface defects could be failure initiating. Much work has been done on measuring the surface roughness of formed components and identifying good lubricants [20,34,66,71-81]. Preliminary surface roughness measurements were done on the samples used for this dissertation work to confirm the behavior agreed with what has already been reported. These results were successful, but led to several unanswered question regarding the interaction between the forming tool and metal sheet: is surface finish uniform throughout the fabricated part or are there local differences; what is the impact of tool geometry on the macroscopic surface features; and how is material moved during fabrication. Before fully characterizing the surface finish at the microscale, these questions must first be answered.

This chapter addresses several of those questions using optical profilometry and scanning electron microscope (SEM) imaging for TPIF of AA 7075-O at room temperature. Roughness measurements and images of the surface indicated variations in the surface finish, even within a single tool striation. To understand this phenomenon, the tool geometry was compared to that of a single tool striation and contact between the tool and sheet was investigated. It was found that there were inconsistencies in the amount of contact between the tool and sheet, which prompted further examination into how the material moves during the forming process.

4.2 Experimental Methods

4.2.1 Two Point Incremental Forming

A set of TPIF heart-shaped specimens (Figure 4.1 [24]) was formed by Ankush Bansal at the University of Michigan from AA 7075-O sheet on a Cincinnati HMC 400 EP CNC milling machine at room temperature. The process parameters are summarized in Table 4.1.

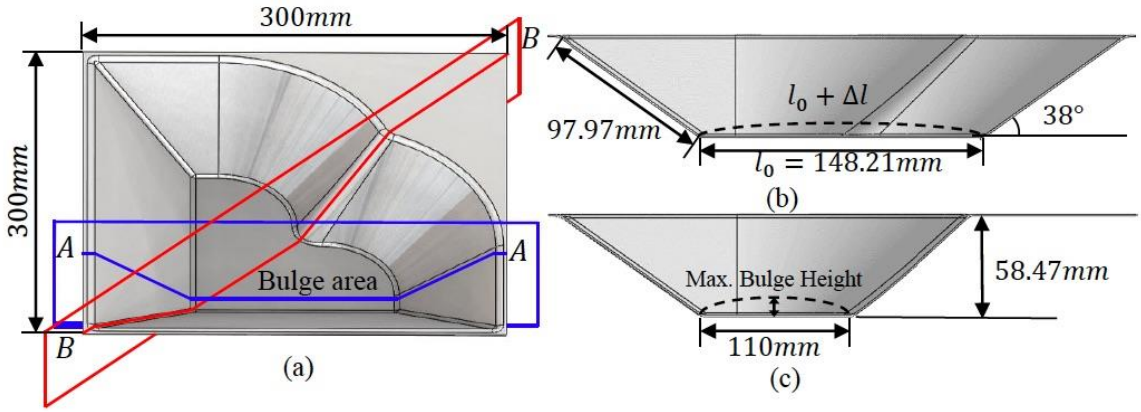

Figure 4.1 Geometry of the TPIF heart-shaped specimens with two flat walls, two curved regions and several fillets: (a) full part; (b) cross section A-A; (c) cross section B-B [24]

Table 4.1 Process parameters used to form the TPIF heart-shaped specimens

Material	AA 7075 - O
Thickness	1.64 mm
Tool diameter	8 mm
Forming angle	38°
Forming depth	59 mm
Feed rate	100 in/min
Step size	0.25, 0.5, 0.63 mm
Effective Squeeze Factor	0 – 5%
Tool path	Contour
Lubricant	MoS_2 grease

4.2.2 Tribology "Scratch Test"

The samples characterized to study material movement during fabrication were formed by a "scratch test," performed by Ankush Bansal on AA 7075-O sheet to mimic a wear test on the TPIF setup (Figure 4.2). The sheet was mounted against a die with a large flat surface and a tool was run in a single, straight line at a defined initial force. It is important to note that the milling machine is displacement controlled, not force controlled, resulting in an increase in force up to 250 N during the test. Two scratches were formed per force, without overlap. Three initial force levels were tested using two different tools. A summary of the test parameters is found in Table 4.2. The region most representative of the defined force is the point of tool contact at the beginning of the scratch. Analysis was done there and at the end of the scratch, to quantify the amount of material displaced. Results are given in Section 4.5.

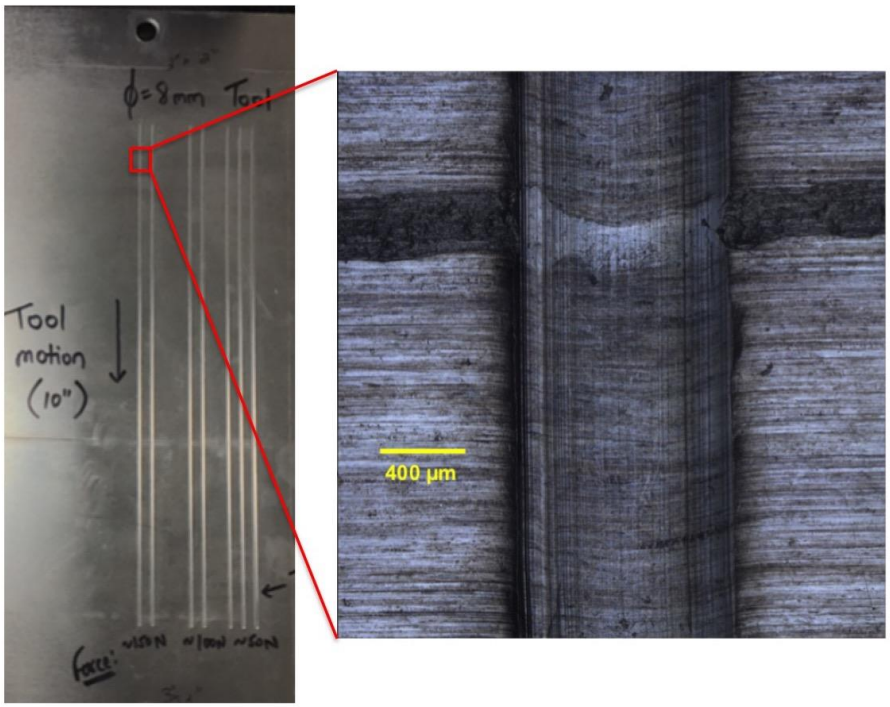

Figure 4.2 Tribology "scratch test" with a 8mm tool and initial forces from 50-150N. The same test was run with a 4 mm tool. AA 7075-O

Table 4.2 Process parameters used for the "scratch test"

Material	AA 7075-O
Thickness	1.64 mm
Tool Diameter	4, 8mm
Initial Forces	50, 100, 150 N
Scratch Length	254 mm

4.2.3 Materials Characterization

Surface finish samples, 15 mm x 15 mm, were cut from the center of the flat walls. The samples were cleaned with ethanol in the ultrasonic cleaner. Optical imaging and surface profile measurements were done on an Olympus DSX510 Digital Microscope. SEM imaging was done on a Tescan Mira3 FEG SEM at an accelerating voltage of 10 kV, beam intensity of 11 and working distance of 10 mm. Data was taken on the tool and non-tool sides of the formed parts.

4.3 Variability in Surface Finish

The surface roughness of incrementally formed parts increases with increasing step size, increasing tool speed and decreasing tool size [20,34]. Preliminary roughness measurements on these TPIF heart shaped specimens, as well as the SPIF cones detailed in Chapter 3, agreed with the reported trends (Appendix C). The surface profiles consistently had a periodic shape, as shown in Figure 4.3a. The larger wavelength features are classified as tool path striations; features created by the tool during forming that are parallel to the direction of tool motion and have a spacing of the step size, with respect to the wall angle (Figure 4.3b). The smaller wavelength features are the surface roughness and can be seen along the peaks and valleys of the individual striations. Additional striations that are residual from the original rolled sheet also exist.

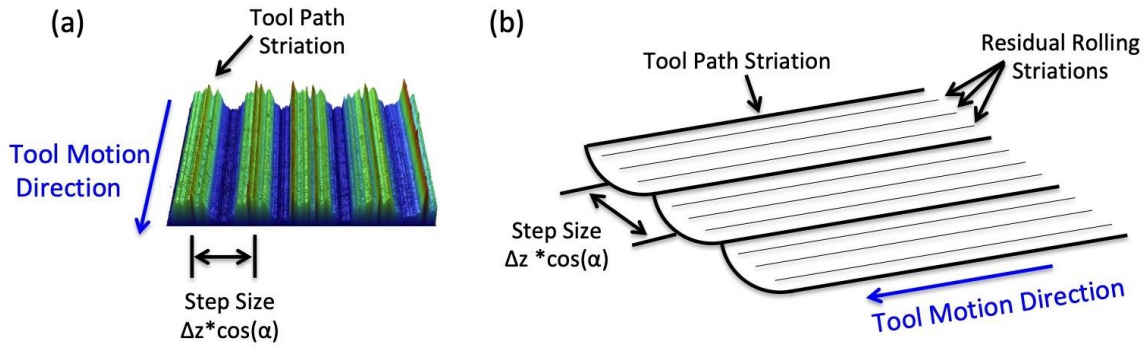

Figure 4.3 Surface profile (a) and schematic (b) of a tool path striation. Striations are parallel to the tool motion direction and have a spacing of the step size with respect to the wall angle. Striations residual from the rolled sheet also exist.

After the profiles were taken, the samples were imaged in the SEM for higher resolution images of the surface. Figure 4.4a captures two tool striations; the periodicity can be seen in the features that have developed on the surface. Generally, surface roughness is reported as an average over a field of view. However, when tilting the sample, it becomes apparent that two modes of roughness exist, seen in Figure 4.4b. Thus, it might be necessary to report roughness at the peaks and valleys of the tool striations separately.

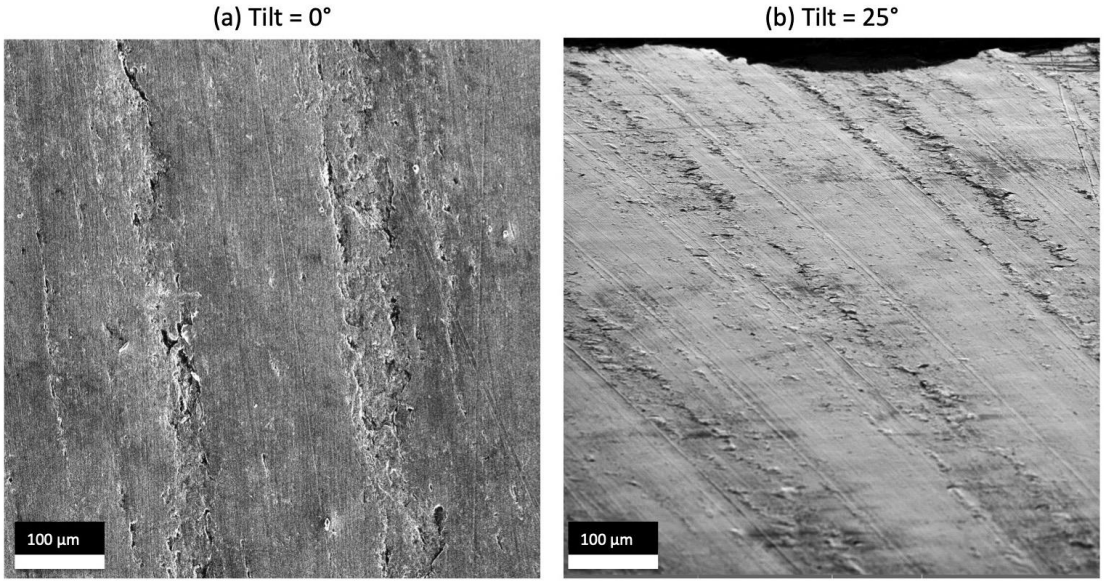

Figure 4.4 SEM images of the as-formed surface where (a) the sample is not tilted and (b) tilted to 25°. TPIF, Heart Shape, Δz = 0.25mm, AA 7075-O

To test this, surface roughness was calculated from line profiles for heart shaped specimens at 0% and 5% effective squeeze. For calculating the average roughness, 10 line profiles parallel and perpendicular to the tool striations were measured and averaged for each sample. In contrast, for calculating roughness along the peaks and valleys separately, 10 line profiles were measured parallel to the tool striations, strategically placed at either the peaks or valleys. Table 4.3 summarizes the results.

Table 4.3 Surface roughness results for the TPIF heart shaped specimens

	0% Effective Squeeze		5% Effective Squeeze	
	Tool	Die	Tool	Die
Average	0.196 +/- 0.020	0.284 +/- 0.047	0.215 +/- 0.035	0.2676 +/- 0.035
Peak	0.196 +/- 0.020	N/A	0.244 +/- 0.012	N/A
Valley	0.192 +/- 0.016		0.203 +/- 0.010	

The die side was consistently rougher than the tool side. The average roughness was not significantly different than the peak and valley roughness for the 0% squeezed sample. Slight deviations were seen in the sample squeezed to 5%. This data shows that it is not necessary to report roughness at the peaks and valleys separately, but best practice would be to measure line profiles parallel to the direction of tool motion.

4.4 Tool and Striation Geometry Comparison

As mentioned earlier, the surface profiles indicated two modes of features; larger wavelength features correspond to tool path striations and smaller wavelength features correspond to surface roughness. To quantify the metrics of the tool path striations, the waviness was isolated from the surface profile and used for the calculations. Waviness is generally defined as irregularities of a longer wavelength caused by tool marks or improper manufacture [99]. In the case of ISF, it is caused by the localized deformation of the forming tool. It can be filtered from the full profile data as given in Equation 4-1,

$$W_e(\lambda) = 1 - R(\lambda) \quad \text{(4-1) [99]}$$

where $W_e(\lambda)$ is the waviness and $R(\lambda)$ is the roughness.

To quantify the metrics of the profiles including the height, depth and spacing of a striation, a measurement procedure and data analysis code was developed to process the raw data. A 3D image is captured on the Olympus microscope at a field of view large enough to encompass at least a single tool striation. Standard surface correction is performed in the software to remove the effects of the bulk sample curvature. Line profiles are measured and the waviness is isolated using the software. The waviness is then filtered so a single striation is in view and exported into a CSV file, which is then imported into MATLAB. The step size and wall angle of the part being analyzed are input into the code, which is then run. Outputs include striation height, depth and spacing as well as a graph of the tool striation and best-fit line. It calculates these metrics by identifying the two tallest peaks in the field of view as striation endpoints and analyzing them and everything in between in matrix form using a linear regression function. It also is able to average over several line profiles, so an average value for a given field of view can be calculated.

After observing the variations in surface roughness even within a single tool striation (Figure 4.4), it became necessary to determine how the tool geometry compared to that of the tool striation. Superimposing the tool geometry on a single striation, using the code previously described, allowed for that comparison as well as observation of how much the tool was in contact during forming. Preliminary measurements found the striations to be hemispherical in shape and the tool tip design is also hemispherical; it was expected that the geometries would match well.

Figure 4.5 details the results of this comparison. It is best to compare the best-fit line of the striation with the tool geometry, as the raw profile includes extra noise. In Figure 4.5a, it can be seen that the tool and striation geometries match well, as expected. Focusing on the striation valley in Figure 4.5b, it can be seen that the tool tip is in contact with the center of the striation. On either side, outside the center zone, a loss of contact is observed. This figure in particular shows some asymmetry between the tool and striation, which is likely due to tool placement. This data indicates that there is inconsistency in the amount of contact between the tool and sheet, which induces the observed variations in surface finish.

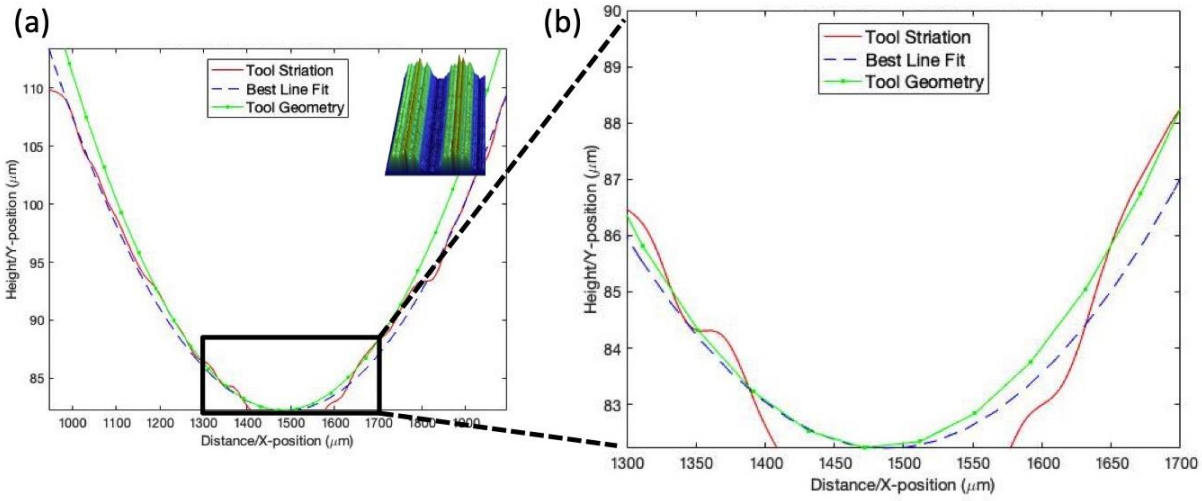

Figure 4.5 Superimposed tool geometry on the tool striation using the data analysis code described. Focusing at the striation valley shows where the tool is and is not in contact with the striation. TPIF, Heart Shape, AA 7075-O

4.5 Material Movement During Forming

Given the observed inconsistencies in the contact surface between the forming tool and sheet, understanding how material is moved during forming needed further investigation. To study this, a tribology "scratch test" detailed in Section 4.2.2 was performed. Results for the 4 mm tool at 100 N are given in Figure 4.6 and Figure 4.7. Each figure has a height map at the point of tool contact and the end of the scratch. Three line profiles, parallel and perpendicular to

the scratch, were measured. The perpendicular profiles allow for measurement of the scratch depth and indicate if the material is symmetrically displaced outside the scratch. It is known that the tool deflects at the macroscale, which is why programmed and effective squeeze factor are separately defined; this would further explore if deflection occurs at the microscale. Parallel line profiles show how the material is pushed during forming. The end of the scratch is analogous to the final tool pass of an incrementally formed part. Confirming this material movement supports the findings in Shin et al., which says that the macroscopic defects seen in the TPIF parts are due to material being pushed forward in a constrained geometry [24].

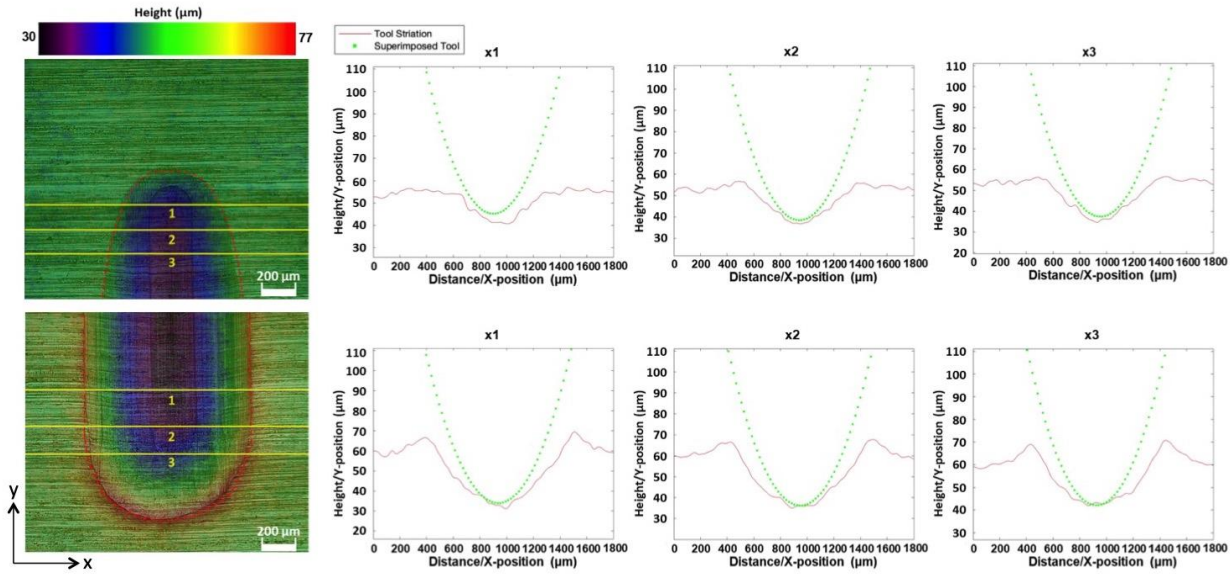

Figure 4.6 X-profile results from the scratch test at 100 N with the 4mm tool. Top row results are at the point of tool contact. Bottom row results are at the end of the scratch. Height maps are included for each location. The tool geometry is superimposed on the x line profiles. AA 7075-O

Figure 4.6 compares the x-profiles at the point of tool contact and the end of the scratch. The positions were selected to capture the progression of tool movement within the two areas of interest. Within the areas of interest, the striation depths were similar. The striations at the end of the scratch were 10-15 µm deeper than those at the beginning and material bulged symmetrically outside the striation.

Figure 4.7 compares the y-profiles at the point of tool contact and the end of the scratch. The positions were selected to observe any variations on either side of the center of the scratch. At the beginning of the scratch, there is a sudden drop in height when the tool contacts the material. At the end of the scratch, there is a distinct bulge where the material is pushed forward. Similar behavior is observed on either side of the scratch center.

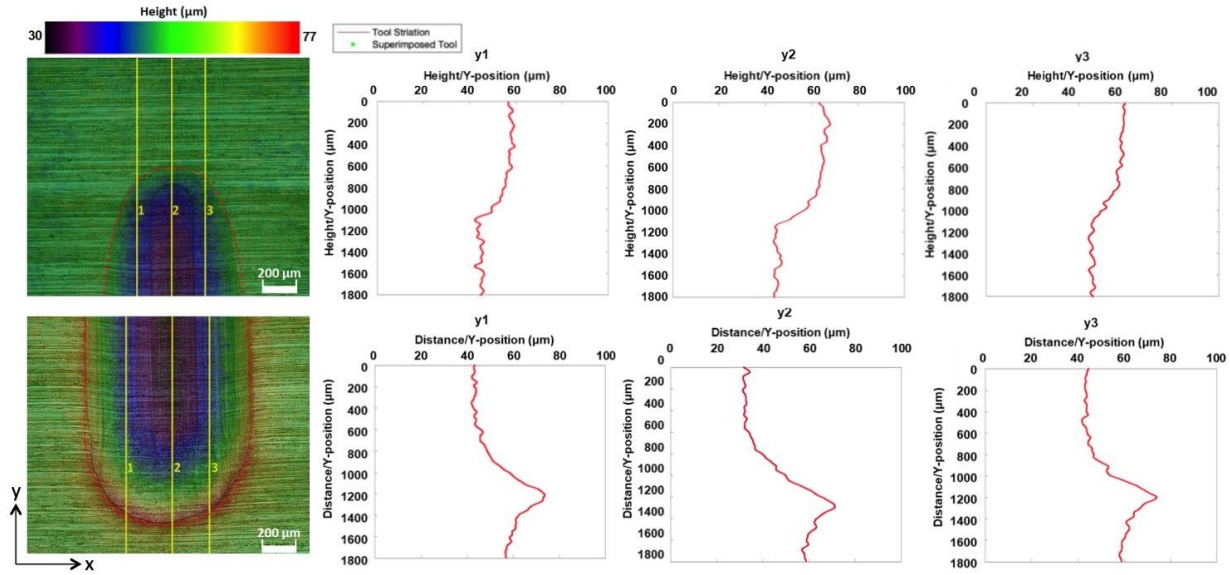

Figure 4.7 Y-profile results from the scratch test at 100 N with the 4mm tool. Top row results are at the point of tool contact. Bottom row results are at the end of the scratch. Height maps are included for each location. The tool geometry is superimposed on the y line profiles. AA 7075-O

The resulting height maps support the idea that the majority of the deformation occurs under the tool [21]. Additionally, the symmetric displacement of the material outside the scratch in the x-direction indicates limited tool deflection at the microscale. The material pushed forward in the y-direction forms a small bulge mirroring the shape of the scratch. When the part geometry is further constrained by a die, such as forming a TPIF heart-shaped part, this small bulge becomes a large macroscopic defect at the bottom of the final part in the undeformed material. The sine law indicates material thins at the walls, so for conservation of volume to hold true with a highly constrained geometry, the material pushed forward must stretch the

sheet into a concave bulge. A defect like this is undesirable for manufacturers; further work outside the scope of this thesis is currently being done by the University of Michigan ISF team to minimize its formation.

Chapter 5. Characterization Of Surface Features On Incrementally Formed Parts

5.1 Introduction

Surface characterization of incrementally formed parts is needed to understand how the parts will perform under cyclic fatigue loading. Extensive work has been done on measuring surface roughness and identifying good lubricants [20,34,66,71-81], but there is limited work characterizing the surface finish at the feature level. This analysis is critical, as any cracks or surface defects could be initiation sites for mechanical failure.

Chapter 4 of this dissertation work focused on the interactions between the forming tool and metal sheet; inconsistencies in the amount of contact between the tool and sheet were found, leading to variations in surface finish. This chapter continues exploring surface finish and further investigates the surface features that develop during forming at the microscale using SEM imaging. After analyzing several specimens across SPIF, TPIF and DSIF, the observed features were classified and their behavior was studied as a function of several process parameters. The native oxide layer and a brittle second phase were both significantly affected by the forming processes; the deformation and resulting crack depths were quantified using focused ion beam (FIB) analysis. These results were compared to high cycle fatigue testing to determine the effects on the bulk fatigue behavior.

5.2 Experimental Methods

SPIF and TPIF cones, SPIF variable angle funnels and TPIF heart-shaped components were formed at room temperature by Ankush Bansal and Erika Salem at the University of Michigan on a Standard Modern 1700 Series CNC lathe, FADAL 88HS and Cincinnati HMC 400 EP CNC milling machine. DSIF cones were formed at room temperature by Dohyun Leem and Newell Moser at Northwestern University on a custom-built DSIF machine. The process parameters used to form all the components are given in Table 5.1.

Table 5.1 Process parameters used to form all the ISF samples characterized in this study

Part Shape:	Cone	Funnel	Heart Shape
ISF Variant	SPIF, TPIF, DSIF	SPIF	TPIF
Material	AA 7075 - O	AA 7075 - O	AA 7075 - O
Thickness	1.58, 1.64 mm	1.64 mm	1.64 mm
Tool diameter	8, 12.7 mm	8 mm	8 mm
Forming angle	45°, 67°	15° - 70°	38°
Forming depth	35, 55 mm	55 mm	59 mm
Feed rate	25, 100 in/min	100 in/min	100 in/min
Step size	0.1, 0.2, 0.5 mm	0.5 mm	0.25, 0.5, 0.63 mm
Effective Squeeze Factor	0 – 5%	N/A	0 – 5%
Tool path	Spiral	Spiral	Contour
Lubricant	MoS_2 grease	MoS_2 grease	MoS_2 grease

An overview of all the part geometries are shown in Figure 5.1: (a) 67° cone; (b) 45° cone; (c) variable angle funnel from 15-70°; (d) heart-shaped component.

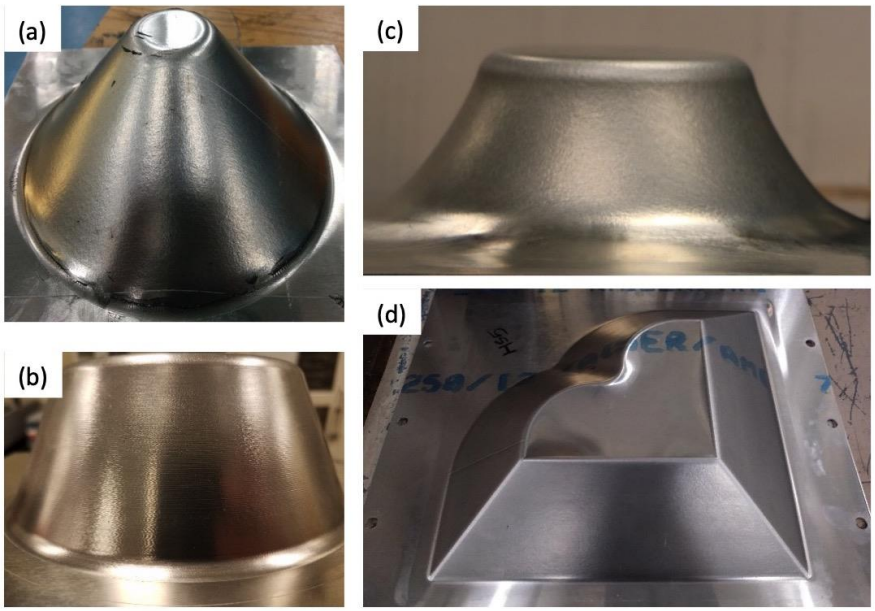

Figure 5.1 An overview of the incrementally formed samples characterized for this study: (a) 67° cone; (b) 45° cone; (c) variable angle funnel; (d) heart-shaped component

Surface finish samples, 15 mm x 15 mm, were sectioned from the component walls. For the heart-shaped specimens, the samples were from the center of the flat walls. The samples were cleaned with ethanol in the ultrasonic cleaner. SEM imaging was done on a Tescan Mira3 FEG SEM at an accelerating voltage of 10 kV, beam intensity of 11 and working distance of 10 mm. Data was taken on both sides of the formed component.

5.3 Surface Feature Classification

After analyzing all the images from the incrementally formed parts, the surface features can be classified into three types (Figure 5.2). On the tool side, the features are tribology grooves, formed at the interface between the tool and sheet (Figure 5.2a). Groove density and orientation are affected by wall angle and squeeze factor. On the non-tool side, the features are either transverse or longitudinal (Figure 5.2b,c). They are likely the result of mechanical deformation and appear as cracks on the surface. They are affected more by wall angle than squeeze factor. Wall angle and squeeze factor are discussed further in sections 5.4.2 and 5.4.3.

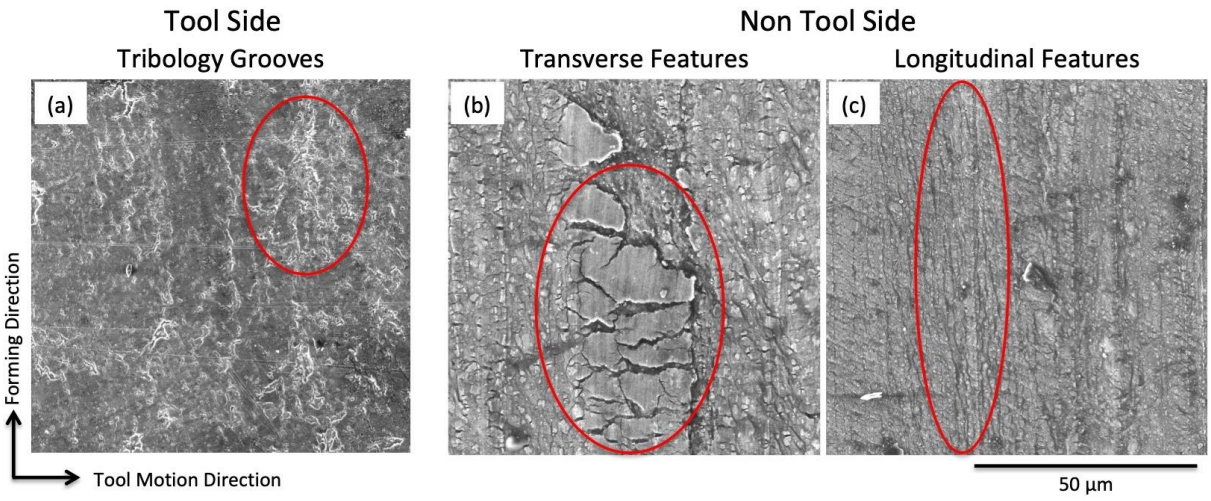

Figure 5.2 Three types of features found in incrementally formed parts. (a) Tribology grooves are found on the tool side. (b) Transverse and (c) longitudinal features are found on the non-tool side.

Quantifying the depths of the cracked transverse and longitudinal features was necessary to determine if those locations would serve as failure initiation sites under fatigue loading. The crack depths were too small for the resolution of the optical profilometer, so Focused Ion Beam (FIB) analysis was performed. The FIB analysis was done by Bobby Kerns, at the Michigan Center for Materials Characterization, on a Nova Nanolab 200 with electron beam conditions of 5kV, 400pA, and ion beam conditions of 30 kV at various currents. A protective carbon layer was deposited to avoid damaging the top surface when cutting cross sections with the ion beam.

Figure 5.3 details the FIB results on the non-tool side of a TPIF heart shaped specimen. A region of interest was chosen with uniformly dispersed cracking (Figure 5.3a) and a 30µm x 2µm x 1µm cross section was cut (Figure 5.3b). Energy dispersive spectroscopy (EDS) analysis indicated the features were the native oxide layer cracking. Most of the cracks were less than 200 nm in depth; the maximum depth was 628 nm (Figure 5.3c,d). This cracked oxide layer is similar to the surface seen by Zhang et al. in their study of micro crack formation during cold rolling of aluminum [43]. The surface oxide layer cracked and the aluminum matrix extruded through the openings, forming a layer of oxide fragments and metal surfaces.

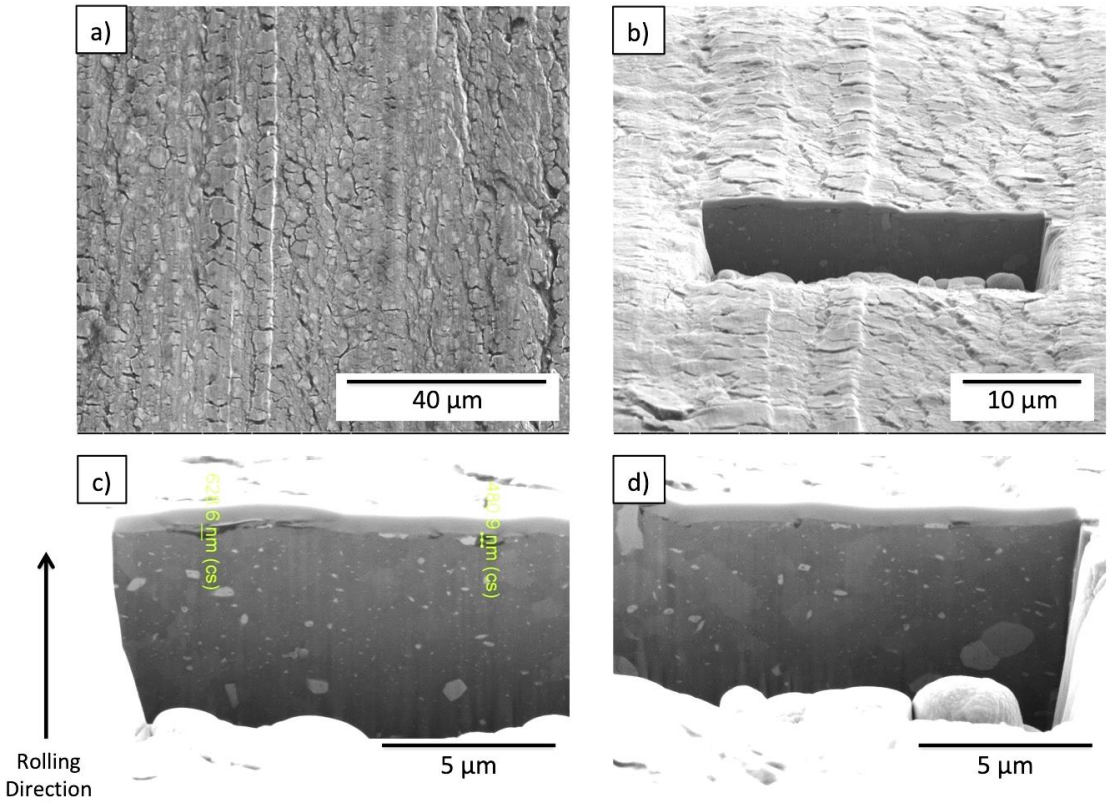

Figure 5.3 FIB analysis of the non-tool side features. (a) SEM region of interest; (b) Cross section with a protective carbon layer to avoid damaging the top surface when cutting with the ion beam; (c) Left edge of the cross section with depth measurements; (d) Right edge of the cross section. TPIF, Heart-shaped, eSF = 0%, AA 7075-O

5.4 Surface Feature Characterization

During the feature analysis, the effects of several process parameters were studied. Section 5.4.1 compares the surface features between TPIF and DSIF using single angle cones. Section 5.4.2 studies the effect of wall angle using a variable angle funnel and Section 5.4.3 studies the effect of squeeze factor on the TPIF heart-shaped parts.

5.4.1 TPIF vs. DSIF Comparison

The surfaces of 45° cones formed by TPIF and DSIF were compared and the results are shown in Figure 5.4. The tool side of the TPIF cone corresponds to the top side of the DSIF cone; both are in contact with the forming tool. The die side of the TPIF cone corresponds to the bottom side of the DSIF cone; both are in contact with a supporting surface.

The tool side of the TPIF cone (Figure 5.4a) exhibited a ‘cleaner’ surface than the top side of the DSIF cone (Figure 5.4c) – smaller tribology grooves, uniformly distributed throughout the surface. This is likely due to the amount of contact between the backside of the sheet and the supporting surface, affecting the stability of the mechanical support. In TPIF, the supporting surface is a full die and in DSIF, the supporting surface is the secondary tool, which is much smaller in size than the die. The larger surface area provides a more stable surface for the forming to occur. The die side of the TPIF cone (Figure 5.4b) exhibited a similar surface to the DSIF cone (Figure 5.4d).

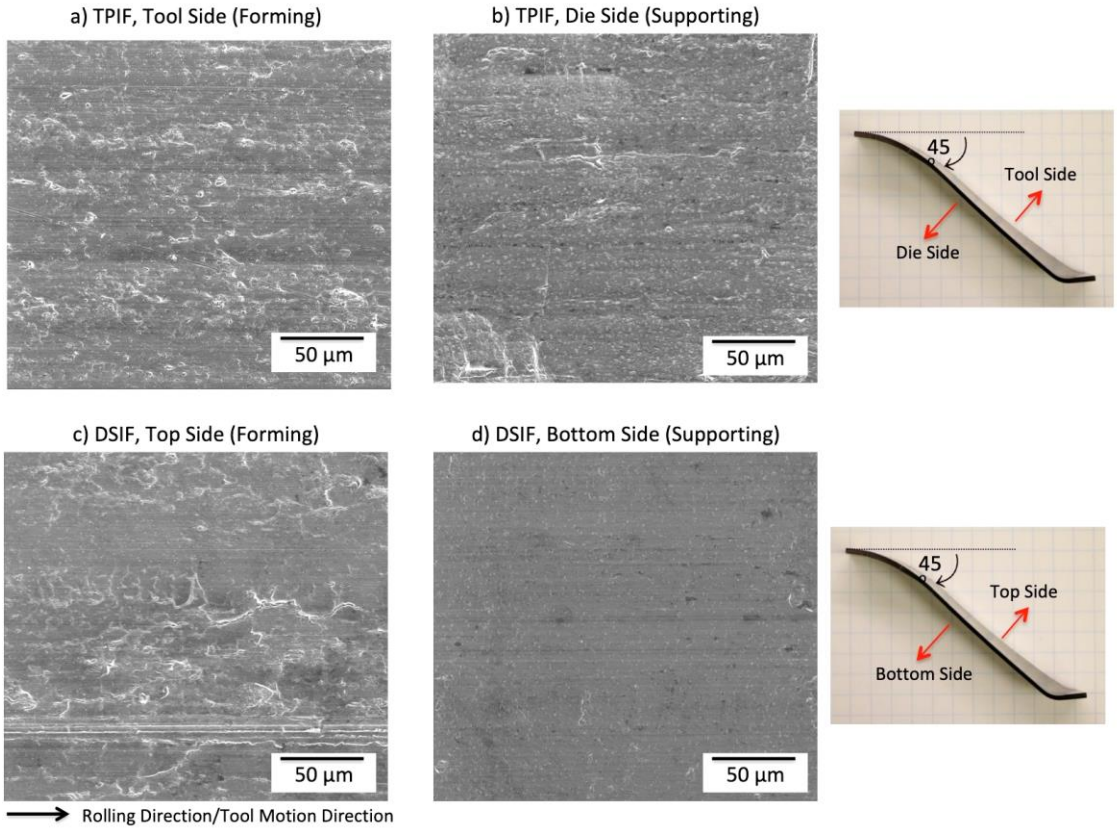

Figure 5.4 Surface feature comparison between 45° TPIF and DSIF cones: (a) TPIF tool side; (b) TPIF die side; (c) DSIF top side; (d) DSIF bottom side. The tool side of the TPIF cone corresponds to the top side of the DSIF cone; both are in contact with the forming tool. The die side of the TPIF cone corresponds to the bottom side of the DSIF cone; both are in contact with a supporting surface – a full die in TPIF and supporting tool in DSIF. AA 7075-O, 45°, Δz = 0.2mm

5.4.2 Effect of Wall Angle

The effect of increasing wall angle was studied using a SPIF variable funnel from 15-70°. Three angles were chosen as regions of interest to compare the progression of feature density and orientation on the tool and non-tool sides (Figure 5.5). With increasing angle, the feature density of the tribology grooves on the tool side increased and their orientation aligned with the forming direction (Figure 5.5a-c). On the non-tool side (Figure 5.5d-f), the oxide layer consistently cracked along the forming direction and there did not appear to be a noticeable difference in feature density.

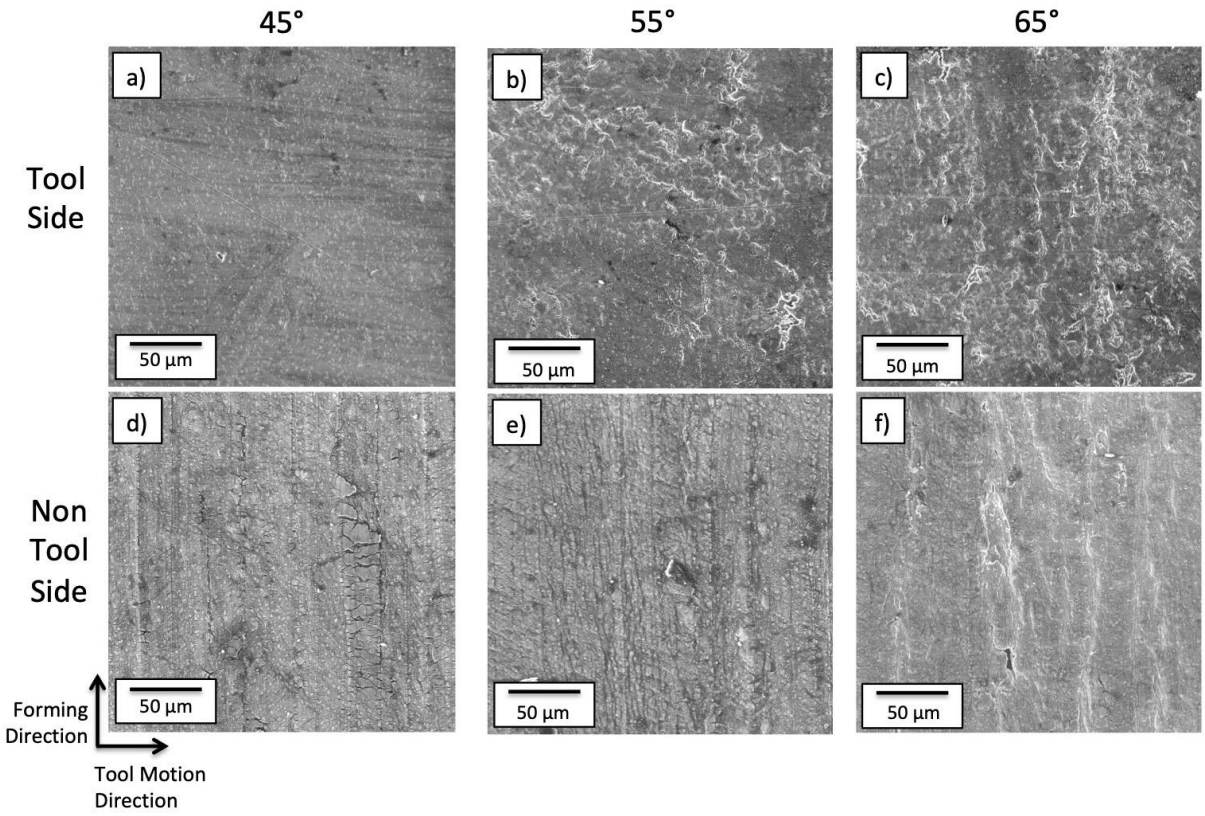

Figure 5.5 Surface feature comparison with increasing wall angle. The tool side and non-tool side were analyzed at (a,d) 45°, (b,e) 55° and (c,f) 65°. SPIF, Funnel, Δz = 0.5mm, AA 7075-O

To further understand the evolution of these features, predicted principal strains for an element at each angle on the non-tool side of the sheet were plotted from Jaekwang Shin's ISF

FEM analysis (Figure 5.6). The maximum principal strain is in the direction of elongation; the minimum principal strain is in the direction of thinning; the middle principal strain is in the circumferential direction. With increasing angle, the maximum principal strains increased by a factor of 2, minimum principal strains decreased by a factor of 2 and middle principal strains remained constant. It is noted that a change in strain by a factor of 2 did not manifest itself as a change in oxide cracking density on the non-tool side as the wall angle increased from 45°- 65°.

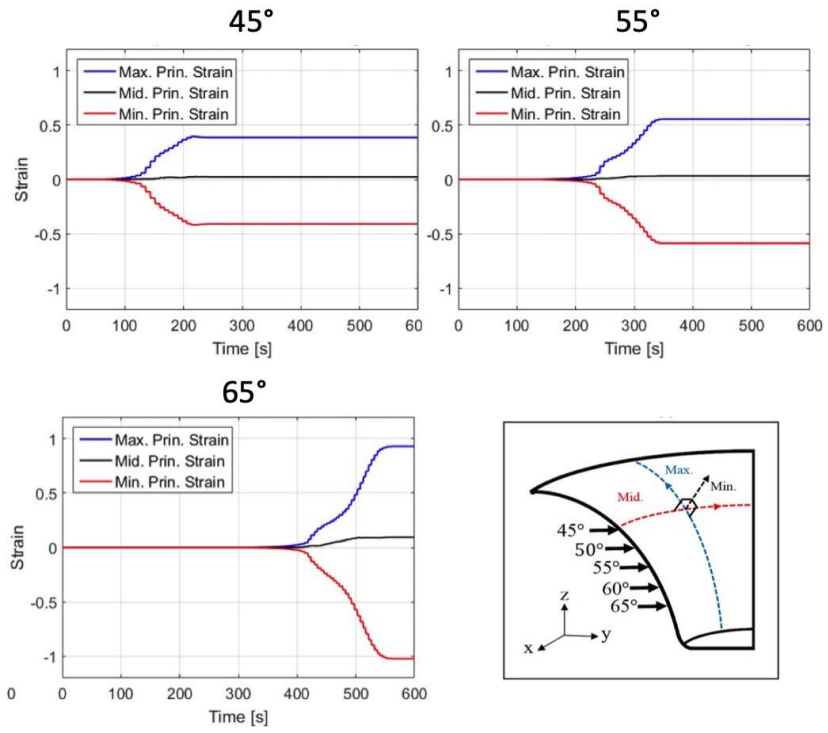

Figure 5.6 Predicted principal strains from the ISF FEM analysis of a variable angle funnel at 45°, 55° and 65°. SPIF, Δz = 0.5 mm, AA 7075-O

5.4.3 Effect of Squeeze Factor

The effect of squeeze factor was studied using TPIF heart-shaped components at two different flat walls. One wall is oriented with the rolling direction (RD) of the original material perpendicular to the direction of tool motion and the other is oriented with the transverse direction (TD) perpendicular to the direction of tool motion. Samples formed with 0-5%

effective squeeze factor were chosen for the analysis. Tool side results are shown in Figure 5.7 and non-tool side results are shown in Figure 5.8.

Increased squeeze factor led to a slight increase in the density of tribology grooves on the tool side. However, the more noticeable observation was the morphology difference between grooves on the differently oriented walls. The tribology grooves on the wall where the RD and tool direction are perpendicular (Figure 5.7a) were generally aligned with the direction of tool motion, but also consistently had transverse branches aligned with the RD. The tribology grooves on the wall where the TD and tool direction are perpendicular (Figure 5.7b) were fully aligned with the direction of tool motion, which is parallel to the RD. This indicates that the orientation of the tribology grooves was dependent on the RD of the original material.

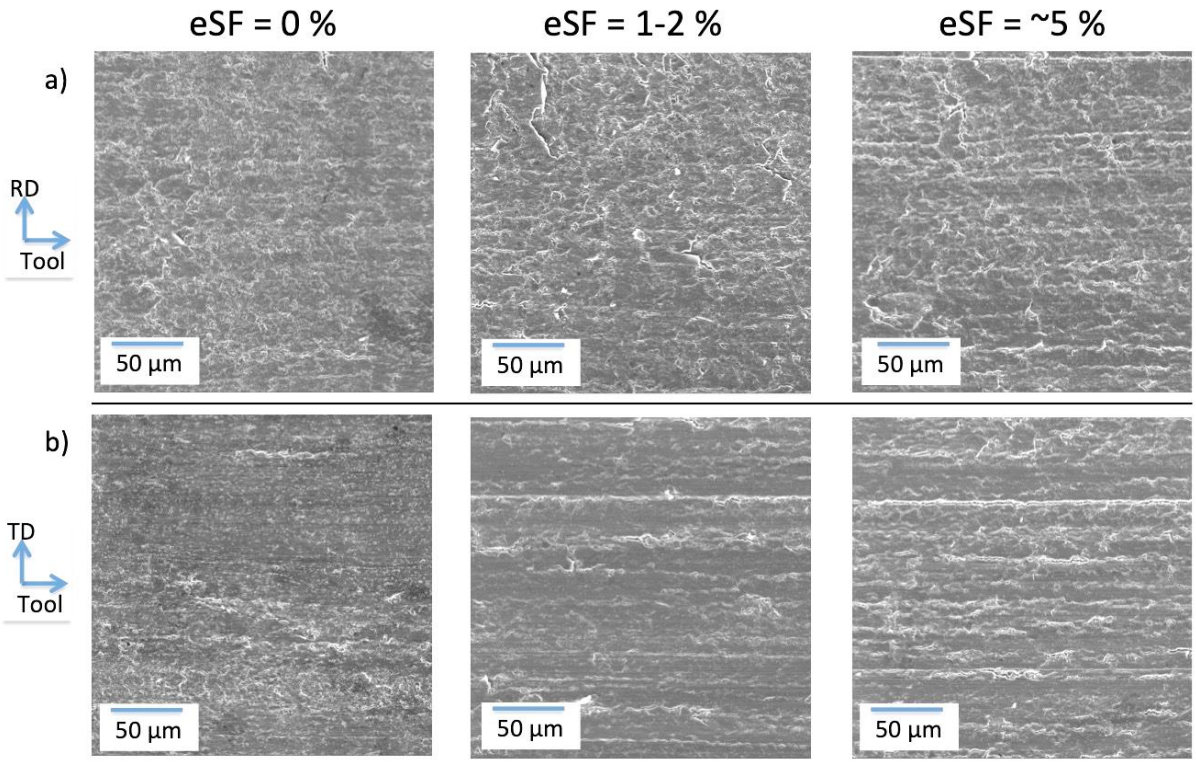

Figure 5.7 Surface feature comparison with increasing squeeze factor on the tool side at the flat wall where (a) the rolling direction is perpendicular to the direction of tool motion and (b) the transverse direction is perpendicular to the direction of tool motion. RD = rolling direction, TD = transverse direction. TPIF, Heart shape, Δz = 0.63mm, AA 7075-O

In contrast, increase squeeze factor did not have a significant effect on feature density or morphology on the non-tool side (Figure 5.8). Higher resolution images of the higher squeezed samples indicated the second phase is cracking, which is further investigated in the next section.

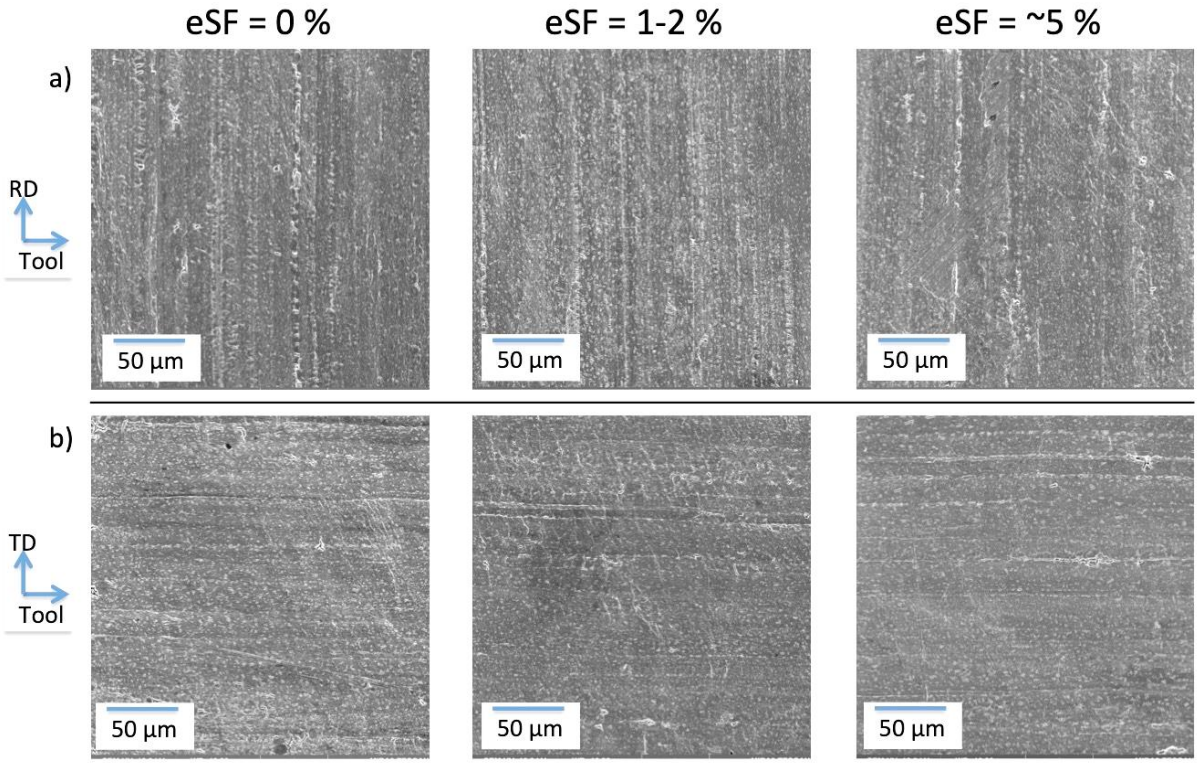

Figure 5.8 Surface feature comparison with increasing squeeze factor on the non-tool side at the flat wall where (a) the rolling direction is perpendicular to the direction of tool motion and (b) the transverse direction is perpendicular to the direction of tool motion. RD = rolling direction, TD = transverse direction. TPIF, Heart shape, Δz = 0.63mm, AA 7075-O

5.5 Second Phase Cracking

Three types of cracking were observed in the incrementally formed samples: matrix cracks; chain-like cracks along the second phase particles; cracks through the second phase particles (Figure 5.9). The second phase particles are 1-5µm in size and preliminary EDS analysis indicated they were Al-Mg-Zn-Cu. Particles of this size are generally considered brittle dispersoids in aluminum alloys and are known to crack under processing and machining conditions [38].

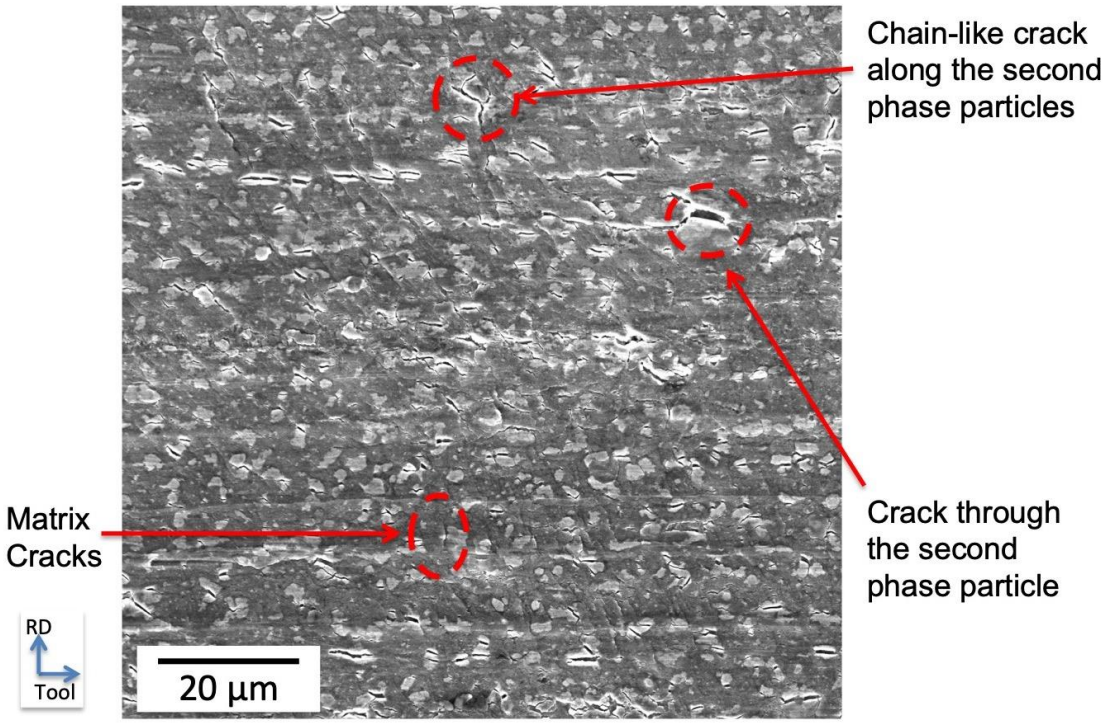

Figure 5.9 Three types of cracking observed in ISF samples: matrix cracks; cracks along the second phase particles; cracks through the second phase particles. TPIF, Heart shape, Δz = 0.63mm, AA 7075-O

Similar to the oxide layer analysis, quantifying the crack depth was necessary to determine if those locations would serve as failure initiation sites under fatigue loading. The crack depths were too small for the resolution of the optical profilometer, so FIB analysis was needed again. Bobby Kerns performed the FIB analysis on the Nova Nanolab 200 at the same conditions as the previous study. A protective platinum cap was deposited on the crack location to avoid further opening when cutting a cross section with the ion beam.

Figure 5.10 details the FIB results on the cracked second phase on the non-tool side of a TPIF heart shaped specimen. A region of interest was chosen (Figure 5.10a) and a 3µm x 2µm cross section was cut (Figure 5.10b,c). Energy dispersive spectroscopy (EDS) analysis confirmed the second phase was Al-Mg-Zn, but also picked up an O peak indicating the phase

may be in the native oxide layer at the surface. The crack extended through the particle, approximately 400 nm in size, and is blunted by the matrix (Figure 5.10d).

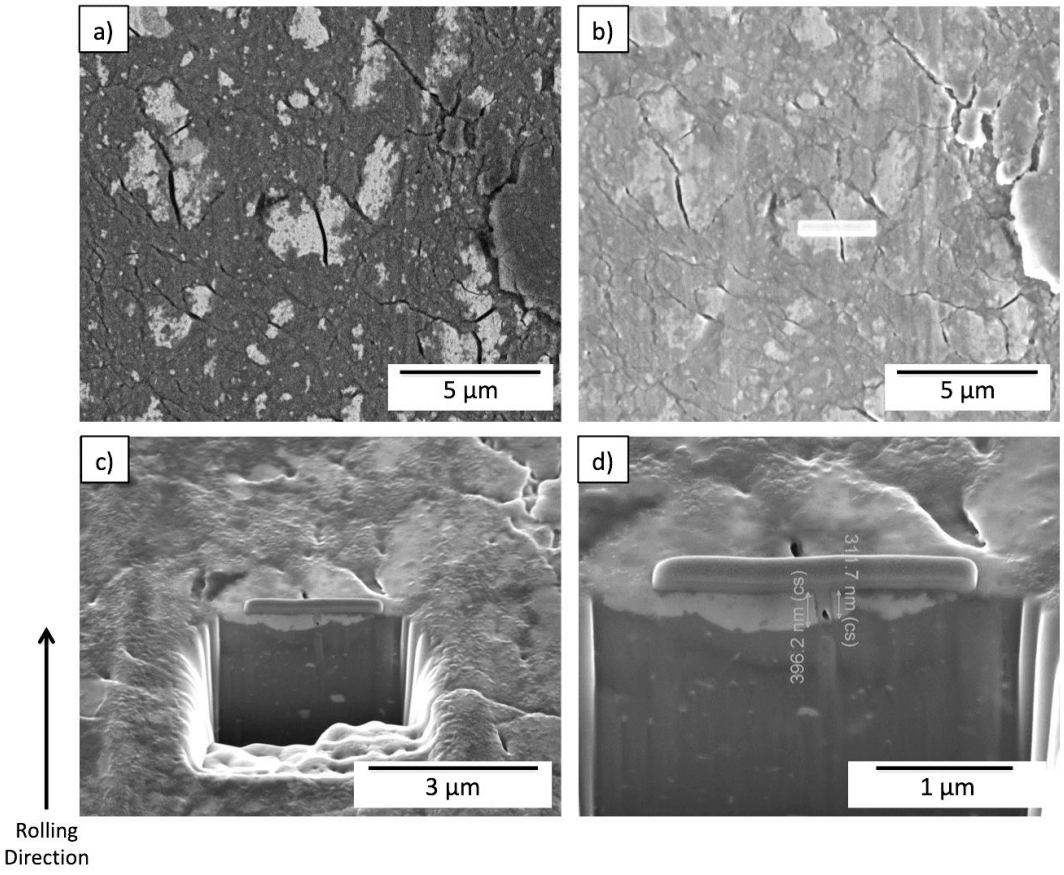

Figure 5.10 FIB analysis of the cracking second phase. (a) SEM region of interest; (b) Cross section with a protective platinum cap over the crack to avoid further opening when cutting a cross section; (c) Cross section; (d) Higher resolution of cross section with depth measurements. TPIF, Heart-shaped, eSF = 2%, AA 7075-O

Figure 5.11 shows the progression in second phase cracking with increasing squeeze factor and the associated radial forces. At eSF = 0% at 405 N (Figure 5.11a), the second phase was uniformly dispersed but barely cracking. The amount of cracks greatly increased when eSF = 2% at 431 N (Figure 5.11b) and continued when eSF = 5% at 526 N (Figure 5.11c). It appears that there is a threshold force for the cracking to occur and further work outside the scope of this thesis should continue this study.

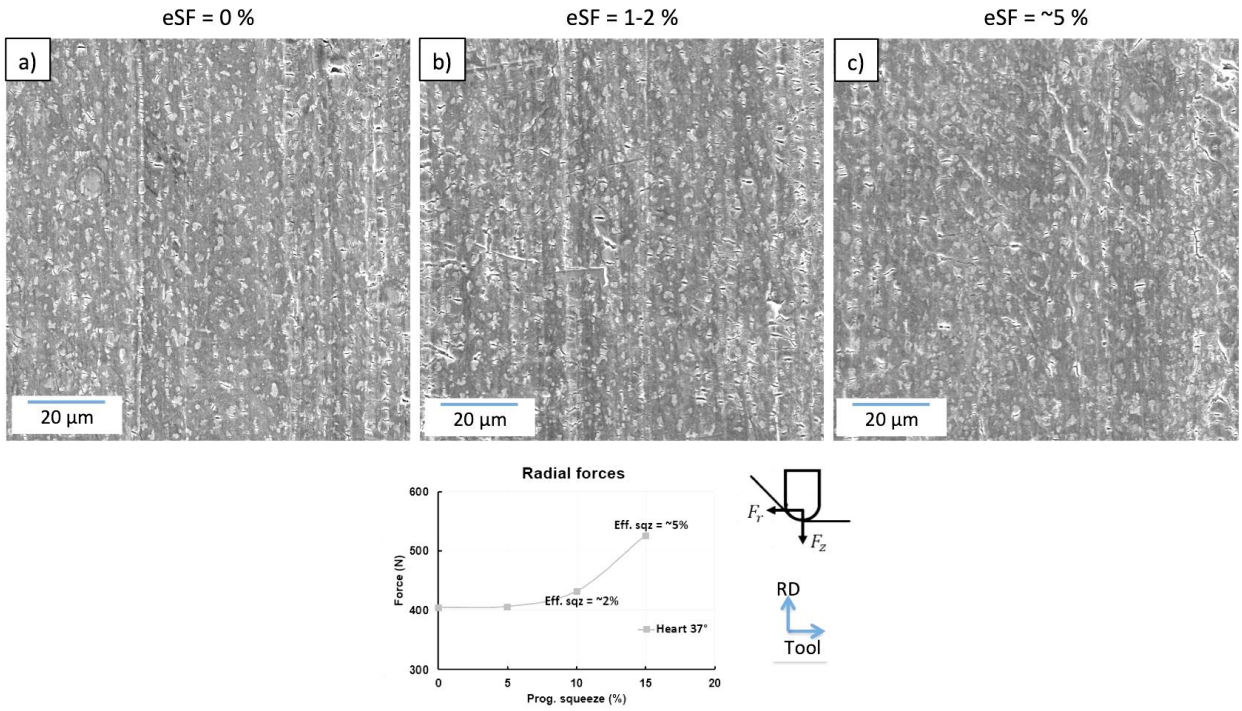

Figure 5.11 Progression in second phase cracking with increasing squeeze factor. (a) eSF = 0%, (b) eSF = 2%, (c) eSF = 5%. Radial forces at the respective effective squeeze factors included. TPIF, Heart-shaped, AA 7075-O

5.6 Effect on Fatigue Properties

The objective of the surface characterization was to determine the effects on the bulk fatigue properties and determine if any cracks or surface defects could be sites of failure initiation. It is unlikely cracks in the oxide layer would be fatigue crack initiation sites; the second phase cracking is more likely to be them. The cracks are limited to the second phase and are blunted at the matrix, but might serve as areas of high stress concentration. Fatigue testing of the TPIF heart-shaped specimens was done by Boeing and compared to a hydroformed part with the same geometry. The results are proprietary, but the ISF fatigue properties were similar to the hydroformed specimens, with the caveat that only limited fatigue tests were performed. Unfortunately, Boeing was not able to get us the failed specimens in time for this dissertation work to determine if the fatigue cracks initiated at the surface. To fully understand the effects of this cracking on the fatigue properties, this comparison should be done.

Chapter 6. Conclusions And Future Work

Incremental sheet forming (ISF) is a die-less or low-cost die manufacturing process where components are formed from metal sheet through a series of localized plastic deformations. It is of high interest for prototyping, after-market service and creating complex products with high strength at low costs in the automotive and aerospace industries. For ISF to be widely used, current challenges predicting the microstructure and mechanical properties of the as-formed parts must be addressed, as well as concerns about tribological and mechanically induced surface features that may impact fatigue life.

This dissertation work addressed two key research objectives for optimizing the performance of incrementally formed AA 7075:

1. Characterizing the microstructural evolution under various strain paths and locally applied force to determine if the microstructure of the formed part can be predicted
   - An improved sample preparation technique for EBSD analysis was developed for characterizing ISF parts. This technique allowed for a majority of the grain structure to be resolved, even at areas with 70+% strain.
   - EBSD analysis showed the grains elongating proportionally to the stretch of the sheet. Further characterization should be done with higher resolution techniques.
   - Strain history appeared to affect microstructure and texture. Further work comparing ISF and deep drawing, as two different strain paths forming the equivalent final geometry, should be performed to fully understand this phenomenon.

- There was no indication of recrystallization in the formed parts, indicating that the starting grain structure can be used to predict the microstructure evolution due to a known strain path and ICME tools can be used for predicting texture. Further research should be conducted to strengthen the prediction models.

2. Studying the surface of as-formed components to understand its potential impact on fatigue properties

- Inconsistencies in tool contact induced variations in surface finish on the as-formed components, even within a single tool striation.
- The majority of the deformation occurred under the tool with limited deflection at the microscale. Material pushed forward formed a macroscopic bulge after the final tool pass.
- Tribological grooves formed on the tool side surface:
    - Grooves were smaller and more uniformly distributed in TPIF than DSIF
    - Groove density increased with increasing wall angle and effective squeeze
    - Groove orientation was dependent on the rolling direction of the original material
- The native oxide layer cracked on the non-tool side surface at a maximum depth of ~620 nm. Their morphology indicates these cracks are unlikely to be sites of fatigue crack initiation.
- Second phase particles (Al-Mg-Zn) cracked on the non-tool side surface at a maximum depth of ~300 nm. Cracks were blunted by the matrix, but might serve as areas of high stress concentration, leading to potential sites for fatigue crack growth.
    - There appears to be a threshold radial force where the second phase particles begin to crack, preliminary examined with effective squeeze factor. Further work should also be done to quantify this force.

- Fatigue testing of ISF parts gave similar results to hydroformed parts, but the samples could not be released from the company in time for this dissertation work to characterize the fracture surfaces. Further work must be done to determine if fatigue cracking initiated at the surface.

Appendices

Appendix A.

Characterizing the Microstructure Evolution as a Function of Effective Squeeze Factor

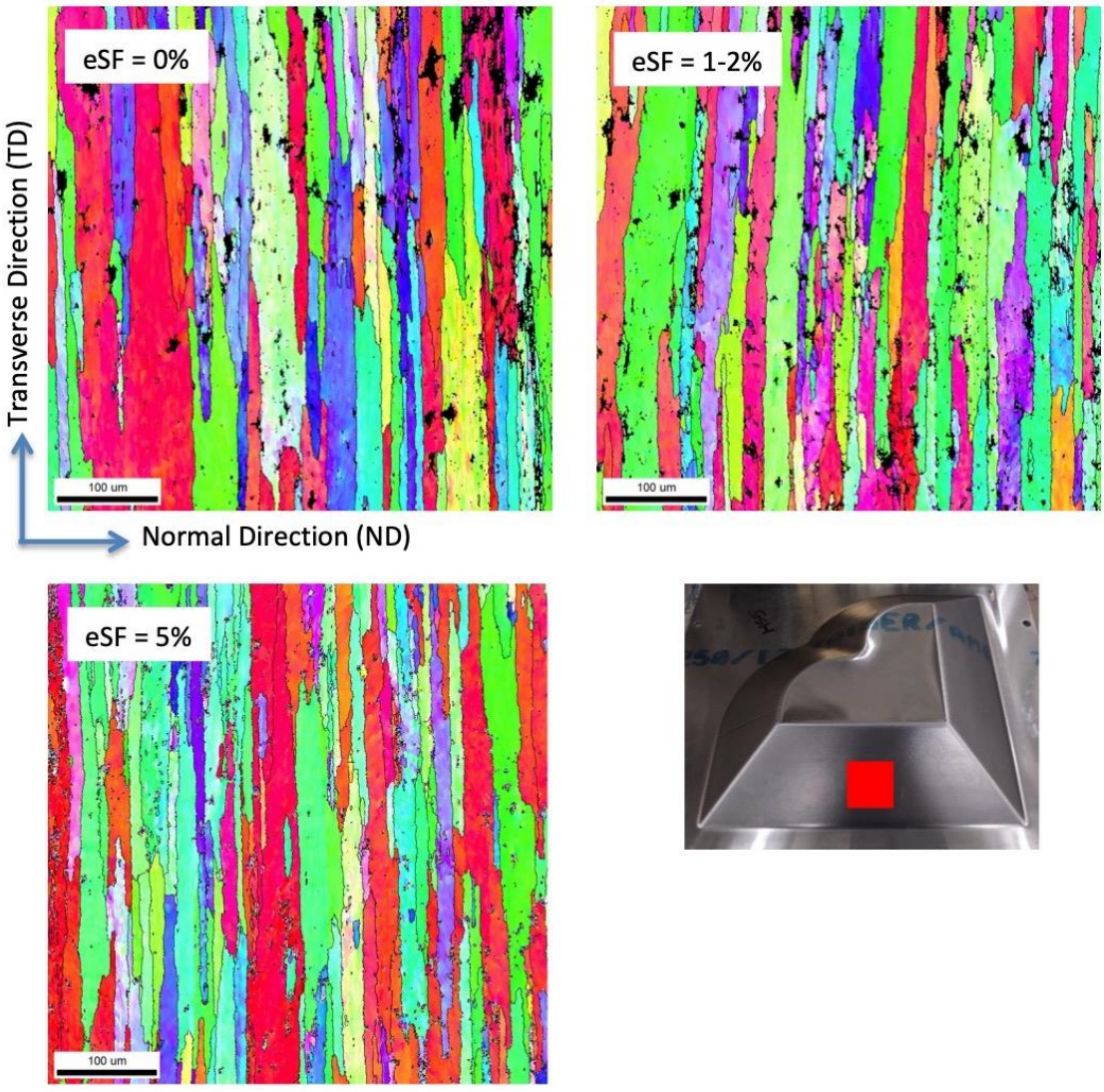

Figure A-1 Microstructural evolution with increasing effective squeeze factor on the TPIF heart shaped specimens. Direction of tool motion is parallel to the transverse direction. No significant change in grain size observed. AA 7075-O, 38°, EBSD step size = 0.4 µm

Appendix B.

Experimental EBSD Results of Undeformed Material Used in CP-FEM RVE

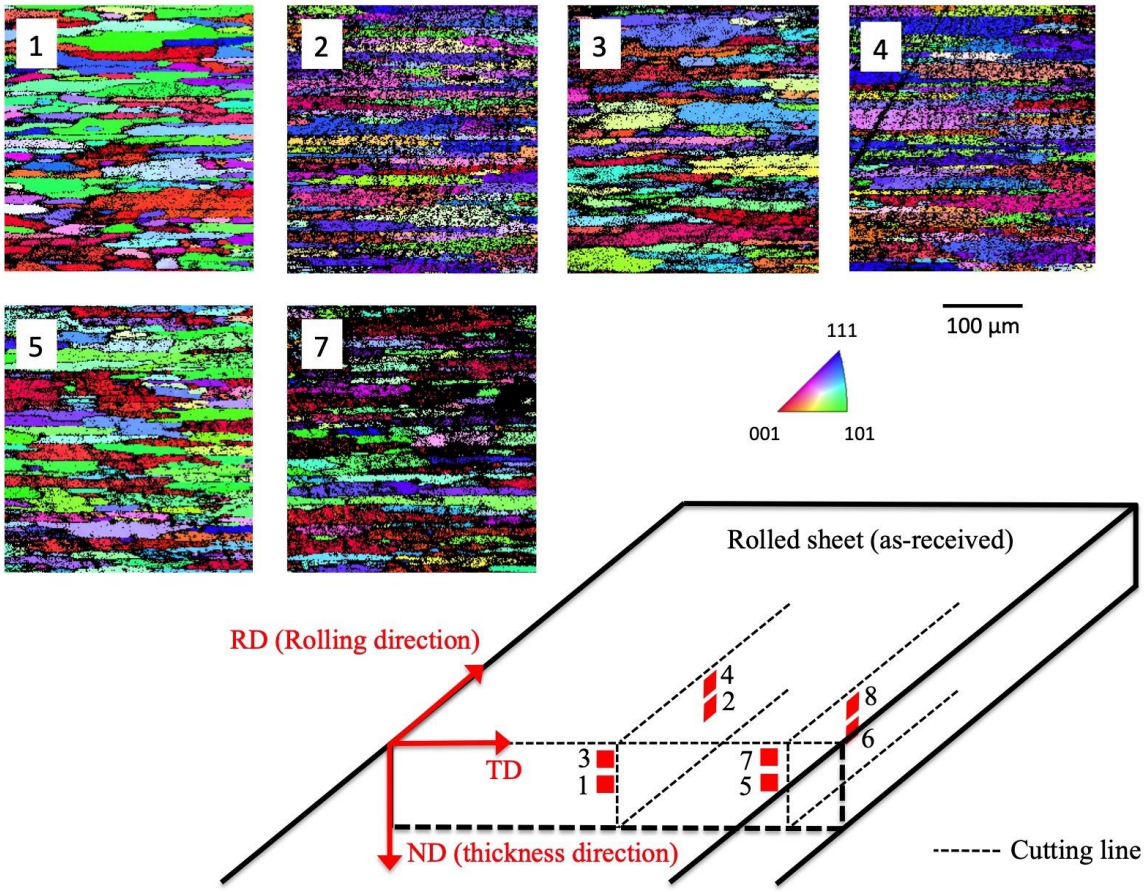

Figure B-1 Experimental EBSD results of the virgin AA 7075-O material at various cross sections used for building the CP-FEM RVE. Locations 6/8 were not reported, because the microstructure was found to be consistent from locations 1-5,7. EBSD step size = 2 µm

Appendix C.

Characterizing the Effects of Tool Speed and Step Size on Surface Roughness

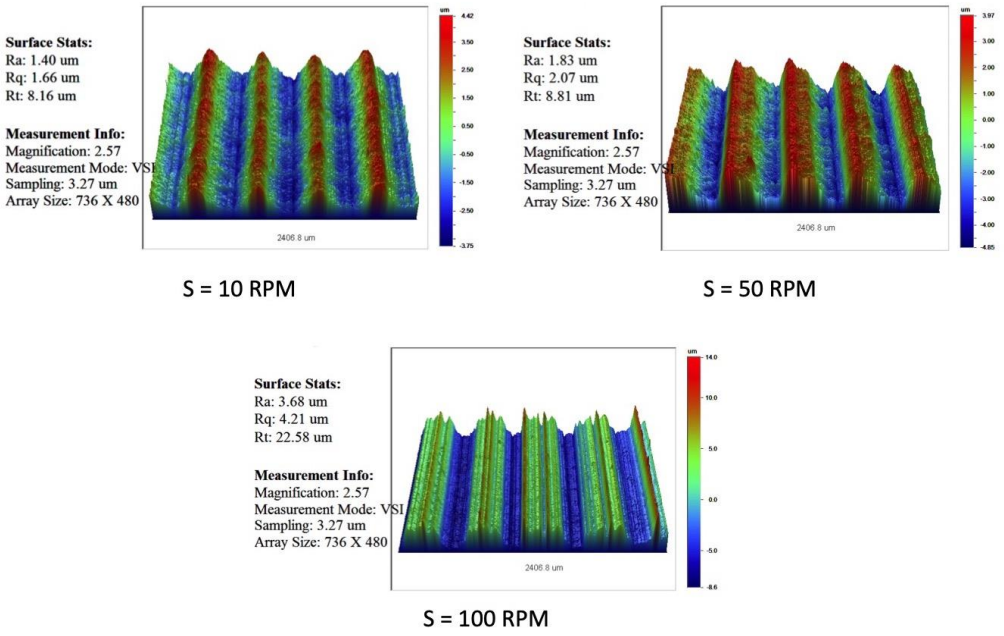

Figure C-1 Surface roughness increases with increasing tool speed. AA 7075-O, Δz = 0.5mm

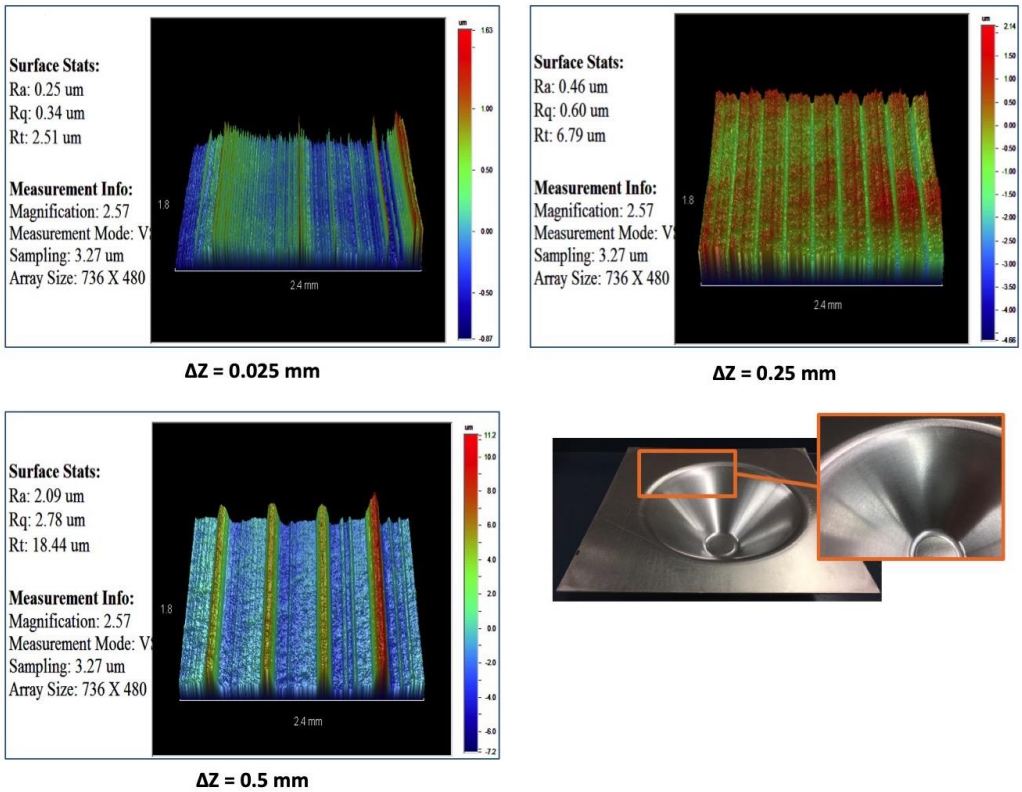

Figure C-2 Surface roughness increases with increasing step size. AA 7075-O, S = 50RPM

References

[1] Taub, A. I. *et al*., "Yesterday, Today and Tomorrow: The Evolution of Technology for Materials Processing over the Last 50 Years: The Automotive Example," *JOM*, 48-57 (2007). https://doi.org/10.1007/s11837-007-0022-7

[2] "Lightweight Materials For Cars and Trucks." Vehicle Techologies Office, Office of Energy Efficiency & Renewable Energy. Available: https://www.energy.gov/eere/vehicles/lightweight-materials-cars-and-trucks

[3] Reddy, N. V., Lingam, R. & Cao, J. in *Handbook of Manufacturing Engineering and Technology*, 411–452 (2015). doi:10.1007/978-1-4471-4670-4

[4] Nimbalkar, D. H. & Nandedkar, V. M. Review of Incremental Forming of Sheet Metal Components. *Int. J. Eng. Res. Appl.* **3,** 39–51 (2013).

[5] Silva, M. B., Bay, N. & Martins, P. A. F. in *Sustainable Manufacturing* (ed. Davim, J. P.) (2010).

[6] Adams, D. & Jeswiet, J. Design rules and applications of single-point incremental forming. *Proc. Inst. Mech. Eng. Part B J. Eng. Manuf.* **229,** 754–760 (2014).

[7] Allwood, J. M., Houghton, N. E. & Jackson, K. P. The Design of an Incremental Sheet Forming Machine. *Adv. Mater. Res.* **6-8,** 471–478 (2005).

[8] Tanaka, S., Nakamura, T., Hayakawa, K., Nakamura, H. & Motomura, K. Residual stress in sheet metal parts made by incremental forming process. *AIP Conf. Proc.* **908,** 775–780 (2007).

[9] Radu, C., Herghelegiu, E., Tampu, C. & Cristea, I. The Residual Stress State Generated by Single Point Incremental Forming of Aluminum Metal Sheets. *Appl. Mech. Mater.* **371,** 148–152 (2013).

[10] Radu, C., Tampu, C., Cristea, I. & Chirita, B. The Effect of Residual Stresses on the Accuracy of Parts Processed by SPIF. *Mater. Manuf. Process.* **28,** 572–576 (2013).

[11] Radu, C., Cristea, I., Herghelegiu, E. & Tabacu, S. Improving the Accuracy of Parts Manufactured by Single Point Incremental Forming. *Appl. Mech. Mater.* **332,** 443–448 (2013).

[12] Jeswiet, J. *et al.* Metal forming progress since 2000. *CIRP J. Manuf. Sci. Technol.* **1,** 2–17 (2008).

[13] Ghaei, A. Modeling springback in stamped automotive structures. *ProQuest Diss. Theses* 207 (2010).

[14] Li, K. P., Carden, W. P. & Wagoner, R. H. Simulation of springback. *Int. J. Mech. Sci.* **44,** 103–122 (2002).

[15] Wagoner, R. H. & Li, M. Simulation of springback: Through-thickness integration. *Int. J. Plast.* **23,** 345–360 (2007).

[16] Lee, S. W. & Yang, D. Y. An assessment of numerical parameters influencing springback in explicit finite element analysis of sheet metal forming process. *J. Mater. Process. Technol.* **80,** 60–67 (1998).

[17] Lee, M.-G., Kim, D., Wagoner, R. H. & Chung, K. Semi-analytic hybrid method to predict springback in the 2D draw bend test. *J. Appl. Mech.* **74,** 1264 (2007).

[18] Jewiet, J., *et al*. Asymmetric Single Point Incremental Forming of Sheet Metal. *CIRP Annals*, **54**, 2, 88-114 (2005).

[19] Ambrogio, G., *et al*. Surface and Microstructure Considerations in High Speed Single Point Incremental Forming of Ti6Al4V Sheets. *Key Engineering Materials*, **611-612** (2014).

[20] Radu, C., *et al*. Anaylsis of the Surface Quality of Parts Processed by Single Poit Incremetal Forming. *J. Eng. Stds. Res*. **19** (2013).

[21] Salem, E., J. Shin, M. Nath, M. Banu and A. Taub. Investigation of Thickness Variation in Single Point Incremental Forming. 44th North American Manufacturing Research Conference. *Procedia Manufacturing* (2016).

[22] Nath, M., E. Salem, J. Shin, T. Odykirk, M. Banu and A. Taub. "Microstructure and Surface Finish Evolution During Single Point Incremental Forming," *In Contributed Papers from Materials Science & Technology 2017* (2017).

[23] Nath, M., J. Shin, A. Bansal, M. Banu and A. Taub. Comparison of Texture and Surface Finish Evolution During Single Point Incremental Forming and Formability Testing of AA 7075. In: *Light Metals 2018*, The Minerals, Metals & Materials Series (2018).

[24] Shin, J., A. Bansal, M. Nath, R. Cheng, M. Banu and A. Taub. Prediction of Negative Bulge in Two Point Incremental Forming (TPIF) of an Asymmetric Heart Shape Part. NUMISHEET 2018, *J. Phys. Conf. Ser.* (2018).

[25] Silva, M. B. *et al.*, Single-point incremental forming and formability – failure diagrams. *Journal of Strain Analysis for Engineering Design*, 43, 15-35 (2008).

[26] Eyckens, P. *et al*. Strain evolution in the single point incremental forming process: Digital image correlation measurement and finite element prediction. *International Journal of Material Forming*, 4, 1, 55-71 (2010).

[27] Jackson, K. & Allwood, J. The mechanics of incremental sheet forming. *J. Mater. Process. Technol.* **209,** 1158–1174 (2009).

[28] Malhotra, R., Xue, L., Belytschko, T. & Cao, J. Mechanics of fracture in single point incremental forming. *J. Mater. Process. Technol.* **212,** 1573–1590 (2012).

[29] Smith, J., Malhotra, R., Liu, W. K. & Cao, J. Deformation mechanics in single-point and accumulative double-sided incremental forming. *Int. J. Adv. Manuf. Technol.* **69,** 1185–1201 (2013).

[30] Seong, D. Y., Haque, M. Z., Kim, J. B., Stoughton, T. B. & Yoon, J. W. Suppression of necking in incremental sheet forming. *Int. J. Solids Struct.* **51,** 2840–2849 (2014).

[31] Bambach, M. A geometrical model of the kinematics of incremental sheet forming for the prediction of membrane strains and sheet thickness. *J. Mater. Process. Technol.* **210,** 1562–1573 (2010).

[32] Young, D., Jeswiet, J. Wall thickness variations in single-point incremental forming. *J. Eng. Manufact. Part B* 218, 1453–14590 (2004).

[33] Matsubara, S. A Computer Numerically Controlled Dieless Incremental Forming of a Sheet Metal. *Proceedings of the Institution of Mechanical Engineers, Part B: Journal of Engineering Manufacture*, vol. 215, no. 7, pp. 959–966 (2001).

[34] Bhattacharya, A., *et al*. Formability and Surface Finish Studies in Single Point Incremental Forming. *J. Mfg. Sci. Eng*. 133 (2011).

[35] Bansal, A., *et al*. Prediction of forming forces in single point incremental forming. *J. Mfg. Processes* (2017).

[36] Bansal, A., *et al*. Effects of machine kinetics on formability and part accuracy in two-point incremental forming. *In progress.*

[37] Shin, J., A. Bansal, M. Nath, R. Cheng, M. Banu and A. Taub. Prediction of Negative Bulge in Two Point Incremental Forming (TPIF) of an Asymmetric Heart Shape Part. NUMISHEET 2018, *J. Phys. Conf. Ser.* (2018).

[38] Davis, J.R. *Aluminum and Alumnium Alloys: ASM Handbook.* ASM International, (1993).

[39] *Properties and Selection: Nonferrous Alloys and Special-Purpose Materials, ASM Handbook* **2,** 62–122 (1992).

[40] Birbilis, N., *et al*. Electrochemical Characteristics of Intermetallic Phases in Aluminum Alloys. *J. Electrochem. Soc*. 152 (2005).

[41] Zou, Xiu-liang, *et al*. Evolution of second phases and mechanical properites of 7075 Al alloy processed by solution heat treatment. *Trans. Nonferros Met. Soc. China*, 27 (2017).

[42] Barter, S.A., et al. Typical Fatigue-Nucleating Discontinuities in Metallic Aircraft Structures. *Aircraft Sustainment and Repair*, (2018).

[43] Zhang, C., et al. Micro Crack of Aluminum Sheet During Cold Rolling. *World Journal of Mechanics*, 1, 169-175 (2011).

[44] Meyers, M. A. & Chawla, K. K. *Mechanical Behavior of Materials*. *Cambridge University Press* (2007).

[45] Kalpajian, Kalpakjian, S. & Schmid, S. R. *Manufacturing Processes for Engineering Materials*. *International Journal of Machine Tool Design and Research* **25,** (2003).

[46] Naderi, M., Ketabchi, M., Abbasi, M. & Bleck, W. Analysis of microstructure and mechanical properties of different high strength carbon steels after hot stamping. *J. Mater. Process. Technol.* **211,** 1117–1125 (2011).

[47] Fan, D. W., Kim, H. S., Birosca, S. & Cooman, B. C. De. Critical review of hot stamping technology for automotive steels. *Mater. Sci. Technol.* 99–110 (2007).

[48] Fan, X. B., He, Z. Bin, Zhou, W. X. & Yuan, S. J. Formability and strengthening mechanism of solution treated Al-Mg-Si alloy sheet under hot stamping conditions. *J. Mater. Process. Technol.* **228,** 179–185 (2016).

[49] Azushima, A. *et a*l. Frictio behavior of aluminum-coated 22MnB5 in hot stamping under dry and lubricated conditions. *J. Mat. Proc. Tech*, 212(5), 1014-1021 (2012).

[50] Ghiotti, A. *et al*. Wear onset in hot stamping of aluminum alloy sheets. *Wear*, 376-377. Part A, 485-495 (2017).

[51] Tikhovskiy, I., Raabe, D. & Roters, F. Simulation of earing during deep drawing of an Al-3% Mg alloy (AA 5754) using a texture component crystal plasticity FEM. *J. Mater. Process. Technol.* **183,** 169–175 (2007).

[52] WANG, Y. *et al.* Influence of blank holder type on drawability of 5182-O aluminum sheet at room temperature. *Trans. Nonferrous Met. Soc. China* **26,** 1251–1258 (2016).

[53] Savoie, J., Zhou, Y., Jonas, J. J. & Macewen, S. R. TEXTURES INDUCED BY TENSION AND DEEP DRAWING IN ALUMINUM SHEETS. *Acta Mater.* **44,** 587–605 (1996).

[54] Suwas, S. & Gurao, N. P. Crystallographic texture in materials. *J. Indian Inst. Sci.* **88,** 151–177 (2008).

[55] Martins, A.L., *et al*. Study of the deep drawing behavior and crystallographic texture of AA 3104-H19 aluminum alloy sheets. Proc. IMechE. Par L: J. Materials: Design and Applications, 230(3), 748-759 (2016).

[56] Simões, F. J. P., De Sousa, R. J. A., Grácio, J. J. A., Barlat, F. & Yoon, J. W. Mechanical behavior of an asymmetrically rolled and annealed 1050-O heet. *Int. J. Mech. Sci.* **50,** 1372–1380 (2008).

[57] Tamimi, S. *et al.* Asymmetric rolling of thin AA-5182 sheets: Modelling and experiments. *Mater. Sci. Eng. A* **603,** 150–159 (2014).

[58] Hurley, P. J. & Humphreys, F. J. The application of EBSD to the study of substructural development in a cold rolled single-phase aluminium alloy. *Acta Mater.* **51,** 1087–1102 (2003).

[59] Bobor, K. *et al.* Microstructure and mechanical properties of Al 7075 alloy processed by differential speed rolling. *Period. Polytech.* **2,** 111–115 (2012).

[60] Tajally, M. & Emadoddin, E. Mechanical and anisotropic behaviors of 7075 aluminum alloy sheets. *Mater. Des.* **32,** 1594–1599 (2011).

[61] Mo, Y. *et al.* Effects of Microstructure on the deformation behavior, mechanical properties and residual stress of cold-rolled HA177-2 aluminum brass tube. J. Mat. Proc. Tech. 235, 75-84 (2016).

[62] Chu, G., Li, F. & Liu, W. Deformation characteristics during Y-shaped tube hydroforming of 6061 aluminum alloy. *Jom* **63,** 81–84 (2011).

[63] Hwang, Yeong-Maw and Li-Shan Huang. Friction tests in tube hydroforming, *Proc. Of IIM, Part B: J. Eng. Manufacture* (2005).

[64] Ben Hmida, R., Thibaud, S., Gilbin, a. & Richard, F. Influence of the initial grain size in single point incremental forming process for thin sheets metal and microparts: Experimental investigations. *Mater. Des.* **45,** 155–165 (2013).

[65] Chezhian Babu, S. & Senthil Kumar, V. S. Experimental studies on incremental forming of stainless steel AISI 304 sheets. *Proc. Inst. Mech. Eng. Part B J. Eng. Manuf.* **226,** 1224–1229 (2012).

[66] Hamilton, K. & Jeswiet, J. Single point incremental forming at high feed rates and rotational speeds: Surface and structural consequences. *CIRP Ann. - Manuf. Technol.* **59,** 311–314 (2010).

[67] Chezhian Babu, S. & Senthil Kumar, V. S. Investigations on Incremental Forming of Low Carbon Steel Sheets. *Applied Mechanics and Materials.* **26-28,** 340–346 (2010).

[68] Barnwal, V.K., *et al*. Forming behavior and microstructural evolution during single point incremental forming process of AA-6061 aluminum alloy sheet. *Int. J. Adv. Manuf. Technol*. **95**:921-235 (2018).

[69] Shrivastava, Parnika and Puneet Tandon. Microstructure and texture based analysis of forming behavior and deformation mechanism of AA1050 sheet during Single Point Incremetnal Forming. *J. Mat. Proc. Technol*. 266:292-310 (2019).

[70] Wang, H., *et al*. Microstructure and mechanical properties of 2060-T8 Al-Li alloy after warm incremental forming. *J. Mech. Sci. Technol*. 32, **10**:4801-4812 (2018).

[71] Kim YH, Park JJ. Effect of process parameters on formability in incremental forming of sheet metal. *J. Mater. Process. Tech.* 130-131:42-46 (2002).

[72] Azevedo NG, Farias JS, Bastos RP, Teixeira P, Davim JP, Alves de Sousa RJ. Lubrication aspects during Single Point Incremental Forming for steel and aluminum materials. *Int. J. Precis. Eng. Manuf.* 16(3):589-595 (2015).

[73] Benmessaod, R., *et al.* Tool, lubricant and process parameters investigation to for an AA 3003-H12 sheet by single point incremental forming process. *Int. J. Sci. Eng. Res.*, 7(11), 950-960 (2016).

[74] Hagan, E. and J. Jeswiet. Analysis of surface roughness for parts formed by computer numerical controlled incremental forming. *Proc. Instn. Mech. Engrs*. Vol 218, Part B: J . Engineering Manufacture (2004).

[75] Echrif, Salah B.M. and Meftah Hrairi. Significant Parameters for the Surface Roughness in Incremental Forming Process. *Materials and Manufacturing Process*, 29:697-703 (2014).

[76] Dakhli, M. *et al.* Optimization of processing parameters and surface roughness of metallic sheets plastically deformed by incremental forming process. *Int. J. Adv. Manuf. Technol*. 102:977-990 (2019).

[77] Wei, Hongyu. *et al.* Surface roughness as a function of friction indicator and an important parameters-combination having controlling influence on the roughness: recent results in incremental forming. *Int. J. Adv. Manuf. Technol*. **101**:2533-2545 (2019).

[78] Kumar, Ajay *et al*. Effects of Process Parameters on Surface Roughness in Incremental Sheet Forming. *Materials Today: Proceedings 5*, 28026-28032 (2018).

[79] Kumar, Ajay and Vishal Gulati. Experimental investigation and optimization of surface roughness in negative incremental forming. *Measurement*, **131**:419-430 (2019).

[80] Jawale, Kishore *et al*. Lubrication study for Single Point Incremental Forming of Copper. *J. Phys. Conf. Ser*. **734** (2016).

[81] Jawale, Kishore et al. Microstructural investigation and lubrication study for single point incremental forming of copper. *Int. J. Solids. Struct.* **151**: 145-151 (2018).

[82] Horstemeyer, M. F. *Integrated Computational Materials Engineering (ICME) for Metals: Using Multiscale Modeling to Invigorate Engineering Design with Science*, (2012).

[83] Vander Voort, G. F. in *Metals Handbook Desk Edition.* 1394–1405 (1998).

[84] Vander Voort, G. F. Personal correspondence. (2016).

[85] Zwieg, T. A Universal Method for the Mechanical Preparation of Aluminium Alloy Specimens with High Edge Retention and their Subsequent Colour Etching. *Prakt. Metallogr.* **38,** 63–73 (2001).

[86] Vander Voort, G. F. in *ASM Handbook: Metallography and Microstructures* **9,** (1977).

[87] Kubic, R. (General Motors). Personal correspondence. (2016).

[88] Kamaya, M., Wilkinson, A. J. & Titchmarsh, J. M. Measurement of plastic strain of polycrystalline material by electron backscatter diffraction. *Nucl. Eng. Des.* **235,** 713–725 (2005).

[89] Yong-jun, C., Hjelen, J. & Roven, H. J. Application of EBSD technique to ultrafine grained and nanostructured materials processed by severe plastic deformation : Sample preparation, parameters optimization and analysis. *Trans. Nonferrous Met. Soc. China* **22,** 1801–1809 (2012).

[90] Neufeld, P. & Southall, D. M. The Electropolishing of Aluminium. *Electrodepos. Surf. Treat.* **3,** 159–168 (1975).

[91] Swain, J. The ‘then and now’ of electropolishing. *Surf. World* 32–36 (2010).

[92] Hensel, K. B. Electropolishing of Aluminum. *Met. Finish.* 19–20 (2001).

[93] Ma, D., Li, S. & Liang, C. Electropolishing of high-purity aluminium in perchloric acid and ethanol solutions. *Corros. Sci.* **51,** 713–718 (2009).

[94] Ji, L., Huang, K., Li, Y., Wu, Z. & Kang, J. Large-area self-ordered aluminium sub-micrometre dot arrays prepared by electropolishing on polycrystalline aluminium at constant current. *Corros. Sci.* **53,** 2914–2917 (2011).

[95] Berman, T. D., Pollock, T. M. & Jones, J. W. Texture, Second-Phase Particles, and the Anisotropy of Deformation Behavior in TTMP AZ61. *Metall. Mater. Trans. A Phys. Metall. Mater. Sci.* **46,** 2986–2998 (2015).

[96] E2627-13: Standard Practice for Determining Average Grain Size Using Electron Backscatter Diffraction (EBSD) in Fully Recrystallized Polycrystalline Materials. *ASTM Int.* 1–5 doi:10.1520/E2627

[97] Wright, S. I., Nowell, M. M. & Field, D. P. A review of strain analysis using electron backscatter diffraction. *Microscopy and microanalysis : the official journal of Microscopy Society of America, Microbeam Analysis Society, Microscopical Society of Canada* **17,** 316–329 (2011).

[98] Jorge-Badiola, D., Iza-Mendia, A. & Gutiérrez, I. Evaluation of intragranular misorientation parameters measured by EBSD in a hot worked austenitic stainless steel. *J. Microsc.* **228,** 373–383 (2007).

[99] Whitehouse, D.J. *Handbook of Surface and Nanometrology*. London: IOP Publishing, (2003).